TÉCNICO LISBOA

Local Based Calibration of the Thermoelastic Signal using Thermoelastic Stress Analysis and Digital Image Correlation

Francisco Pereira Brandão de Sá Rodrigues

Thesis to obtain the Master of Science Degree in

Aerospace Engineering

Supervisors: Prof. Afzal Suleman
Prof. Mehmet Yıldız

Examination Committee

Chairperson: Prof. Fernando José Parracho Lau
Supervisor: Prof. Afzal Suleman
Member of the Committee: Prof. Aurélio Lima Araújo

November 2019

Dedicated to my mother, brother and grandparents
(Armando and Júlia) for their constant support.

Acknowledgments

Firstly I would like to thank both my supervisors, Prof. Dr. Afzal Suleman and Prof. Dr. Mehmet Yıldız, for the opportunity they provided me in this journey and their early trust on my work and dedication to this project. Also for the immense knowledge and the financial support that both ensured me throughout this work.

The financial and infrastructural support given to me by Sabanci University - Integrated Manufacturing Technologies Research and Application Center, Sabanci University - Kordsa Composite Technologies Center of Excellence through, not only but greatly appreciated, an individual research grant but also all the trainings for the servo-hydraulic Instron machines, autoclave and hot press curing machines and laboratorial facilities that ensured all the necessary conditions for the fulfilment of this work.

A great part of my gratitude also goes to Eng. Ricardo Marques for all the immense knowledge and patience, for all the late night calls debating the results I obtained through the infrared camera and on whose previous work I have taken much inspiration and useful considerations. This thesis would have taken far longer to be developed if not for him.

I would also like to appreciate the contribution of all the technicians, engineers and Msc, PhD and PostDoc students that work at the Composite Center of Excellence whose help and conversations allowed me to grow as a person and as an engineer. My special thanks to Ertan Acar and Dr. Çağatay Yılmaz for all the manufacturing ideas and composite material properties insights. To Gokhan Inan, Sinan Karasu and Mehmet Olcaz for the trainings regarding the Instron's servo hydraulic machines and mechanical testing expertise. To Isa Emami, Hafiz Qasim Ali and Raja Awais for the help in the early stage of my work and for the discussions regarding the obtained results. Finally to Pouya Yousefi for the big friendship and all the conversations and knowledge he provided me.

Finally to my family, my mother Elisabete, my brother Tomás and my grandparents Armando and Maria Júlia for all the financial and emotional support throughout this journey that started in 2014. I owe everything to you.

Abstract

Increasing developments in camera's sensor quality and decreasing computational processing time has allowed the improvement of instruments and systems capable of detecting motions and temperature emissions characteristic of the thermoelastic phenomena.

Digital Image Correlation (DIC) and Thermoelastic Stress Analysis (TSA) have been increasingly used in the field of Experimental Mechanics as full-field Structural Health Monitoring (SHM) techniques due to the non-contact, non-destructive assessment of strain/stress fields in different materials with the incorporation of high resolution cameras for infrared(IR) detection, in the case of TSA, and sequential image acquisition, in the case of DIC.

Presently, the usage of TSA implies the pre-determination of some thermo-mechanical properties and the assumption of a model that best characterizes the material's global thermoelastic behaviour. However, due to the heterogeneity of the material, these assumptions prove to under/overestimate the stress/strain magnitude in the material.

To the authors knowledge, combine analysis using both TSA and DIC has been done in order to allow motion compensation of the infrared response of materials, however no mention is done in the literature to the local calibration of the thermoelastic signal in composite materials.

This thesis aims to correct the weaknesses found nowadays in the characterization of the thermoelastic effect as a global phenomena instead of a local one, dependent of characteristics of the material like the thickness of the resin rich layer or presence of voids which will influence local thermoelastic response.

Keywords: Thermoelastic Stress Analysis, Digital Image Correlation, Carbon Fiber-Reinforced Polymers, Structural Health Monitoring, Local Thermoelastic Signal Calibration

Resumo

O crescente desenvolvimento na qualidade dos sensores de câmeras permitiu a criação de instrumentos capazes de detectar emissões térmicas e movimento da ordem de grandeza dos que ocorrem no fenómeno termoelástico.

Correlação de Imagem Digital (DIC) e a Análise Termoelástica de Tensão (TSA) têm ganho crescente importância no campo da Mecânica dos Sólidos Experimental como técnicas de monitorização de saúde estrutural (SHM) devido à particularidade de não requererem contacto com o material e serem não destrutivas, tendo como objectivo a avaliação dos campos de tensão/extensão em diferentes materiais através da incorporação de câmeras infravermelhas, no caso de TSA, e de câmeras digitais, no caso de DIC.

A Análise Termoelástica de Tensão requer a predeterminação de algumas propriedades termomecânicas e assunção de um modelo que melhor permite caracterizar o comportamento termoelástico global do material, contudo, devido à heterogeneidade inerente do material, esta hipótese pode levar a sub/sobreestimações da sua resposta mecânica.

O uso combinado destas duas técnicas tem sido documentada como forma de compensar o movimento do material captado pela câmera infravermelha, não sendo feita, com conhecimento do autor, qualquer tipo de menção à calibração local dos modelos termoelástico.

Esta tese tem como objectivo evidenciar as desvantagens da calibração global dos modelos termoelásticos, em oposição a uma análise local devido à heterogeneidade inerente dos materiais compósitos, dependente de factores como a quantidade de resina na superfície ou a presença de locais com falta de material na estrutura.

Keywords: Análise Termoelástica de Tensão, Correlação de Imagem Digital, Polímeros reforçados com fibra de carbono,Análise de Saúde Estrutural, Calibração Termoelástica Local

Contents

List of Tables

List of Figures

Nomenclature

Abreviations

AGREE	Advisory Group for the Reliability of Electronic Equipment
CCD	Charge Coupled Device
CFRP	Carbon Fiber-Reinforced Polymer
CLPT	Classical Laminate Plate Theory
CMOS	Complementary Metal Oxide Semiconductor
CP	Cross Ply Laminate
CTE	Coefficient of thermal expansion
DCB	Double cantilever beam
DIC	Digital Image Correlation
DoT	Department of Transportation
FAA	Federal Aviation Administration
FFT	Fast Fourier Transform
GFRP	Glass Fiber-Reinforced Polymer
IR	Infrared
NUC	Non-Uniformity Correction
PAN	Polyacrilonitrile
QI	Quasi-Isotropic Laminate
RBF	Radial Basis Function
ROI	Region Of Interest
RTM	Resin Transfer Method
SEM	Scaning Electron Microscope
SHM	Structural Health Monitoring
SPATE	Stress Pattern Analysis

TSA	Thermoelastic Stress Analysis
UD	Unidirectional Laminate
VARTM	Vaccum Assisted Resin Transfer Method

List of Symbols

α_1,α_2	Coefficient of thermal expansion, in the principal directions
α_x,α_y	Coefficient of thermal expansion in the loading direction
α_r	Resin's coefficient of thermal expansion
γ	Shear Strain
δ	Variation, change
ϵ_{ij}	Small elastic strain tensor
ϵ_x, ϵ_y	Strain in the loading directions
ϵ_1,ϵ_2	Strain in the principal directions
θ	Lamina's Orientation
σ_{ij}	Stress tensor
σ_1, σ_2, σ_3	Stress in the lamina's principal directions
σ_x, σ_y	Stress in the loading directions
ν_{12},ν_{21}	Lamina's Poisson Ratio
ν_r	Resin's Poisson ratio
ρ_r	Resin's density
ρ	Laminate's Density
ϕ	Kernel Function
ξ	Background Mesh
[$\bar{Q}$]	Off-axis stiffness matrix
[A_{ij}]	Extensional stiffness matrix
[B_{ij}]	Extensional-bending stiffness matrix
[C]$_{6x6}$	Elastic isothermal stiffness tensor
[D_{ij}]	Bending stiffness matrix
[Q]$_{3x3}$	Reduced stiffness matrix
[S]$_{6x6}$	Compliance matrix
[T]$_\epsilon$	Transformation matrix for in-plane strain components
[T]$_\sigma$	Transformation matrix for in-plane stress components

C(x,y)	Cross-correlation function
C_σ,C_p	Specific heat at constant pressure
C_{pr}	Resin's specific heat at constant pressure
$E_{1,2}$	Tensile Stiffness in the principal directions
E_r	Resin's Young's Modulus
I(x,y)	Discrete intensity signal
K_i	Thermoelastic Constant in direction i
k_x,k_y,k_{xy}	Thermal Strain in the loading directions
m_c	Laminate's mass
O(x,y)	Continuous intensity signal
q	Heat transferred per unit mass
s	Entropy
T_0	Reference temperature
u	Internal Energy per unit volume
V_c	Laminate's volume
w	Work per unit mass
w_f	Fiber Volume Fraction
w_m	Matrix Volume Fraction
w_v	Void Volume Fraction

Chapter 1

Introduction

1.1 Composite Materials in Aerospace Industry

The continuous strive to comply with increasingly strict fuel saving requirements and environmental sustainability demands within the aerospace industry motivated the search for lighter materials capable of delivering high mechanical performances for structural applications. Composite materials have emerged as a viable alternative to metals (namely aluminium alloys) due to their higher stiffness- and strength-to-weight ratios, as well as higher resistance to corrosion and fatigue phenomena. More than 50% of the latest Boeing and Airbus aircraft models' structural weight is made of composite materials [1], being carbon and glass fiber-reinforced polymers (CFRPs and GFRPs, respectively) the most predominant. These materials are currently being employed in locations of the aircraft where high stiffness, yield strength and fatigue resistance is necessary to withstand high load and frequency levels[2] (figures 1.1 and 1.2).

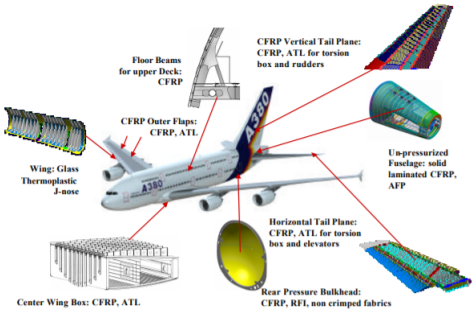

Figure 1.1: A380 Structural Components[2]

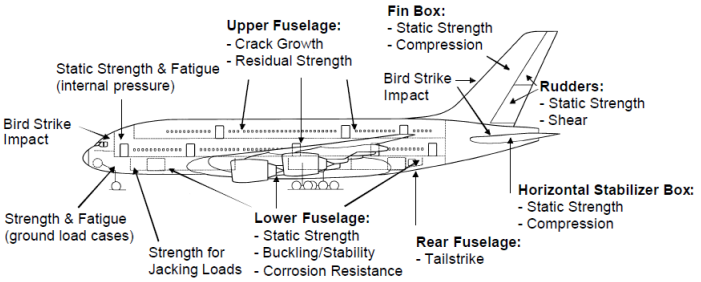

Figure 1.2: A380 Loads during flight[2]

During a flight mission, the structural integrity of aircraft components is continuously compromised by the effect of dynamic loading conditions imparted by wind gusts, accelerated maneuvers, or the impact after landing. This leads to the reduction of the material's lifetime, for which preventive replacement

and periodical revisions are currently the regulation methods being employed for monitoring structural integrity of structures [3]. Alternatively, Structural Health Monitoring (SHM) techniques allow real-time data acquisition and processing for damage location identification and severity quantification. This approach allows a more flexible maintenance scheduling based on evaluating the present material condition, whilst preventing unexpected damage generation that might lead to material failure.

1.2 Structural Health Monitoring

Material's life expectancy constitutes a topic of great importance in the aerospace industry due to the risk presented to human lives in case of structural failure. To better understand this topic, in the 1950s, AGREE (Advisory Group for the Reliability of Electronic Equipment) concluded that the failure rate of an electronic equipment throughout the operational lifetime can be presented in three distinct phases, as shown in figure 1.3.

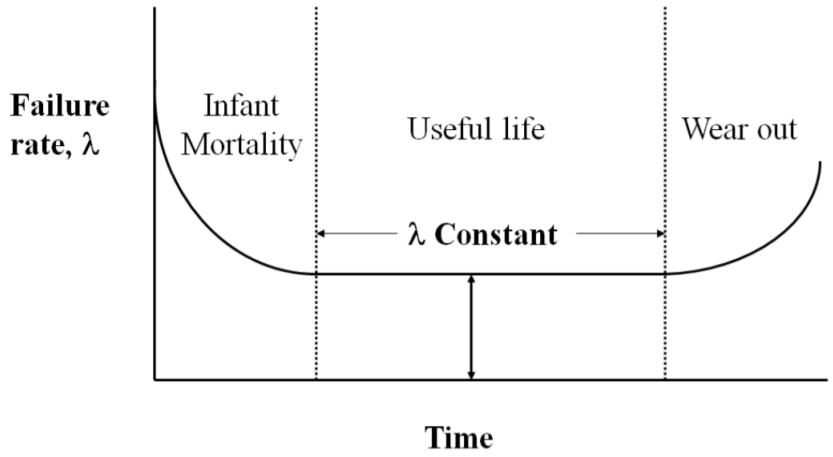

Figure 1.3: Bathtub Curve

1. Infant Mortality, where most of the manufacturing's critical imperfections lead to material failure;
2. Useful Life, with a constant failure rate λ;
3. Wear Out, where there is an increased probability of imminent failure due to the damage accumulated during service;

This classical "bathtub" curve can be also extended to other industries, including the aerospace.

Preventive maintenance lies in the supposition that the material under replacement is in the "Wear Out" phase of the bathtub curve. Application of this type of maintenance is valid, since commercial aircraft operate in a damage tolerance zone which allows the structures to withstand damage threshold before major failure occurs. Currently, US Airforce's airframes are under a scheduled maintenance plan, according to the Aircraft Structural Integrity Program (ASIP), which involves the maintainability of the structures according to manual periodic inspections [4]. This process requires the vehicle's re-

moval from service to ensure its structural integrity and passenger safety. In most cases, no damage is detected which demonstrates that this maintenance approach carries unnecessary and considerable costs, ranging from $1000 to $120 000, per inspection, depending on the aircraft configuration, inspection type and requirement for coating removal/restoration [4, 5]. This corresponds to the major limitation of the current maintenance regulation. However, damage occurs in an unpredictable time scale way and it is better evaluated if constant monitoring is carried out. Lack of proper damage monitoring has been the cause of some catastrophic events. Of these, the De Havilland Comet aircraft accident, in the early 1950ies, is referred[3] has the trigger to the birth of SHM in aeronautics. Figure 1.4 summarises some types of damage that might occur in aircraft structures and current repair methods.

Issue	*Solution*	*Comment*
Accident	Visual and/or Non-Destructive Inspection (NDI); Repair	Barely visible damage can be overseen
Loads	Design spectrum; pilot judgement followed by possible NDI	Very subjective judgement
Fatigue & Fracture	Damage Tolerance Design; Major Structural Testing; NDI; Inspection Interval	Can be time consuming and labour intensive
Corrosion	Design; Corrosion Protection Plan; NDI; Inspection Interval	
Multi-Site Damage	NDI; Inspection Interval	
Repair	Quality Assurance; NDI; Inspection Interval	

Figure 1.4: Damage in aircraft structures and current means of solution[3]

In order to address the aforementioned limitations, an extensive amount of research work exploited the non-contacting and non-destructive capabilities of SHM techniques such as Holography [6], Photoelasticity [7], Thermoelastic Stress Analysis (TSA) [8] and Digital Image Correlation (DIC) [9, 10]. Despite the current state-of-the-art, several challenges are posed to the translation of SHM to real maintenance scenarios [5]. Within the regulatory aircraft's structural integrity assessment framework, the large time scale and high costs involved in incorporating SHM techniques in the maintenance process makes this transition prohibitive. Moreover, the localized nature of damage onset, together with the large and varying time-scales of propagation can pose several challenges for SHM techniques to provide damage assessment since there is a lack of available data of in-service damage progression of structures. Development of models capable of quantitative and qualitative damage assessment and capable of identifying types of failure in composite materials has yet to be done. Another meaningful non-technical challenge comes with persuading structure manufacturers of the financial advantages of employing these techniques by altering the current guidelines and regulations to address evolving technology [4, 5].

The two following sections introduce the SHM techniques under study in this thesis.

1.3 Digital Image Correlation (DIC)

DIC [9, 10] is a non-contact and non-destructive SHM technique that collects a set of images from an object under deformation, stores them under digital form and performs a subsequent analysis in order to obtain a full-field evaluation of the object's mechanical behaviour. Deformation and motion quantification through the usage of this technique relies in the monitoring and identification of changes in the surface pattern through the comparison of two images: a reference stage (typically in the unloaded condition) and a deformed stage (after loading is imparted).

Quantification of the material's motion through the difference between collected images relies on two assumptions [9, 11]:

- A direct correlation between the material's motion and the camera's sensor reading is obtained, i.e there is continuity in the material;
- The sample presents, or is painted with, a natural high-contrast random pattern for accurate image matching, throughout the measurement.

Therefore, DIC outputs are compromised in the following cases:

- Image subsets contain discontinuities (e.g cracks, holes);
- Loss of image contrast due to delamination, debonding, or change in surface's diffuse reflectivity.

Depending on the number of cameras employed for displacement evaluation, DIC techniques can be classified as two-dimensional or three-dimensional (2D and 3D, respectively). While 2D-DIC measurements employ a single camera whose lens axis is perpendicular to the specimen's surface for in-plane deformation assessment, 3D-DIC output complements the aforementioned method with the specimen's normal displacement and curvature through the usage of two cameras.

Motion quantification involves the distinction between four different systems of axes (figure 1.5): the world's coordinate system (X_w, Y_w, Z_w), the camera's coordinate system, the sensor's coordinate system (X_s, Y_s, Z_s) and the object's coordinate system.

1.3.1 Applications to composite materials

Many authors have taken advantage of the DIC's full-field characteristics in the quantification of the mechanical behaviour of composite materials, validating the reliability of this SHM technique. Canal et al.[12] were able to detect large strain fluctuations in fiber and matrix rich zones of E-glass/epoxy laminates under transverse compressive load using DIC together with Scanning Electron Microscopes (SEM). Regarding damage monitoring, Muc et al.[13] found that DIC was able to highlight strain concentration zones and identify the crack tip zones in circular and elliptical holes, for glass/epoxy and glass woven roving fabric/epoxy resin materials. Caminero et al.[14] attempted simulate the mechan-

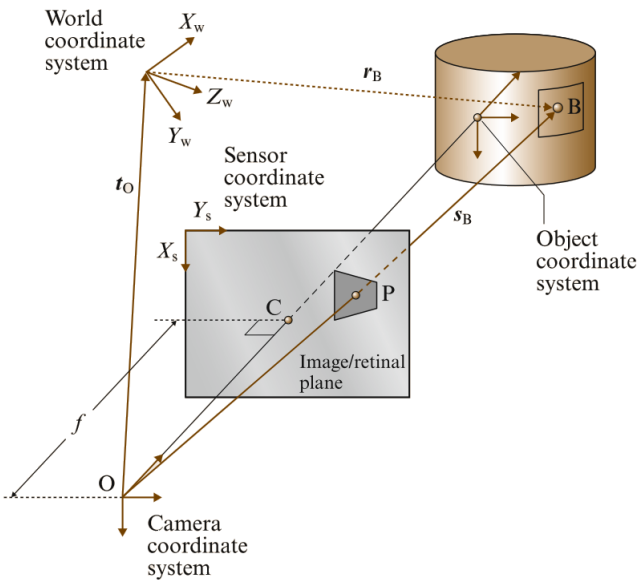

Figure 1.5: Two-dimensional DIC system of axis[9]

ical behaviour of aircraft structures discontinuities, such as cut-out and fastener holes, by employing 2D and 3D DIC for strain measurements in different notched carbon-fiber/epoxy composite specimens under uniaxial tensile loading, and damage monitoring of adhesively bonded patch repairs in composite panels.

1.3.2 Applications in aerospace

The aircraft's certification process consists in the submission of each component and assembly systems to several rigorous tests in order to ensure the passengers' safety, whose completion and final approval for commercial flight purposes may take up to several years [2]. The landing gear is a component whose certification process involves longer and a particular set of tests due to its vital role in damping the impact loads.

Landing gear is a component of the aircraft whose certification involves long and different tests, due to the vital role it develops in impact load damping, for which companies increasingly rely on optical monitoring for evaluation of its structural performance[15], as represented in figure 1.6. Specifically for this component, two sets of tests are performed[15],

- Limit and Ultimate Tensile tests, where the component's structural integrity is evaluated.
- Dynamic tests, where the component's fatigue resistance is compared with the specifications of the manufacture.

The purpose of the static certification test is to allow the structure to be subjected to several critical load cases that intend to simulate the conditions which would occur during landing and taxi of the aircraft, whilst the second test intends to predict the fatigue cycle life of this component in order to assess

when preventive maintenance should occur. During these tests, DIC provided 3D displacements and deformations on a full-field basis, not only for the entire assembly but for individual parts of this structure. This assisted engineers in identifying if the components and respective assembly were able to withstand higher deformations. Moreover, by allowing three dimensional deformations, pinpointing of the heavily loaded locations due to translational and rotational movement was possible.

DIC has reportedly been used in order to assist the certification of aircraft, like the A350[16], as an optical metrology method. This technique not only allowed full-field motion assessment (figure 1.7) during numerous static and dynamic tests with an almost instantaneous processing of the data but also a valid method for validation of finite element analysis results.

Figure 1.6: Full-Field Monitoring of Landing Gear Displacement[15]

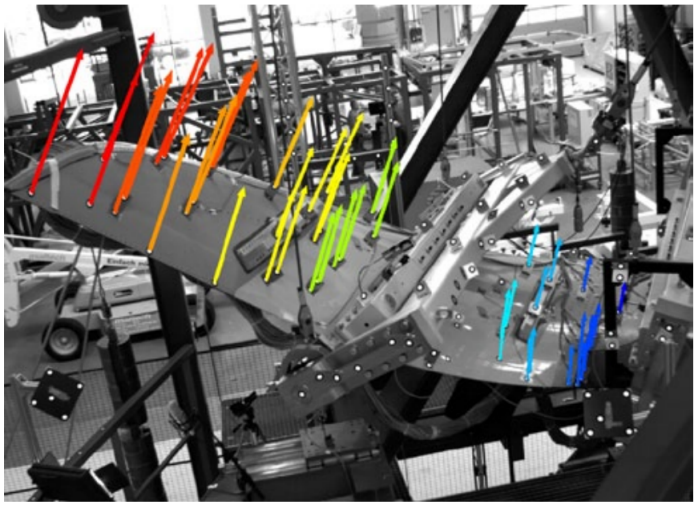

Figure 1.7: A350 winglet spatial motion assessment[16]

A peculiar situation that was emphasised by the authors in their report[16] is the ability brought by this optical method by accelerating the already in use conventional techniques. More specifically it highlights the time saving that 3D-DIC measurements brought to the determination of the points where the strain gauges should be attached for more local deformation measurement, by employment of strain gauges.

1.4 Thermoelastic Stress Analysis (TSA)

1.4.1 Thermoelastic effect in continuous solids

Consider a container where an ideal gas is stored and the system can be considered as isolated (no exchange of mass and energy with the surroundings). Cyclic motion of a lubricated piston will induce a compression and expansion of the gas, associated with the decrease and increase of volume. If this process occurs under isentropic conditions, the change of the average kinetic energy, related with the

pressure change, will induce a correspondent temperature variation (according to equation 1.1).

$$\frac{T_2}{T_1} = \frac{p_2}{p_1}^{\frac{\gamma-1}{\gamma}} \tag{1.1}$$

where T_1 and T_2 are, respectively, the initial and final temperature, associated to pressures p_1 and p_2 and γ is the ratio between the gas' specific heats.

The same effect occurs in a solid material, subjected to a combination of tensile-compressive loads, in isentropic conditions. More specifically, a material under a compressive load increases its temperature, from an initial state (T_i) to a final state (T_f) and the inverse effect is verified when the material is extended ($T_f < T_i$). This is known as the thermoelastic effect of a solid material and was firstly reported in a qualitative manner by Gough[17], in 1805, with its work in "indian rubber". Later, in 1857, the mathematical formulation for the thermoelastic effect was firstly reported.

Requirements for the material to be loaded under isentropic conditions translate in small deformations which induce small cyclic fluctuations of temperature in the material, around 1.0 mK in metals for a stress amplitude of 1 MPa [18]. Therefore, appropriate cameras, sensitive to small temperature variations originated due to the thermoelastic effect, have to be employed. This justifies the gap between the theoretical developments and the initial quantitative measurements of the thermoelastic phenomena (denominated Thermoelastic Stress Analysis), which only became possible in 1982, with the development of the first thermographic instrument, the Stress Pattern Analysis (**SPATE**) system. Prior to this, the order of magnitude of such effect could not be perceived by the available technology.

Current developments in highly sensitive infrared(IR) cameras allowed quantitative measurements of the thermoelastic effect to gain increasing popularity in the real time monitoring and structural integrity evaluation. To summarise, the purpose of TSA is to generate a detectable temperature variation in the material's surface and correlate it with the respective sum of stress amplitude, due to a variable applied mechanical load, under isentropic conditions.

1.4.2 Thermoelastic Equations

The theoretical foundations of TSA were developed by William Thomson (Lorde Kelvin), in 1857. Thomson [19] derived the mathematical formulation that characterises the thermoelastic behaviour of a solid isotropic material, based on the first and second law of thermodynamics and classical mechanics, relating the material's temperature change, ΔT, with the stress change in the principal directions, $\Delta\sigma_{ii}$, leading to the classic formulation of the thermoelastic effect (equation 1.2).

$$\Delta T = -\frac{T_0 \alpha}{\rho C_p} \Delta(\sigma_{11} + \sigma_{22}) \tag{1.2}$$

where T_0 the absolute temperature, ρ, the density of the material, C_p the Specific Heat and α the

coefficient of thermal expansion (CTE). Equation 1.2 relies in the assumption of reversible conditions. This conditions is fulfilled if the induced stress from the applied load is inferior to the yield stress, since the material remains in the elastic domain (characterized by a linear relation between stress and strain), where all the deformations it undertakes are reversible, providing no heat generation effects originated from defects in the material (void, cracks, among others) are present. However, in order for this temperature change to be measurable through infrared cameras, heat transfer phenomena must be negligible. This will be achieved by applying the variable mechanical load at a frequency high enough so that the temperature change is retained in the material.

If an orthotropic material under plane stress is being evaluated, then the temperature amplitude is dependent of a linear combination between the coefficient of thermal expansion, α_1 and α_2 , and the stress amplitude, $\Delta\sigma_1$ and $\Delta\sigma_2$, in the material's principal direction.

$$\Delta T = -\frac{T_0}{\rho C_p}[\alpha]^T_{1,2}[\Delta\sigma]_{1,2} \tag{1.3}$$

By rewriting equation 1.2 for uncalibrated infrared systems, the following equation is obtained [8],

$$AS = K(\Delta\sigma_1 + \Delta\sigma_2) \tag{1.4}$$

where A and S are the camera's calibration constant and uncalibrated signal, respectively, and K corresponds to the thermoelastic constant, given by

$$K = \frac{\alpha}{\rho C_p} \tag{1.5}$$

In annex A the full deduction of the TSA equation can be found. As stated in this section, the TSA equation are valid if adiabatic conditions are attained during the loading.

To summarise, Thermoelastic Stress Analysis measurements require the material to be cyclically loaded, with an appropriate frequency, in order to obtain measurable temperature changes in the infrared camera's wavelength scope, achieved through the dynamic combination of tension and compression loads in the material's elastic region, allowing the retaining of the temperature change amplitude in the material's surface [8].

1.4.3 Application to Composite Materials

Quantitative TSA analysis in fiber-reinforced polymers (FRP) has been the focus of numerous researches. Marques et al. [20] provided a new methodology for the calculation of the Remaining Useful Life of quasi-isotropic GFRP laminates through the usage of TSA measurements, for calculation of the strain energy density by obtaining the temperature amplitude experienced by a material during fatigue

tests.

Krstulovic-Opara et al. [21] employed TSA for measuring the stress field in post-impact damage evaluation of GFRP composite materials. For this, an impact damaged $[0/90]_2$ woven glass/epoxy sample was loaded at 10 Hz, it was reported that TSA was able to identify fiber damaged locations.

Emery et al. [22] evaluated the strain field distribution in the vicinity of three types of damage mechanisms: delamination, fiber breakage and matrix cracking for different stacking sequences of uni-directional pre-impregnated E-glass epoxy laminates. Different laminate's were manufactured so that only one type of damage would occur. For cross ply laminate's, matrix cracking was observed, for angle ply, delamination and for quasi-isotropic fiber breakage, although delamination and matrix cracking also occurred.

Pitarresi and Galietti [23] investigated the influence of two theoretical thermoelastic theories, the Bulk model and the Resin Rich Layer model, in the CFRP's thermoelastic response. In this work, the authors manufactured laminates, which their theoretical work predicted the two models would supply different thermoelastic responses. The results obtained led the authors to point out the different significance of the Resin rich layer model's influence for GFRPs and CFRPs. One of the reasons for this was related with the significant dependence of Bulk model in the coefficient of thermal expansion and the variability of this parameter within the lamina.

1.4.4 Applications in aerospace

Nik Rajic and Steve Galea [24] have proposed the incorporation of TSA in aircrafts however, this technique's feasibility combined with all the appropriate conditions for such (frequency of the tests, load amplitude, type of material and surface coating), constitutes a challenge for the marketing of this SHM technique as cost-saving and more efficient to aircraft manufacturers.

Figure 1.8 illustrates the proposal from the previous authors for the incorporation of this SHM technique in the aircraft structure for monitoring of high failure locations.

Dulieu-Barton et al.[25] point out that, while most TSA research relies on the measurement of small samples of composite materials, industrial applications of these materials often do not allow the disassembly of the structure. In this way a portable system is necessary to apply the necessary loads/frequencies for an accurate measurement. The experimental part of their work relied on the usage of a stringer for the application of the loads at the frequency of the first and third vibrational modes in the center of the composite plate.

Tomlinson and Calvert[26] provided a summary of some cases study which applied Thermoelastic Stress Analysis for industrial applications. One of these comprised the analysis of a fuel pump, where real flight conditions were simulated and a large electro-mechanical shaker applied the desired loading at the resonance frequencies. TSA measurements focused on the upper metal flange, which, due to

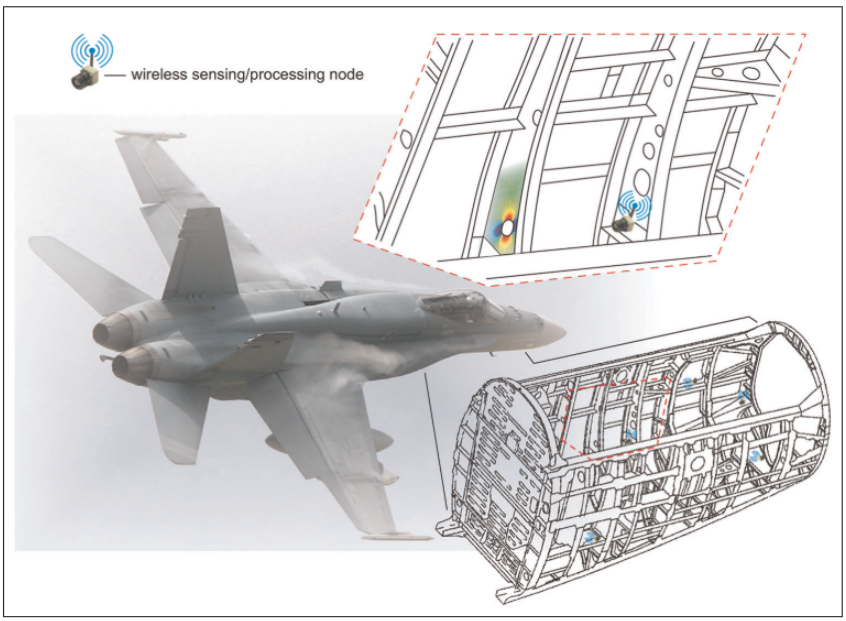

Figure 1.8: Incorporation of TSA in the aircraft industry [24]

the high temperature operating conditions,led to the authors stressing the importance of TSA for these measurements, since other techniques would not measurements though other SHM techniques were impossible.

1.5 Joint employment of DIC and TSA

One of the well known limitations of TSA is that the camera output is only related to the first invariant of the stress/strain, not providing its individual components[27]. Correction of this setback can be done by employing DIC in the tests which allows the separation of the stress/strain components in the different directions.

Joint employment of DIC and TSA has been used by authors to address different limitations of these techniques. Silva et al.[28] used DIC alongside TSA with only one CCD camera to correct sample motion which may compromise the infrared readings for monitoring of fatigue crack tip in an aluminium alloy 2024 and measurement of open hole displacement field in a Nylon 6 plate. In this work, DIC and TSA measurements were both resultant from the same set of IR images and discontinuities arising by the gaps in the speckle pattern were filled by interpolating the data across the speckles.

Wang et al.[29] stressed that, even though the work by Silva et al.[28] presents several benefits, the, at the time, IR detectors provided limited spatial resolutions, decreasing the accuracy of the displacement field calculated by the DIC. This can pose several problems especially when discontinuities are presented in the surface. To correct these weaknesses, the authors employed two camera systems with respective position markers in order to address complex body motions, more specifically face sheet

debonding in double cantilever beam (DCB).

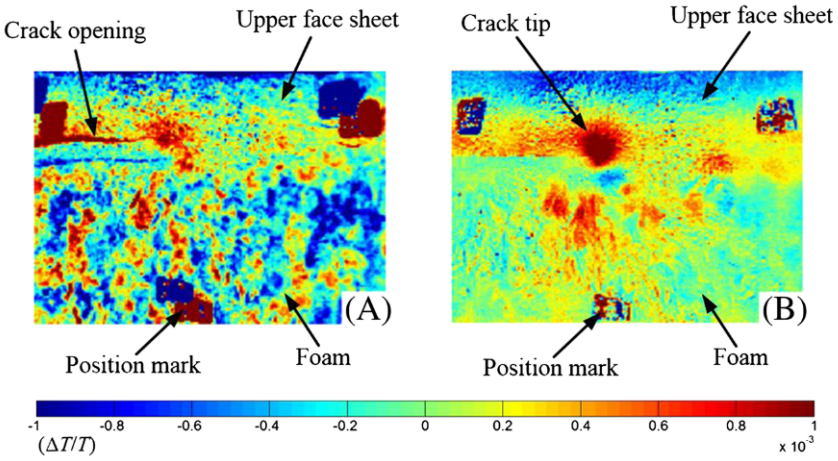

Figure 1.9: Temperature ratio distribution on DCB obtained with(A) and without(B) motion compensation[29]

Figure 1.9 illustrates the result of the work of these authors in the improvement of TSA results for the DCB crack tip propagation monitoring.

1.6 Motivation and Objectives

Current TSA measurements resort to a global calibration of the thermoelastic signal through employment of strain gauges or extensometers during cyclic load test. These measurements systems provide an average value for the laminate's strain change during the loading limits of the sample. These values, considered the theoretical results, are converted into temperature change values by replacing them in the thermoelastic models equations. Afterwards, these theoretical values are compared with the values obtained from the camera output signal.The model which will be selected to characterize the behaviour of the whole system corresponds to the one that gives the lowest error.

The aforementioned method does not exploit the full-field capabilities of TSA since the heterogeneity of material's like FRPs is not considered. The material is assumed to be homogeneous and only one model is assigned to characterize the full-field behaviour of the material, not accounting with the inherent imperfections that are associated with the manufacturing process of composite materials. One of the main concerns related to this assumption is the over/underestimation of strain in critical regions that might lead to safety issues in high risk industries, such as the aerospace industry.

In this work, a methodology is proposed for switching from a global to a local-wise calibration technique in order to correct these wrong assumptions which do not fully exploit an otherwise strong and useful way to prevent failure in materials. This will be done by employing DIC, for a full-field assessment of strain, instead of extensometers of strain gauges which only allow local strain measurement (usually in the center of the gauge length).

1.7 Thesis Outline

A brief description of the contents of the forward chapters are now presented.

Chapter 1

Chapter 1 reflects on the lack of regulatory maintenance based approaches which rely on the material's present state. Furthermore, this chapter introduces the two SHM techniques used during this thesis and lays the motivation behind the usage of both these techniques for fulfilling this work's objective.

Chapter 2

Chapter 2 details composite material's microstructure and develops the mathematical formulation for predicting the mechanical behaviour of these materials mesostructure and macrostructure.

Chapter 3

During this chapter, the description of Digital Image Correlation technique for addressing full-field deformation measurements is detailed, giving particular emphasis to the mathematical formation which allow correlation between captured image and deformation quantification.

Chapter 4

The principles of Thermoelastic Stress Analysis are presented namely the non-adiabatic effects inherent to composite materials, including heat transfer, the effect of the resin surface layer and the influence of the loading frequency in the analysis. Furthermore, the mathematical formulations for the already proposed models, in the literature, are presented.

Chapter 5

The manufacturing process, from the laminae assembly to the CFRP sample tabbing, is described in this chapter.

Chapter 6

In this chapter, the tests performed for determining the properties necessary to perform quantitative TSA measurements are detailed with the corresponding references to the ASTM standards.

Chapter 7

In this chapter, a detailed description of the followed procedure was done, with a detailed description of the interpolation methodology for valid concurrent usage of DIC and TSA. Furthermore, the results are presented alongside its analysis.

Chapter 8

Concluding remarks of this work and future work is enumerated.

Chapter 2

Composite Materials

Composite materials, particularly FRPs, contain two different phases whose combined properties are superior to the individual component's if each were to act separately. A fibrous material with high stiffness and strength withstands high load levels, while a continuous polymeric matrix embeds the fibers to improve the load transmission and protect the laminate from corrosion and humidity.

The composite materials' structure can be described in the following length scales:

- Micro level, where material properties are defined at the fiber and matrix levels;
- Ply or lamina level, where the fiber/matrix mixture is homogenized and each lamina is characterized by the fiber orientation;
- Laminate level, consisting in the stacking of several laminae;

2.1 Microstructure

2.1.1 Fibers

For FRPs, several types of fibers can be found in the literature[30]. Of these, glass, carbon and aramid fibers are the most commonly mentioned. Selection of the reinforcement is highly dependent of the application's requirements and available resources.

Carbon fibers are lightweight materials composed, in its majority, by carbon atoms, whose average size extends from 5, to 10 micrometers. This type of fibers have become one of the most important fiber reinforcements for polymeric matrix composites by increasing its strength, toughness, electrical and thermal properties. Carbon fibers can be twice as stiff and five times stronger than steel (per unit weight)[31] and present a higher tensile modulus than many other fiber reinforcements, thus justifying their applicability in industries that require high mechanical performance at the component's level, such

as the aeronautical and automotive.

Glass fiber reinforcements were pioneer in the replacement of metals in aircraft structures[30]. Due to the high range of commercial applications and respective requirements, several variations of glass fibers can be manufactured. Of these, E-glass and S-glass fibers are the most commonly referred, for their high electrical and high strength properties, respectively. S-Glass fibers have a 25% higher tensile strength and 17% higher stiffness modulus than E-Glass fibers. Even though this kind of fibers has lower mechanical properties, compared to carbon fibers, it provides a valid alternative due to the lower cost (between 2.5 to 5 times less expensive than PAN based carbon fibers). Due to the low density this reinforcement is employed in structures which are not heavily loaded and allow weight saving. Applications for this type of fibers range from ship hulls and glider constructions, to high pressure gas containers and rocket motor casings[32].

Aramid fibers are a class of organic fibers, introduced in the 1970's. These type of reinforcement are characterized by low density (1.44g/cm^3, 40% lower than glass and 20% lower than common carbon), high tensile stiffness and strength, low compressive properties and low shear modulus(due to the weak hydrogen bonds in the molecular structure) and are not as brittle as glass or carbon. Combining fiber toughness and low density results in very lightweight structures. Composite materials, reinforced with aramid fibers, produce structures highly damage tolerant, with superior vibration-damping characteristics, when compared with other fiber reinforcements. However, the low compressive properties, characteristic of organic fibers, limit the applicability of this type of fibers for high performance structural applications. This justifies the application of this type of fibers to secondary structures of aircraft, which are not heavily loaded[32], reducing its structural weight. However, the main application of this kind of fibers resides in the ballistic industry, as body, tank and aircraft armour for impact damage.

Common employment of continuous fiber reinforcement in commercial applications is done through two different fiber configurations, all parallel fibers (continuous unidirectional configuration) and fibers applied with right angles between each other (woven fabric configuration).

2.1.2 Matrix

Two types of polymers are usually employed in FRPs, thermosets and thermoplastics. Thermosets correspond to the group of polymers that, once cured, acquire a solid form which cannot be returned to the initial state. Composite material with this matrix are characterized by high strength and fatigue resistance[30]. Contrarily, thermoplastics allow reverting the polymer's form to the initial state, without loss of physical properties. These materials present higher impact resistance and damage tolerance than thermosets and, since they can be reheated, it eases damage repair procedure. However, thermoplastics require higher manufacturing energy for melting the plastic and impregnating the fibers, which makes thermoplastics a more expensive alternative than thermosets.

For fiber-reinforced polymers the commonly used thermoset matrices are Epoxy and Polyester resins.

Epoxy based matrices have found a wide range of applications, namely in the aerospace industry, due to the possibility of altering parameters, such as the curing cycle, in order to obtain certain mechanical and viscoelastic properties. Cured epoxy yields[33] high tensile, compressive, flexural and fatigue strengths, when compared to other polymers, good adhesion to several types of materials, high corrosion resistance and low shrinkage during cure, which allows a better size control. The main disadvantages of this material lies in the brittleness and reduction of properties in the presence of moisture.

Polyester resins are relatively inexpensive and easily processed materials used in low-cost applications. Moreover, this material presents high thermal and dimensional stability and creep resistance. Cure of this resin can be done within a high range of temperatures, however without the proper temperature conditions, it remains in a plasticized state. Main advantages of these type over epoxy based, lies in the easier processing and higher toughness.

2.2 Mesostructure

2.2.1 Coordinate system

Characterizing the in-plane behaviour of composite laminates, constituted by unidirectional laminae, involves considering two different systems of axes (figure 2.1),

1. Local reference system: oriented along the fiber's direction, i.e lamina's principal directions (1, 2 and 3);
2. Global reference system: oriented along the laminate's loading direction (*x*,*y*, *z*);

The angle, θ, given by the counter-clockwise rotation between the laminae and laminate's axes system corresponds to the lamina's orientation.

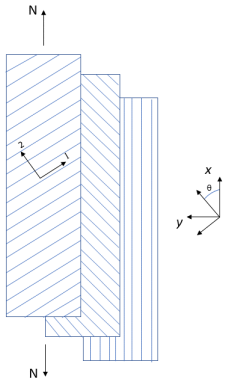

Figure 2.1: Lamina (1,2) and laminate (x,y) in-plane reference axes

2.2.2 Constitutive Law

The stress state in a point of an anisotropic material can be characterized by 6 stress components, σ_i, and 6 strain components, ϵ_i, which are related, in contracted notation, by the following equations, known as the generalized Hooke's law,

$$\begin{bmatrix} \sigma_1 \\ \sigma_2 \\ \sigma_3 \\ \tau_4 \\ \tau_5 \\ \tau_6 \end{bmatrix} = \begin{bmatrix} C_{11} & C_{12} & C_{13} & C_{14} & C_{15} & C_{16} \\ C_{21} & C_{22} & C_{23} & C_{24} & C_{25} & C_{26} \\ C_{31} & C_{32} & C_{33} & C_{34} & C_{35} & C_{36} \\ C_{41} & C_{42} & C_{43} & C_{44} & C_{45} & C_{46} \\ C_{51} & C_{52} & C_{53} & C_{54} & C_{55} & C_{56} \\ C_{61} & C_{62} & C_{63} & C_{64} & C_{65} & C_{66} \end{bmatrix} \begin{bmatrix} \epsilon_1 \\ \epsilon_2 \\ \epsilon_3 \\ \gamma_4 \\ \gamma_5 \\ \gamma_6 \end{bmatrix} \tag{2.1}$$

and

$$\begin{bmatrix} \epsilon_1 \\ \epsilon_2 \\ \epsilon_3 \\ \gamma_4 \\ \gamma_5 \\ \gamma_6 \end{bmatrix} = \begin{bmatrix} S_{11} & S_{12} & S_{13} & S_{14} & S_{15} & S_{16} \\ S_{21} & S_{22} & S_{23} & S_{24} & S_{25} & S_{26} \\ S_{31} & S_{32} & S_{33} & S_{34} & S_{35} & S_{36} \\ S_{41} & S_{42} & S_{43} & S_{44} & S_{45} & S_{46} \\ S_{51} & S_{52} & S_{53} & S_{54} & S_{55} & S_{56} \\ S_{61} & S_{62} & S_{63} & S_{64} & S_{65} & S_{66} \end{bmatrix} \begin{bmatrix} \sigma_1 \\ \sigma_2 \\ \sigma_3 \\ \tau_4 \\ \tau_5 \\ \tau_6 \end{bmatrix} \tag{2.2}$$

which can be simplified in index notation by

$$\begin{aligned} \sigma_i &= C_{ij}\epsilon_j \\ \epsilon_i &= S_{ij}\sigma_j \end{aligned} \tag{2.3}$$

where C_{ij} and S_{ij} are the elastic stiffness and compliance matrices, respectively, each containing 36 elastic constants that should be calculated to fully characterize the material's mechanical behaviour.

2.2.3 Orthotropic Material

Mechanical properties of orthotropic materials can be described along 3 axes of symmetry. Therefore, the stiffness tensor, shown in equation 2.1, can be characterized by 9 independent elastic stiffness constants:

$$\begin{bmatrix} \sigma_1 \\ \sigma_2 \\ \sigma_3 \\ \tau_4 \\ \tau_5 \\ \tau_6 \end{bmatrix} = \begin{bmatrix} C_{11} & C_{12} & C_{13} & 0 & 0 & 0 \\ C_{12} & C_{22} & C_{23} & 0 & 0 & 0 \\ C_{13} & C_{23} & C_{33} & 0 & 0 & 0 \\ 0 & 0 & 0 & C_{44} & 0 & 0 \\ 0 & 0 & 0 & 0 & C_{55} & 0 \\ 0 & 0 & 0 & 0 & 0 & C_{66} \end{bmatrix} \begin{bmatrix} \epsilon_1 \\ \epsilon_2 \\ \epsilon_3 \\ \gamma_4 \\ \gamma_5 \\ \gamma_6 \end{bmatrix} \tag{2.4}$$

Considering the in-plane dimensions of the lamina to be much higher than the thickness, plain-stress condition is valid and defined by,

$$\sigma_3 = \tau_4 = \tau_5 = 0 \tag{2.5}$$

Therefore, the following equations are obtained,

$$\begin{aligned} \sigma_1 &= C_{11}\epsilon_1 + C_{12}\epsilon_2 + C_{13}\epsilon_3 \\ \sigma_2 &= C_{12}\epsilon_1 + C_{22}\epsilon_2 + C_{23}\epsilon_3 \\ 0 &= C_{13}\epsilon_1 + C_{23}\epsilon_2 + C_{33}\epsilon_3 \\ \tau_6 &= C_{66}\epsilon_6 \end{aligned} \tag{2.6}$$

By rewriting the previous equations dependent of the in-plane strains, the following equation is obtained,

$$\begin{aligned} \sigma_1 &= (C_{11} - \frac{C_{13}^2}{C_{33}})\epsilon_1 + (C_{12} - \frac{C_{13}C_{23}}{C_{33}})\epsilon_2 \\ \sigma_2 &= (C_{12} - \frac{C_{13}C_{23}}{C_{33}})\epsilon_1 + (C_{22} - \frac{C_{23}^2}{C_{33}})\epsilon_2 \\ \tau_6 &= C_{66}\gamma_6 \end{aligned} \tag{2.7}$$

For plain-stress state, the previous system of equations can be rewritten in matrix form as

$$[\sigma] = [Q][\epsilon] \tag{2.8a}$$

where $[Q]$ is denoted as the reduced stiffness matrix, for plain-stress conditions.

$$\begin{bmatrix} \sigma_1 \\ \sigma_2 \\ \tau_6 \end{bmatrix} = \begin{bmatrix} Q_{11} & Q_{12} & 0 \\ Q_{21} & Q_{22} & 0 \\ 0 & 0 & Q_{66} \end{bmatrix} \begin{bmatrix} \epsilon_1 \\ \epsilon_2 \\ \gamma_6 \end{bmatrix} \tag{2.8b}$$

where,

$$\begin{aligned} Q_{11} &= (C_{11} - \frac{C_{13}^2}{C_{33}}) = \frac{E_1}{1 - \nu_{12}\nu_{21}} \\ Q_{12} &= (C_{12} - \frac{C_{13}C_{23}}{C_{33}}) = \frac{\nu_{21}E_1}{1 - \nu_{12}\nu_{21}} \\ Q_{21} &= (C_{12} - \frac{C_{13}C_{23}}{C_{33}}) = \frac{\nu_{12}E_2}{1 - \nu_{12}\nu_{21}} \\ Q_{22} &= \frac{E_2}{1 - \nu_{12}\nu_{21}} \\ Q_{66} &= G_{12} \end{aligned} \tag{2.8c}$$

By inspecting the system of equations from 2.8c, symmetry of the stiffness matrix is proved. There-

fore, the following relation can be derived, from establishing $Q_{12} = Q_{21}$

$$\frac{\nu_{12}}{E_1} = \frac{\nu_{21}}{E_2} \tag{2.9}$$

For converting the stress and strain vectors of an unidirectional ply oriented at an angle θ, between two references axes systems, transformation matrices are employed, $[T]_\sigma$ and $[T]_\epsilon$, and the inverses, $[T]_\sigma^{-1}$ and $[T]_\epsilon^{-1}$.

$$\begin{bmatrix}\sigma_1\\ \sigma_2\\ \tau_6\end{bmatrix} = \Big[T\Big]_\sigma \begin{bmatrix}\sigma_x\\ \sigma_y\\ \tau_{xy}\end{bmatrix} \tag{2.10a}$$

$$\begin{bmatrix}\epsilon_1\\ \epsilon_2\\ \gamma_6\end{bmatrix} = \Big[T\Big]_\epsilon \begin{bmatrix}\epsilon_x\\ \epsilon_y\\ \gamma_{xy}\end{bmatrix} \tag{2.11a}$$

$$\begin{bmatrix}\sigma_x\\ \sigma_y\\ \tau_{xy}\end{bmatrix} = \Big[T\Big]_\sigma^{-1} \begin{bmatrix}\sigma_1\\ \sigma_2\\ \tau_6\end{bmatrix} \tag{2.10b}$$

$$\begin{bmatrix}\epsilon_x\\ \epsilon_y\\ \gamma_{xy}\end{bmatrix} = \Big[T\Big]_\epsilon^{-1} \begin{bmatrix}\epsilon_1\\ \epsilon_2\\ \gamma_6\end{bmatrix} \tag{2.11b}$$

The transformation matrices are given by the following equations, where $c = cos(\theta)$ and $s = sin(\theta)$.

$$\Big[T\Big]_\sigma = \begin{bmatrix} c^2 & s^2 & 2cs \\ s^2 & c^2 & -2cs \\ -cs & cs & C^2 - s^2 \end{bmatrix} \tag{2.12a}$$

$$\Big[T\Big]_\epsilon = \begin{bmatrix} c^2 & s^2 & cs \\ s^2 & c^2 & -cs \\ -2cs & 2cs & C^2 - s^2 \end{bmatrix} \tag{2.13a}$$

$$\Big[T\Big]_\sigma^{-1} = \begin{bmatrix} c^2 & s^2 & -2cs \\ s^2 & c^2 & 2cs \\ cs & -cs & C^2 - s^2 \end{bmatrix} \tag{2.12b}$$

$$\Big[T\Big]_\epsilon^{-1} = \begin{bmatrix} c^2 & s^2 & -cs \\ s^2 & c^2 & cs \\ 2cs & -2cs & C^2 - s^2 \end{bmatrix} \tag{2.13b}$$

2.2.4 Isotropic Material

Isotropic materials, such as the cured Epoxy matrix, have an infinite number of symmetry axes, thus the mechanical behaviour is independent of the material's direction. Therefore, the stiffness tensor can be further simplified and only two stiffness constants need to be computed. Under these conditions, equation 2.1 simplifies to

$$\begin{bmatrix}\sigma_1\\ \sigma_2\\ \sigma_3\\ \tau_4\\ \tau_5\\ \tau_6\end{bmatrix} = \begin{bmatrix} C_{11} & C_{12} & C_{12} & 0 & 0 & 0 \\ C_{12} & C_{11} & C_{12} & 0 & 0 & 0 \\ C_{12} & C_{12} & C_{11} & 0 & 0 & 0 \\ 0 & 0 & 0 & \frac{C_{11}-C_{12}}{2} & 0 & 0 \\ 0 & 0 & 0 & 0 & \frac{C_{11}-C_{12}}{2} & 0 \\ 0 & 0 & 0 & 0 & 0 & \frac{C_{11}-C_{12}}{2} \end{bmatrix} \begin{bmatrix}\epsilon_1\\ \epsilon_2\\ \epsilon_3\\ \gamma_4\\ \gamma_5\\ \gamma_6\end{bmatrix} \tag{2.14}$$

Maintaining the assumption of plane-stress, valid at the lamina level, 4 equations are obtained,

$$\begin{aligned} \sigma_1 &= C_{11}\epsilon_1 + C_{12}\epsilon_2 + C_{12}\epsilon_3 \\ \sigma_2 &= C_{12}\epsilon_1 + C_{11}\epsilon_2 + C_{12}\epsilon_3 \\ \tau_6 &= \frac{C_{11} - C_{12}}{2}\gamma_6 \\ 0 &= C_{12}\epsilon_1 + C_{12}\epsilon_2 + C_{11}\epsilon_3 \end{aligned} \tag{2.15}$$

Recovering the method used for orthotropic materials, the system equations 2.15 can be written as,

$$\begin{aligned} \sigma_1 &= (C_{11} - \frac{C_{12}^2}{C_{11}})\epsilon_1 + (C_{12} - \frac{C_{12}^2}{C_{11}})\epsilon_2 \\ \sigma_2 &= (C_{12} - \frac{C_{12}^2}{C_{11}})\epsilon_1 + (C_{11} - \frac{C_{12}^2}{C_{11}})\epsilon_2 \\ \tau_6 &= \frac{C_{11} - C_{12}}{2}\gamma_6 \end{aligned} \tag{2.16}$$

Therefore, the entries of the reduced stiffness matrix, [Q], under plain-stress are,

$$\begin{aligned} Q_{11} = Q_{22} = C_{11} &= \frac{E_r}{1 - \nu_r^2} \\ Q_{12} = Q_{21} = C_{12} &= \frac{\nu_r E_r}{1 - \nu_r^2} \\ Q_{66} = \frac{C_{11} - C_{12}}{2} &= \frac{E_r}{2(1 + \nu_r)} \end{aligned} \tag{2.17}$$

where the subscript r corresponds to the Resin's properties.

2.3 Macrostructure

The mechanical behaviour of composite laminates is estimated taking into account the Classical Lamination Theory (CLT). For this, an initial strain/displacement field, consistent with the applied load, is assumed and through appropriate constitutive laws, the stress field is estimated. Moreover, loads in each lamina are calculated by satisfying the equilibrium of loads.

For plates subjected to small deformation the Kirchhoff hypothesis should be verified[34],

- Laminate deformations occur in the elastic domain;
- Deformations are continuous throughout the thickness;
- Each lamina is mechanically orthotropic and the distribution of the fibers within the resin medium is impossible to identify. The lamina is therefore homogenized in its properties;
- Plane sections that are initially normal to the mid-plane surface, preserve this condition after

loading;

- Deflection of the mid surface is negligible when compared to the thickness of the laminate;
- Shear strains, γ_{xz} and γ_{yz} , are negligible (γ_{xz} = $\gamma_{yz} = 0$);
- Thickness of the plate is much smaller than the width and length, so that plane stress is applied, $\sigma_3 = 0, \tau_4 = \tau_5 = 0$;

The laminate's loads and momentum are given according to the conventions illustrated in figures 2.2 and 2.3, respectively.

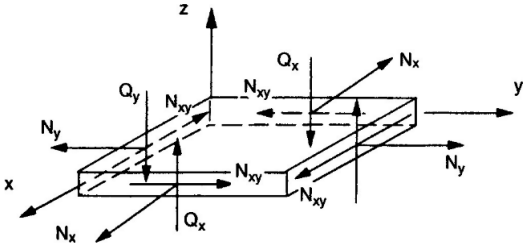

Figure 2.2: Laminate Load[34]

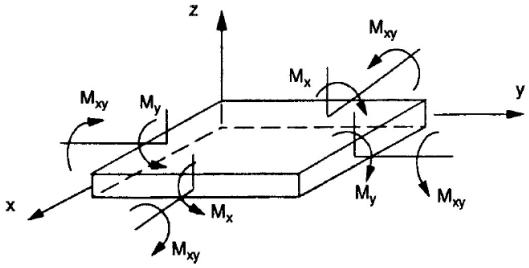

Figure 2.3: Laminate Momentum[34]

In order to satisfy equilibrium conditions, the loading and momentum must be balanced with the integral of stresses along the thickness. This can also be expressed as a sum of the stresses along the thickness of each layer, where m is the number of plies in the laminate.

$$\begin{bmatrix} N_x \\ N_y \\ N_{xy} \end{bmatrix} = \int_{-h/2}^{h/2} \begin{bmatrix} \sigma_x \\ \sigma_y \\ \tau_{xy} \end{bmatrix} dz = \sum_{k=1}^{m} \int_{z_{k-1}}^{z_k} \begin{bmatrix} \sigma_x \\ \sigma_y \\ \tau_{xy} \end{bmatrix}_k dz \tag{2.18a}$$

$$\begin{bmatrix} M_x \\ M_y \\ M_{xy} \end{bmatrix} = \int_{-h/2}^{h/2} z \begin{bmatrix} \sigma_x \\ \sigma_y \\ \tau_{xy} \end{bmatrix} dz = \sum_{k=1}^{m} \int_{z_{k-1}}^{z_k} z \begin{bmatrix} \sigma_x \\ \sigma_y \\ \tau_{xy} \end{bmatrix}_k dz \tag{2.18b}$$

By writing the previous equation as a function of the mid-surface strains and curvatures.

$$\begin{bmatrix} N_x \\ N_y \\ N_{xy} \end{bmatrix} = \sum_{k=1}^{N} [\bar{Q}]_k \Big(\int_{z_{k-1}}^{z_k} \begin{bmatrix} \epsilon_x^0 \\ \epsilon_y^0 \\ \epsilon_{xy}^0 \end{bmatrix} dz + \int_{z_{k-1}}^{z_k} z \begin{bmatrix} \sigma_x \\ \sigma_y \\ \tau_{xy} \end{bmatrix}_k dz \Big) \tag{2.19a}$$

$$\begin{bmatrix} M_x \\ M_y \\ M_{xy} \end{bmatrix} = \sum_{k=1}^{N} [\bar{Q}]_k \Big(\int_{z_{k-1}}^{z_k} z \begin{bmatrix} \epsilon_x^0 \\ \epsilon_y^0 \\ \epsilon_{xy}^0 \end{bmatrix} dz + \int_{z_{k-1}}^{z_k} z^2 \begin{bmatrix} k_x \\ k_y \\ k_{xy} \end{bmatrix}_k dz \Big) \tag{2.19b}$$

The results obtained until here can be comprised to a matrix form, as a function of the mid-surface strains and curvatures, and of the laminate's mechanical properties.

$$\begin{bmatrix} N_x \\ N_y \\ N_{xy} \\ --- \\ M_x \\ M_y \\ M_{xy} \end{bmatrix} = \left[\begin{array}{ccc|ccc} A_{11} & A_{12} & A_{13} & B_{11} & B_{12} & B_{13} \\ A_{11} & A_{12} & A_{13} & B_{21} & B_{22} & B_{23} \\ A_{11} & A_{12} & A_{13} & B_{31} & B_{32} & B_{33} \\ --- & --- & --- & --- & --- & --- \\ B_{11} & B_{12} & B_{13} & D_{11} & D_{12} & D_{13} \\ B_{21} & B_{22} & B_{23} & D_{21} & D_{22} & D_{23} \\ B_{31} & B_{32} & B_{33} & D_{31} & D_{32} & D_{33} \end{array}\right] \begin{bmatrix} \epsilon_x^0 \\ \epsilon_y^0 \\ \epsilon_{xy}^0 \\ --- \\ k_x^0 \\ k_y^0 \\ k_{xy}^0 \end{bmatrix} \tag{2.20}$$

where $\epsilon_x^0, \epsilon_y^0$ and ϵ_{xy}^0 are the mid surface strains and k_x^0, k_y^0 and k_{xy}^0 the mid surface curvatures. Moreover, the entries of the Extensional Stiffness matrix, [A_{ij}], the Extensional-bending stiffness matrix, [B_{ij}], and the Bending Stiffness matrix, [D_{ij}], are given by,

$$[A_{ij}] = \sum_{k=1}^{N} [\bar{Q}_{ij}]_k (z_k - z_{k-1}) \tag{2.21a}$$

$$[B_{ij}] = \frac{1}{2} \sum_{k=1}^{N} [\bar{Q}_{ij}]_k (z_k^2 - z_{k-1}^2) \tag{2.21b}$$

$$[D_{ij}] = \frac{1}{3} \sum_{k=1}^{N} [\bar{Q}_{ij}] (z_k^3 - z_{k-1}^3) \tag{2.21c}$$

where $[\bar{Q}]$ corresponds to the reduced stiffness matrix of the lamina in the loading direction and is computer by,

$$[\bar{Q}] = [T]_\sigma^{-1} [Q] [T]_\epsilon$$

The transformation matrices $[T]_\sigma^{-1}$ and $[T]_\epsilon$ have been previously described in equations 2.12b and 2.13a.

For a geometrically symmetric laminate, plies with the same orientation are at an equal distance of the mid-plane. Consequence of this symmetrically oriented plies is [B_{ij}] = 0;

Balanced laminates are obtained when, for a ply with the orientation θ, there is also ply with the orientation -θ. Therefore the entries relating the laminate's extension and distortion will be equal to zero due to the algebraic sum of symmetric terms, $A_{16} = A_{26} = 0$.

For balanced and symmetric laminates, the conjugation of the aforementioned effects is verified. In this work, only balanced symmetric laminates will be used, for which the aforementioned rules apply.

2.4 Stacking Sequence Type

2.4.1 Unidirectional Laminate

Unidirectional laminates (UD) consist on multiple layers of unidirectional laminae that are stacked in only one orientation, 0° or 90°. This type of laminates present high stiffness along the fiber direction ($0°$ direction), however possess lower strength and modulus in the transverse direction ($90°$ direction), as it is demonstrated in the results obtained in section 6.2.1.

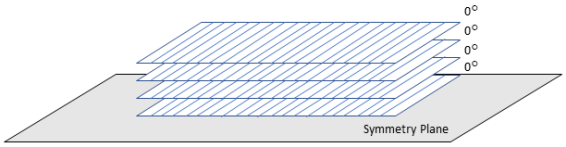

Figure 2.4: 8 layered unidirectional laminate ($UD(0)_8$)

2.4.2 Cross Ply Laminate

For Cross Ply laminates (CP), multiple plies are stacked with fibers oriented at $0°$ and $90°$, as illustrated in figure 2.5. For each ply, the entries of the reduced stiffness matrix, related to the coupling between extension and distortion are equal to zero. This implies that the entries 16 and 26 of the laminate's extensional stiffness matrix, [A], are zero. Moreover the following relations can be considered

$$\begin{aligned} \bar{Q}_{11}(0) = \bar{Q}_{22}(90), \quad \bar{Q}_{22}(0) = \bar{Q}_{11}(90) \\ \bar{Q}_{12}(0) = \bar{Q}_{12}(90), \quad \bar{Q}_{66}(0) = \bar{Q}_{66}(90) \end{aligned} \tag{2.22}$$

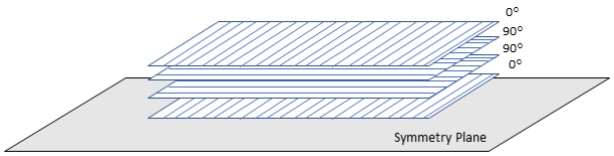

Figure 2.5: 8 layer symmetric Crossply laminate

2.4.3 Quasi-Isotropic Laminate

Quasi-isotropic laminates (QI) are groups of laminae that are stacked in a way to produce a material whose mechanical behaviour under in-plane loading is similar to an isotropic material. However, this does not apply for transverse loads or interlaminar shear, justifying the designation of quasi-isotropic, rather than isotropic since there is extension-distortion coupling in the extensional-bending and bending stiffness matrices, [B] and [D], respectively. Nonetheless, this stacking sequence leads to the generation of laminates with mechanical properties higher than some metals[35].

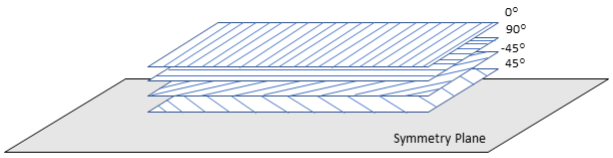

Figure 2.6: 8 layer symmetric quasi-isotropic laminate (QI(0,90))

Stacking of plies, in order to obtain a quasi-isotropic stacking sequence, some rules should be applied to the lamina's orientation[36], where n is a positive integer.

$$\left[0, \frac{\pi}{n}, \frac{2\pi}{n}, ..., \frac{(n-1)\pi}{n}\right], \quad n = 1, 2, 3, ...$$

Chapter 3

Digital Image Correlation

The first proposal for computer-aided 2D image processing in motion evaluation came from Peters and Ranson [37], in 1982. Through this work, the authors laid the basis for image correlation by suggesting an approach that uses fundamental continuum mechanics concepts for governing the deformation process of small regions in the sensors plane (designated as subsets), prior and after deformation. Since then, several authors have continued developing numerical algorithms for image correlation that would increase displacement measurement's accuracy and decrease computational times. Of these, gradient and coarse-fine search approaches were discussed by Tian and Huns [38] and demonstrated to provide sub-pixel accuracy for displacement measurements.

In order to optimize the image correlation process for displacement measurements, Sutton et al. [39] proposed a methodology based on the Newton-Raphson method for initial estimations of the displacement field, at each point. This method led to a severe decrease of the computational cost, while maintaining an optimal accuracy of the results. So far, the Newton-Raphson approach still remains the foundation of two-dimensional image correlation [10] and allowed a twentyfold speed increase when compared, at the time, with the remaining methodologies. The main parameters that affect 2D DIC accuracy, based on the previous method, have been demonstrated by Sutton et al. [40] to be related to the number of bits that are converted into digital values and the interpolation functions to reconstruct the intensity pattern at the sub-pixel locations.

Perfectly adiabatic thermoelastic effects are characterized by in-plane motions. Consequently, through-thickness motion evaluation (3D DIC) will be redundant for the present work. This leads to one big advantage regarding system calibration, since this procedure was experienced to be much simpler for only one camera (figure 3.7). Moreover, the employment of two cameras makes the system highly sensitive to the camera's motion due to the requirement that both cameras should have a certain yaw angle, usually 25°.

When compared with other interferometric optical techniques, 2D DIC presents several advantages

[41], namely

- Simple experimental setup and specimen preparation, since only one camera is required for deformation monitoring and the specimen's surface only requires to present a random gray distribution;
- Low requirements during measurements, i.e only a blue light (short wavelength) source irradiating at the material during measurement sequence;

However, some disadvantages can also be pointed out: measurement accuracy is dependent of the speckle pattern quality and imaging system quality and the fact that 2D DIC is susceptible to high errors due to out of plane motions and distortion effects since it induces erroneous image correlation, resulting in defects on the strain measurements.

3.1 Image Acquisition

For typical 2D DIC motion measurement, the axis of the camera's Charge Coupled Device/Complementary Metal Oxide Semiconductor (CCD/CMOS) sensor should be perpendicularly oriented to the sample's surface, as illustrated in figure 3.1.

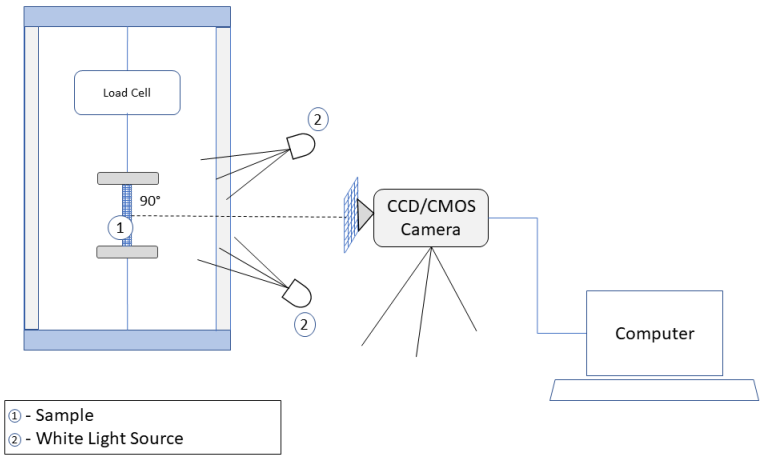

Figure 3.1: Illustration of a typical image acquisition system using two-dimensional DIC

The 2D DIC system follows gray intensity values given to each pixel based on a gradient between black and white. This intensity scale is dependent of the amount of bits the system's intensity resolution provides. When the light incident on a sensor is integrated over a fixed period, continuous intensity field reflected from the surface plane, O(x,y), is converted, by the imaging process of the camera's sensor, into a discrete integer intensity field, in the sensor plane I(x,y). Furthermore, the rectangular array of sensors converts the continuous intensity pattern, I(x,y) into a discrete array of integer intensity values in the sensor plane, I(i,j), where i and j correspond to the pixel's row and column number, respectively.

The basic principle of 2D DIC relies on the tracking and subsequent matching between images

taken in deformed configurations and an image taken in the reference stage. Initially, a calculation area denominated region of interest (ROI) is defined in the reference stage. This region is composed by several squared pixel areas (subsets) and the displacement field is calculated, in the subsets' centres, by computing the position in the reference stage and searching throughout the ROI for an optimal match. Let from now on, I(x,y) and I'(x,y) be the discrete integer intensity field in the undeformed and deformed conditions, respectively. Analogously, O(x,y) and O'(x,y) are the continuous intensity field, in the object plane, for the same conditions.

3.2 Mathematical Formulation for Image Matching

Considering a given subset with two points, m and n, of coordinates (x, y) and $(x + dx, y + dy)$, respectively, and m being the center of the subset under analysis, the continuously interpolated discrete intensity pattern, at this point, is given by,

$$I(m) = I(x, y) \tag{3.1a}$$

$$I(n) = I(x + dx, y + dy) \tag{3.1b}$$

where dx and dy are the small distances between m and n, in the sensors coordinate system.

Assuming the deformation at fields I and I' is given by the same deformations occurring in the object, the intensity pattern at the deformed configuration can be related to the reference configuration intensity pattern by a displacement vector field ($u(x, y)$,$v(x, y)$), so that the following relation is valid for transforming points m and n into their deformed states M and N, for which the discrete intensity field values yields,

$$I'(X, Y) = I(x + u(x, y), y + v(x, y)) \tag{3.2a}$$

$$\begin{aligned} I'(X + dX, Y + dY) &= I\big[x + dx + u(x + dx, y + dy), y + dy + v(x + dx, y + dy)\big] \\ &= I\Big[x + u(x, y) + \Big(1 + \frac{\partial u}{\partial x}\Big)dx + \frac{\partial u}{\partial y}dy, y + v(x, y) + \frac{\partial v}{\partial x}dx + \Big(1 + \frac{\partial v}{\partial y}\Big)dy\Big] \end{aligned} \tag{3.2b}$$

where $u(x, y)$ and $v(x, y)$ are given by a certain order-shape function, dependent of the deformation type,

- Zero-order shape: $u(x,y) = \xi$, $v(x,y) = \eta$
- First-order shape: $u(x,y) = \xi + \xi_x\Delta x + \xi_y\Delta y$, $v(x,y) = \eta + \eta_x\Delta x + \eta_y\Delta y$
- Second-order shape $u(x,y) = \xi + \xi_x\Delta x + \xi_y\Delta y + \frac{1}{2}\xi_{xx}\Delta x^2 + \frac{1}{2}\xi_{yy}\Delta y^2 + \frac{1}{2}\xi_{xy}\Delta x\Delta y$, $v(x,y) = \eta + \eta_x\Delta x + \eta_y\Delta y + \frac{1}{2}\eta_{xx}\Delta x^2 + \frac{1}{2}\eta_{yy}\Delta y^2 + \frac{1}{2}\eta_{xy}\Delta x\Delta y$

Considering the subset is sufficiently small so that the displacement gradient is constant throughout

the ROI, each pixel in the subset undergoes a uniform deformation, implying that the initial square shape subset is transformed into a parallelogram in the deformed configuration.

Determination of the parameters $u, v, \partial u/\partial x, \partial v/\partial x, \partial u/\partial y, \partial v/\partial y$ for each subset lies in the correct correspondence between the intensity signals in the initial and deformed stages (correlation function, $C(x, y)$). For this, several image correspondence methods have been proposed [10]

- Intensity magnitude value difference: $\sum_i |I'(N_i) - I(n_i)|$;
- Sum of squares of intensity value differences: $\sum_i (I'(N_i) - I(n_i))^2$;
- Cross-correlation: $\sum_i (I'(N_i)I(n_i))$
- Normalized cross-correlation: $\frac{\sum_i (I'(N_i)I(n_i))}{(\sum_i (I'(N_i)^2))^{\frac{1}{2}} (\sum_i (I(n_i)^2))^{\frac{1}{2}}}$

The correlation function establishes the correspondence between subsets in the reference and deformed configuration. The full Region of Interest (ROI) is evaluated searching for the optimal correspondence, which is given by the minimization/maximization of the correlation function, depending on the type of function used.

$$C(x,y) = 1 - \frac{\sum_{i=1}^{i=N} \sum_{j=1}^{j=M} I(x_i, y_j) I'(x_i + u_i(x_i, y_j), y_j + v_i(x_i, y_j)))}{\sum_{i=1}^{i=N} \sum_{j=1}^{j=M} (I^2(x_i, y_j) I'^2(x_i + u_i(x_i, y_j), y_j + v_i(x_i, y_j)))^{\frac{1}{2}}} \tag{3.3}$$

In the current work, the normalized cross-correlation function is used [42], equation 3.3, which also corresponds to the most commonly used in other DIC systems [10]. The optimization method which allows the minimization of the correlation function is the Newton-Raphson method since it provides appropriate computational times when compared with other methods [39], like the Levenburg-Marquardt.

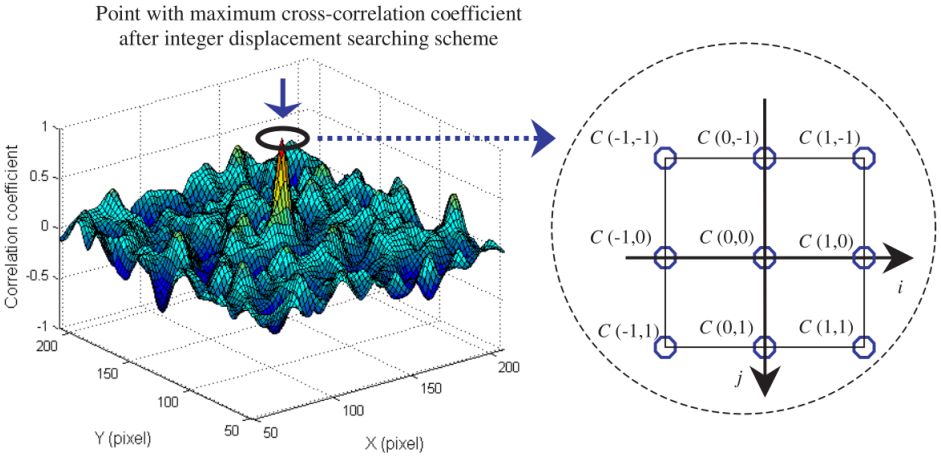

Figure 3.2: Subset cross-correlation match [41]

In the subset's deformed configuration, some of the points' coordinates might be located between pixels. Prior to the matching between undeformed and deformed configuration, a valid image correlation for these points should be obtained. Therefore, the DIC system interpolates the discrete intensity values,

in the sensor plane I(i,j), into a continuous map by employing interpolation functions. Some functions have already been suggested [10], such as the Bi-linear interpolation, Bi-cubic interpolation and Bi-cubic spline interpolation, illustrated in figure 3.3.

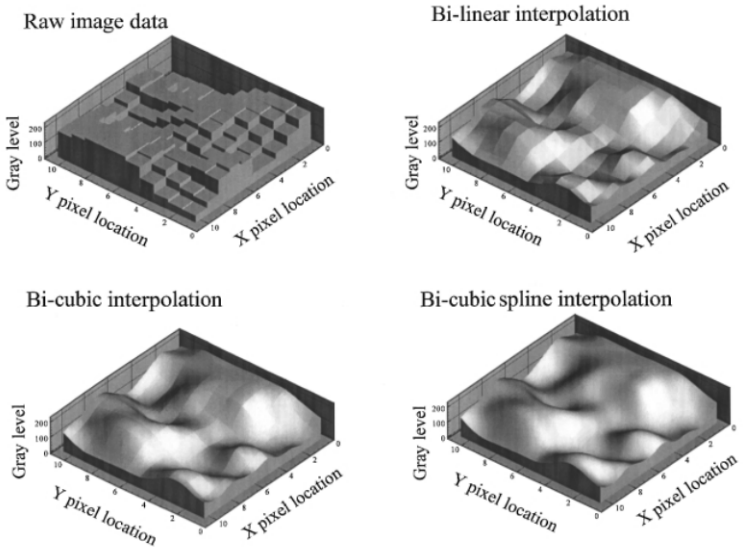

Figure 3.3: DIC interpolation method [9]

This section described the procedure for image matching during sample deformation measurements. The following section describes the displacement and strain field computation, respectively.

3.3 Displacement Field Measurement

Pixel-wise correspondence methodologies were proposed in the previous section. Due to the discrete matching nature of the presented methods, displacement calculation with 1 pixel accuracy can be easily computed. Introduction of sub-pixel accuracy for the displacement measurement requires two consecutive steps [41]: initial deformation estimation and sub-pixel displacement measurements.

Accurate initial deformation estimations are easily obtained by employing spatial or frequency domain search algorithms, throughout the vicinity of the subset center. Examples of employed search methods are, Coarse-to-fine method, for spatial domain, and Fast Fourier Transforms, for frequency (Fourier) domain [9]. The above methods have good performances for small deformations between subsets. However, difficulties arise for high displacements and rotations between images. For these, other techniques relying on multiple point matching are applied which translate in higher computational costs.

Conventional correlation calculation algorithms analyse the whole ROI, point-wise and along each row and column. In order to save computational times, the computed displacements and strains at the current point are used as initial estimations for the calculations of the next point, assuming continuous

deformations assumption [41]. This makes the conventional approach to DIC path dependent, which for large deformation or discontinuous areas, such as cracks and holes, makes the transfer of initial deformation might lead to error propagation for the case of wrong initial point measurement. Addressing this issue, reliability-guided DIC methods were proposed based on sum of squared differences correlation criterion for ordering the computed points.

For obtaining sub-pixel displacements accuracy, some methodologies have been proposed however, only the Newton-Raphson will be described considering the vast employment of this approach and the specific application to the present work.

3.3.1 Iterative Spatial domain cross-correlation algorithm

Considering the relative motion between the reference stage and target subsets in the deformed configurations, a non-linear relation is developed with respect to the desired mapping parameter vector [41]. If a first-order shape function is used, the mapping parameter vector is given by **p** = $(\eta,\eta_x,\eta_y,\xi,\xi_x,\xi_y)^{\mathsf{T}}$. The deformation vector, obtained using the Newton-Raphson method, can be obtained following the mathematical formulation,

$$\boldsymbol{p} = \boldsymbol{p_0} - \frac{\nabla C(\boldsymbol{p_0})}{\nabla\nabla C(\boldsymbol{p_0})} \tag{3.4}$$

where $\mathbf{p_0}$ is the present value for the point, **p** is the next iteration solution, $\nabla C(\boldsymbol{p_0})$ is the gradient of the correlation function and $\nabla\nabla C(\boldsymbol{p_0})$ is the Hessian matrix of the correlation function. Further approximations have been proposed for the Hessian matrix and improvement of computational times.

3.4 Strain Field Measurement

The displacement fields are calculated through the previously described methodology which is incorporated in most DIC systems nowadays[42]. However, in many experimental applications, such as structures stress analysis, computation of the strain field is more desirable and significant.

For strain field measurements the local least-squares fitting, proposed by Pan et al.[43], is usually employed and can be explained as follows.

For calculation of strain in a certain point, a square window is defined containing a certain number of points around the target point. For a calculation window small enough so that the displacement distribution can be approximated as linear plane, yielding

$$\begin{aligned} u(i,j) &= a_0 + a_1 x + a_2 y \\ v(i,j) &= b_0 + b_1 x + b_2 y \end{aligned} \tag{3.5}$$

where u and v are the original displacements, the entries (i,j) relate to the calculation window's

dimensions and $a_{0,1,2}$ and $b_{0,1,2}$ are coefficients. The displacement components have already been previously computed through the Newton-Raphson method and, since the locations of the sample are also known in the lens coordinate system, the previous system reduces to the computation of the equation's coefficients (a_0,a_1,a_2,b_0,b_1,b_2). Considering a window whose dimensions range from i = -m,...,m and j = -m,...,m then the displacement component, u, is given, in matrix form, by

$$\begin{bmatrix} 1 & -m & -m \\ 1 & -m+1 & -m \\ . & . & . \\ . & . & . \\ . & . & . \\ 1 & 0 & 0 \\ . & . & . \\ . & . & . \\ . & . & . \\ 1 & m-1 & m \\ 1 & m & m \end{bmatrix} \begin{bmatrix} a_0 \\ a_1 \\ a_2 \end{bmatrix} = \begin{bmatrix} u(-m,-m) \\ u(-m+1,-m) \\ . \\ . \\ . \\ u(0,0) \\ . \\ . \\ . \\ u(m-1,m) \\ u(m,m) \end{bmatrix} \tag{3.6}$$

Methods such as the least-squares method can be used to determine the equation's coefficients. However, it should be noted that the accuracy of the strain field calculation is highly dependent of the displacement fields' accuracy. Another important factor lies in the computation window's dimension, which can change according to the type of deformation occurring.

3.5 Displacement Measurement Errors

Error sources for 2D DIC displacement measurements can be divided into two categories [41]: errors related to specimen, loading and imaging and errors related to the system correlation algorithms.

The first category comprises errors related with the specimen preparation and system configuration and comprises aspects such as the Speckle Pattern quality, camera's sensor axis orientation, image distortion and noise during image acquisition. DIC measurements strongly rely on the speckle pattern quality since image correlation relies on the intensity signal from the sample. The surface pattern also is highly related with the subset's size, incorporated in the other category.

Other error incorporated in the first category relates with the relative orientation between the sample's surface and the camera sensor's axis. Deflections in this angle inferior to 5º lead to displacement errors lower than 0.01 pixels.

Another parameter influencing the measurements relates to the camera's noise. To mitigate the effect of this variable, blue source lights are employed during measurements, so that no fluctuation of illumination lightning occurs. Current DIC systems allow surface deformations field to be evaluated with an accuracy of $\pm$ 0.01 pixels [9] providing appropriate illumination conditions are fulfilled, since these are vital for accurate DIC measurements. Sutton et al. [10] stressed out the sensitivity of some of the correlation methods to the changes in lightning, which leads to considerable errors due to changes

in the background intensity levels. This also increases the correlation coefficient, translating in higher uncertainty regarding the subset matching. In tensile quasi-static tests of composite materials loss of lightning is not one of the prime concerns since the motion of the sample is done steadily and no sudden loss of illumination occurs. The same cannot be said for monitoring of mechanical phenomena such as buckling, where sudden changes in the material's shape occur and without proper illumination correspondence between the stages before and after buckling configurations may be invalid. Another alternative to address noise reduction consists in the usage of proper hardware, incorporated with effective cooling systems.

The second error category is related with the algorithm details. Parameters such as the correlation function, subset size, shape function and sub-pixel interpolation have an effect on the final displacement measurements and inaccurate definition of said parameters will result in wrong correlations.

During 2D DIC measurements the user should input certain specifications for the system to perform displacement measurements accurately. Selection of the subset size is strongly influenced by the speckle pattern quality, for which some methods have been proposed, in order to reduce errors from inaccurate selections. The subset size should be large enough so that a distinctive intensity pattern from other subsets is achieved. However, while small subsets displacement can accurately be approximated by first and second-order shape functions, larger subsets induce larger errors for the approximation of larger deformations. Moreover overly small subsets are prone to noise and interpolation errors [10]. Therefore a trade-off must be done in order to minimize errors.

This technique has been very useful for quantifying uniform macroscopic deformations in composite materials [13, 14]. However, its usage for assessing microscopic level deformation is rather limited due to the high deformation gradient at the interface between phases. This way, accurate assessment of strain is limited since current DIC systems average the displacement field in the window of analysis [12]. To address this issue, subset size should be reduce and the overlapping between subsets should be as high as possible, however this will increase the computational time abruptly. James et al. [44] developed a new methodology for image processing of in-plane motion for heterogeneous materials taking into account incorporation of SEM and optical photomicrographs with an error of ± 0.50 pixels.

3.6 DIC Experimental Setup

For displacement and strain measurements through DIC measurements during tensile tests, a GOM Adjustable 12M sensor system was used, for which a full illustration of said system is presented in figure 3.4. This system is composed by two cameras which allow 3D DIC displacement measurements. Since only 2D DIC measurements are required, only one of the camera was employed for the measurements. The left camera was chosen for such, due to positioning restrictions.

The **Teledyne Dalsa** camera possesses a CCD sensor, with maximum frame rate measurements

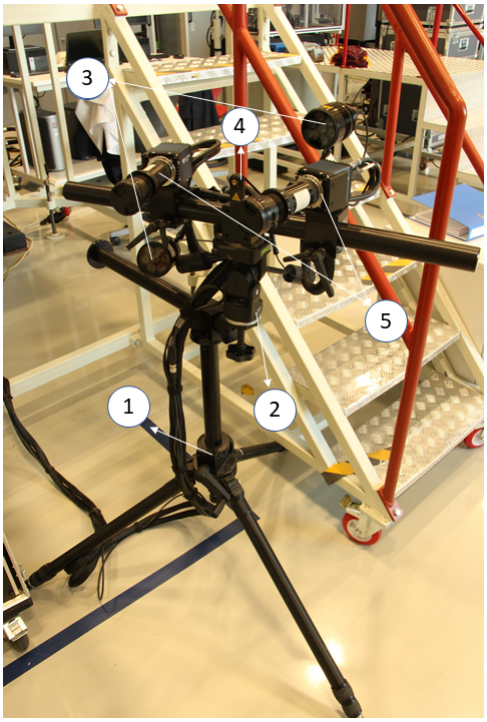

Figure 3.4: DIC setup: 1-**FOBA** tripod; 2-**Manfrotto** 229 Head; **GOM** adjustable base (3-high power led lamps; 4-laser); 5- **Teledyne Dalsa** cameras

of 25 fps and resolutions of 4096 x 3072 pixels and it's capable of detecting radiation with wavelengths between 400-700 nm (visible radiation spectrum).

3.7 ARAMIS Professional

For displacement tracking through 2D DIC measurements, the ARAMIS Professional software was used. The first step was verifying if the sample's dimension corresponds to the surface area correspondent to the recorded calibration (section B.4).

3.7.1 Sensor Calibration

A calibration of the camera's sensor is required in order to compensate the lens distortions due to vibrations during sample loading [9]. Calibration of the measuring system should be done before starting measurements for the first time, or if the camera is tilted.

Another benefit of employing 2D DIC in the measurements is the easier eye identification of decalibration based on the camera's angles. In 3D DIC, both camera's must present a "yaw" angle, which must align with the laser pointer, whilst in 2D DIC the camera lens should be parallel to the sample's surface which allows a much better standing of the camera.

Decalibration of the system might be indicated if the ARAMIS software illustrates many yellow facets

in the camera images after computation [45].

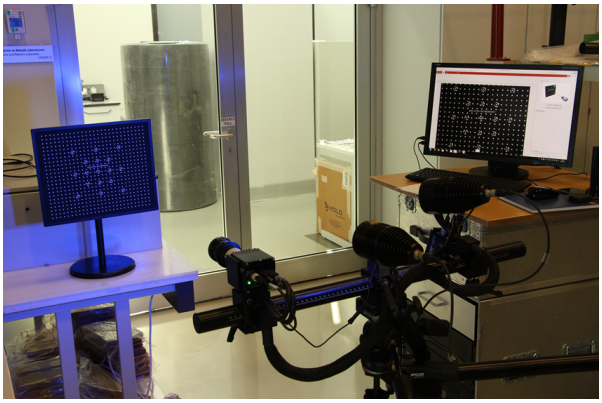

Figure 3.5: 2D DIC system calibration

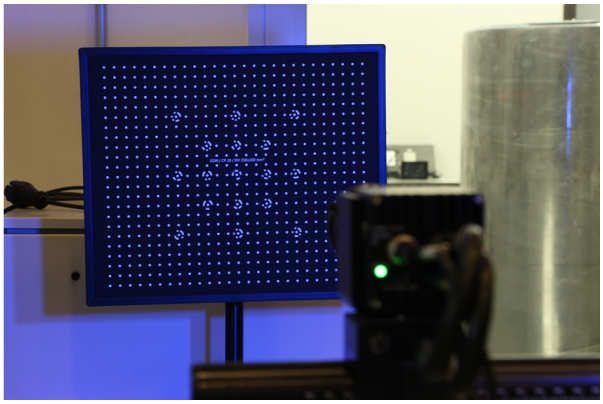

Figure 3.6: Calibration Panel

Figure 3.7: DIC system calibration

The calibration procedure comprises two distinct steps,

1. Lens Calibration, where the slider distance, the measurement distance, the focus and overexposure of the camera are adjusted according to the calibration sheet (figure B.4);
2. Sensor Calibration, through the rotation and tilting of the calibration panel;

The sensor calibration is done through the aid of a calibration panel (figure 3.6) with the appropriate dimensions input in the ARAMIS software. The first step of the calibration consists in the placement of the calibration panel at an appropriate distance from the sensor which is dependent of the measuring area and registered in the calibration sheet (figure B.4). Prior to the sensor calibration the camera's zoom and the overexposure should be corrected to the measuring distance and the desired frame rate.

Afterwards, following the software's instructions, the calibration panel was rotated and a sequence of pictures were taken for each panel orientation.

1. Orientation of the panel at $0°$;
2. Orientation of the panel at $90°$;
3. Orientation of the panel at $180°$;
4. Orientation of the panel at $270°$;
5. Tilting at $40°$ and rotation at $270°$;
6. Tilting at $40°$ and rotation at $0°$;
7. Tilting at $40°$ and rotation at $90°$;
8. Tilting at $40°$ and rotation at $180°$;

Consecutive single snap shots were taken at each step of the calibration with a resulting calibration deviation = 0.018 pixels (limit value: 0.050 pixels) and scale deviation = 0.002 mm (limit value: 0.022 mm), both these values are consistent with a good specimen calibration[45]. The calibration deviation is calculated from the average reference point deviation of all points recorded during the calibration process. The scale deviation translates the previous deviation into length units, according to the performed calibration.

3.7.2 Surface Component Definition

After the sensor replicates the image from the sample's surface, a reference stage (which can later be changed) is taken of the unloaded stage with the grips closed. Afterwards, the ROI (denominated Surface Component, in the ARAMIS software) will be defined which will restrict the deformation measurement algorithm to this region. In order to characterize the subsets within the ROI, the subset's size and the distance between subsequent subsets were defined (figure 3.8). Values which take into account speckle's quality are automatically given and can later be changed. For defining this parameter care should be taken given the already advantages and disadvantages mentioned in this chapter.

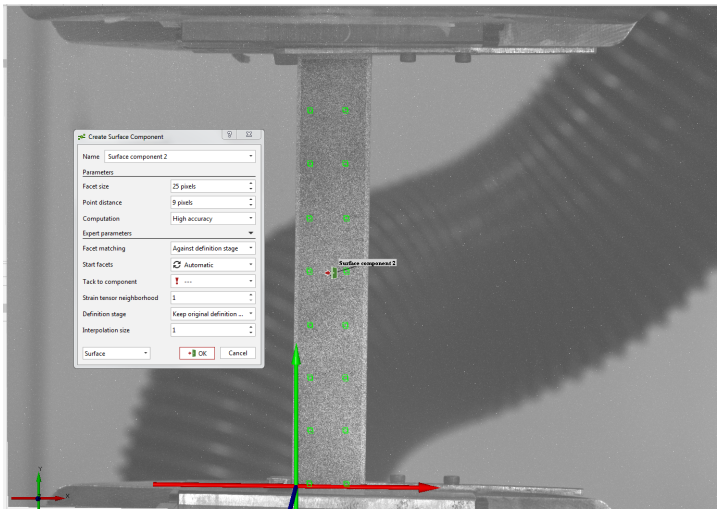

Figure 3.8: ARAMIS software: surface component defining

Measurements with dimensions equal to the ones used in the current work, a square subset, with a size and step size of 25 and 19 pixels, respectively, are usually employed. By decreasing the subsets size and distance between subsets' center a higher number of subsets is achieved and, consequently, the generated mesh after deformation tracking is refined. This might increase the accuracy of the results, however it also increases the computational time for displacement and strain calculation, besides the already mentioned disadvantages.

3.7.3 Stage Acquisition

Manual start and ending of the tests' image acquisition would lead to erroneous correlation, since initial and final images would not correspond to the exact load values for which correlation is to be made. Therefore, data acquisition needs to be synchronized with the Instron servo-hydraulic machine so that images referring to the desired limits. For this three conventional analog RG59 cables, with 75Ω resistance, were connected from the Instron console to the DIC system's channels. To channel 0 and 1, the Instron machine output 1V once the load reached the minimum measurement load value, while for channel 3 the same system output a value of 1V correspondent to the maximum load.

Figure 3.9 illustrates the stage acquisition definition for the image acquisition of the quasi-static tensile test. For this, three stages were defined. The first stage (*Start trigger*) refers to the initiation of the measurement, which corresponds to the minimum load value. The following stage (*Fast measurement*) relates to the image acquisition parameters, for which a frame rate of 0.5Hz were demonstrated to be sufficient for the current tests. The third and last stage (*Force*) corresponds to the interval for which the deformation measurement should be computed.

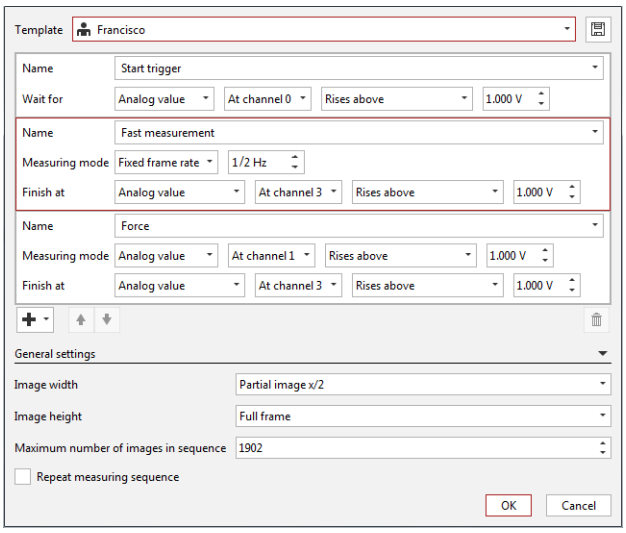

Figure 3.9: ARAMIS Professional stage acquisition definition

When acquiring each image, at the mentioned frame rate, the DIC system records the corresponding voltage value at each port. This proved to be extremely useful since it allowed the identification of the maximum and minimum load images, translating in more accurate measurements.

3.7.4 DIC Results Processing

The ARAMIS Correlate software was used for the post processing of the 2D DIC measurements. By defining the ROI, in the reference stage, a mesh, whose nodes correspond to the subsets' center, is generated (figure 3.10). This allows a better data manipulation since for each output, the ARAMIS system also outputs the node location, in reference to a given system of axes.

Figure 3.10: Surface Component Mesh

After mesh generation several parameters can be calculated. Of those, the strain components, ϵ_x and ϵ_y and γ_{xy}, are of prime importance for the work at hand. Calculation of the strain matrix in the loading direction, $[\Delta\epsilon]_{x,y}$, can be performed in relation to the reference stage or to a certain reference value.

According to the theoretical strain formulation of the thermoelastic phenomena for orthotropic materials, equation 1.3, the variation of strain, between the maximum and minimum applied load is required to estimate the temperature change in said test. By defining the reference stage as the figure correspondent to the minimum load, strain measurements will be given in relation to this configuration. Therefore, by investigating the configuration which corresponds to the maximum load, the strain in this stage will correspond to a variation between the maximum and minimum load configurations. Therefore, the values of $\Delta\epsilon_x$ and $\Delta\epsilon_y$ are obtained.

Chapter 4

Thermoelastic Stress Analysis

Thermoelastic stress analysis (**TSA**) was introduced as a non-destructive, non-contacting SHM technique, with its first usage reported in 1982 owed to the development of the SPATE system in conjugation with the thermoelastic formulation deducted by Thomson [19]. In the forthcoming years, major technological developments in infrared detectors led to an increased interest in the employment of this technique for material's structural integrity evaluation. Shifting from SPATE to focal-plane array (FPA) systems resulted in increased sensor's temperature sensitivity, reduced observation times and decreased system's weight due to the absence of an external cooling system [46].

Potter and Greaves [47] were amongst the first to apply TSA to fiber-reinforced composites by using a SPATE system. These authors addressed many important aspects which are still being referenced today, namely the influence of the resin-rich layer of composite laminates in the measured thermoelastic response and exclusion of temperature dependent terms, in the thermoelastic equation.

Dunn et al.[48] investigated the effect of the mean stress effect in aluminium alloys and graphite/epoxy composite materials. Samples were tested for frequencies of 10 and 30 Hz, for several mean stress values. The results obtained demonstrated to be very useful for the calculation of residual stresses in the material. Moreover, the author investigated the effect of the frequency in thermoelastic effect of aluminium samples, $[(\pm 45)_6]$ and $[(0^o,\pm 45^o)_s]$ graphite/epoxy composite materials. The authors verified that both the Aluminium and the $[(\pm 45)_6]$ sample provided similar responses for frequency changes and an approximately constant thermal response was obtained over 5Hz however, the $[(0^o,\pm 45^o)_s]$ sample presented contrasting phase angle response and didn't attain adiabatic conditions.

Finally, Wong[49] addressed the issue of non-adiabatic behaviour in Thermoelastic Stress Analysis of CFRP coupons with numerical and experimental work, namely by developing a mathematical formulation which would predict the temperature amplitude emission with increasing frequencies and the validation of these models in angle-ply and multi-directional laminates.

The aforementioned researches had a considerable impact for better understanding the thermoelastic phenomenon in FRPs. Further TSA researches can be found, in considerable amount, on the literature for characterization of different material's mechanical behaviour.

4.1 Non-adiabatic Effects

TSA in composite materials assumes the attainment of adiabatic conditions through the application of sufficient high frequency cyclic loads, in order for the temperature fluctuation, induced by stress/strain (equation 1.3), to be retained in the outer lamina. Therefore, investigation of the phenomena which could induce non-adiabatic conditions during measurements should be done. Analysing the boundary conditions of a test coupon installed in a servo-hydraulic machine, heat transfer can occur in three separate ways,

- Conduction between plies;
- Conduction between fiber and matrix;
- Convection between the atmosphere and the composite;

Wong[49] numerically compared the magnitude of the heat transfer through convection, in air, and conduction between plies and between matrix and fibers. For a heat transfer coefficient ranging from typical values of $h = 1W.m^{-2}.^{\circ}C^{-1}$ up to over two orders of magnitude, the heat transfer by convection proved to generate insignificant heat losses for loading frequencies over 5Hz.

4.1.1 Heat transfer between fiber and matrix

Large stress gradients exist, particularly in CFRPs, between the fibers and matrix, due to large discrepancies between the mechanical properties of these phases. This stress gradient occurs at the vicinity between these two phases and it is expected that different temperature fluctuations and heat transfer occurs. Therefore, the time-scale at which this phenomenon occurs should be determined so as to inspect the appropriate material's loading frequency.

During his numerical work, Wong [49] modelled the fibers as infinitely long circular cylinders, initially at thermal equilibrium and subjected to an imposed temperature boundary condition. The solution for the heat transfer equation is known and expressed as a series of Bessel Functions. Inspection of the Fourier number, Fo, of this solution, for which the heat diffusion is completed, the value of Fo = 0.8 was obtained. This implies that heat transfer would occur in 10^{-5} s which is lower than the load change period at 20 Hz($5.33 \cdot 10^{-3}$ s). Therefore, Wong concluded that approximately the same temperature fluctuations are originated in both phases despite the difference in mechanical/thermal properties.

4.1.2 Heat transfer between plies

Another heat transfer phenomenon to consider during TSA measurements of composite materials is the heat transfer occurring between plies. For unidirectional plies, the same orientation of the laminae allows generation of a uniform stress field within the laminate, provided no damage or voids are present. However, when stacking multi-directional plies, the stress state will differ from ply to ply. Higher difference in the laminae properties imply the increase of stress gradients, in the lamina's interface, which will increase heat transfer in the through-thickness direction.

Following the same methodology as in the previous section, the lamina was modelled as an infinitely long plate subjected to temperature changes in both of its surfaces. In this model, heat transfer is completed for Fo = 2, which corresponds to a time of 0.01s. This value is higher than the load change period. Therefore, Wong concluded that the temperature between different layers is not harmonized and adiabatic conditions cannot be fully attained for the usually applied frequencies during TSA measurements, in CFRPs. Meanwhile, Bakis et al.[50] verified that, in CFRPs, a continuous increase in the loading frequency above 35 Hz led to mechanical and electrical resonance. These effects induced considerable thermal response errors.

4.1.3 Loading frequency

Minimizing the non-adiabatic effects, referred in sections 4.1, requires the applied load to be cyclically changed at a time-scale small enough so that heat conduction effects are abated within the material's internal structure. As demonstrated in numerous researches[50, 51] the temperature amplitude emission in highly conductive, isotropic materials, such as Aluminium is constant for frequencies over 5 Hz. Moreover, in orthotropic materials, such as glass fiber-reinforced polymers, the temperature emission remains unchanged for frequencies between 10-15 Hz[52]. However, for CFRPs there seems to be a continuous increase of the thermoelastic response with the frequency[49, 50].

For multi-directional laminates, Wong[49] stated that the influence of the subsurface plies decreases with increasing frequencies. For this, a model was developed considering a finite plate, with time dependent temperature boundary conditions. Wong verified that for decreasing loading frequencies the signal difference between the one from the servo-hydraulic machine and the one from the SPATE system approach out-of-phase angles.

4.1.4 Epoxy Surface Layer

Current manufacturing processes generate an epoxy resin accumulation in the surface of the composite laminate. For increasing frequencies the heat generated due to the thermoelastic effect is retained in the outer surface ply[49], which due to the low conductive properties of the epoxy resin, translates in a temperature barrier and a delay of the thermoelastic signal's acquisition, in relation to the

reference signal. Such effect will increase the phase shift and decrease the temperature amplitude reading. Pitarresi et al.[53] investigated the effect of the resin rich-layer in the thermoelastic response of GFRPs and the hypothesis that, for these materials, the epoxy will behave as a strain witness of the laminate. For this, unidirectional plain weave E-glass/epoxy samples were manufactured and tested under load control. TSA measurements were performed using SPATE and DeltaTherm systems. The authors concluded that the influence of the strain witness model better fitted the obtained results. Moreover, it was concluded that, due to the higher thermoelastic constant, lower thermal conductivity and greater thickness, the resin-rich layer will demonstrate a strain witness behaviour for lower frequencies than a high emissivity black paint layer. The strain witness model proves extremely useful due to the simplification it induces in the TSA measurements of orthotropic materials, since an isotropic material is solely responsible for the thermoelastic signal generation.

For carbon/epoxy laminates, Zhang et al. [54], exploited the effect of the epoxy layer on the laminate's thermoelastic effect. By ranging the values of the resinlayer thickness, from 0 to 0.30 mm, the SPATE's signal was evaluated and concluded to stabilize for thickness higher than 0.03 mm. However, the effect of the strain witness behaviour has been proved by Pitarresi and Gallieti [23] to not have a high impact on the thermoelastic response of CFRPs due to the discrepancy between the fiber and matrix's properties.

4.2 Strain based Thermoelastic Equations

In section 1.4.2, equation 1.3 was presented as the extension of Thomson's formulation for orthotropic materials in matrix form,

$$\Delta T = -\frac{T_0}{\rho C_p}[\alpha]^T_{1,2}[\Delta\sigma]_{1,2}$$

Switching from stress- to strain-dependent thermoelastic formulations becomes a more meaningful approach. On one hand, strain data can be readily attained using strain gauges, extensometers and DIC. Moreover, multi-directional composite materials subjected to in-plane loading conditions will generate a lamina-dependent stress state, whilst strain remains constant throughout the thickness. Substituting 2.8b into 1.3 yields,

$$\frac{\Delta T}{T_0} = -\frac{1}{\rho C_p}[\alpha]^T_{1,2}[Q]_{1,2}[\Delta\epsilon]_{1,2} \tag{4.1}$$

Equation 4.1 can be also rewritten in the loading system of axes using 2.11a

$$\frac{\Delta T}{T_0} = -\frac{T_0}{\rho C_p}[\alpha]^T_{1,2}[Q]_{1,2}[T]_\epsilon[\Delta\epsilon]_{x,y} \tag{4.2}$$

The full matrix form of equation 4.2 is given by,

$$\frac{\Delta T}{T_0} = -\frac{1}{\rho C_p}\begin{bmatrix}\alpha_1 & \alpha_2 & 0\end{bmatrix}\begin{bmatrix}Q_{11} & Q_{12} & 0\\ Q_{21} & Q_{22} & 0\\ 0 & 0 & Q_{66}\end{bmatrix}\begin{bmatrix}c^2 & s^2 & 2cs\\ s^2 & c^2 & -2cs\\ -sc & sc & c^2-s^2\end{bmatrix}\begin{bmatrix}\Delta\epsilon_x\\ \Delta\epsilon_y\\ \Delta\gamma_s/2\end{bmatrix} \tag{4.3}$$

whose final form translates to,

$$\begin{aligned}\frac{\Delta T}{T_0} = -\frac{1}{\rho C_p}[&(\alpha_1 Q_{11}+\alpha_2 Q_{12})(\Delta\epsilon_x cos^2\theta + \Delta\epsilon_y sin^2\theta + \Delta\gamma_s cos\theta sin\theta)+\\ &(\alpha_1 Q_{21}+\alpha_2 Q_{22})(\Delta\epsilon_x sin^2\theta + \Delta\epsilon_y cos^2\theta - \Delta\gamma_s cos\theta sin\theta)]\end{aligned} \tag{4.4}$$

4.2.1 Orthotropic surface layer (Bulk model)

This model retains the mathematical formulation of the thermoelastic effect for orthotropic materials (equation 4.4) implying the thermal amplitude to be retained in the surface layer.

For a surface layer with fibers at 0° or 90°, under plane stress, equation 4.4 is reduced to the following

$$\begin{aligned}\frac{\Delta T}{T_0} = -\frac{1}{\rho C_p}[&(\alpha_1 Q_{11}+\alpha_2 Q_{12})(\Delta\epsilon_x cos^2(\theta)\Delta + \Delta\epsilon_y sin^2(\theta))+\\ &(\alpha_1 Q_{21}+\alpha_2 Q_{22})(\Delta\epsilon_x sin^2(\theta) + \Delta\epsilon_y cos^2(\theta))]\end{aligned} \tag{4.5}$$

4.2.2 Resin-Rich layer model

Under the strain witness assumption, the thermoelastic response can be quantified using the mechanical and thermal properties of the external epoxy layer. Since the mechanical response of the external epoxy layer will be identical to the laminate's,

$$\Delta\epsilon_{xr} = \Delta\epsilon_{xc} \tag{4.6a}$$

$$\Delta\epsilon_{yr} = \Delta\epsilon_{yc} \tag{4.6b}$$

Considering the epoxy as an isotropic material, the following stress/strain relation can be written

$$\Delta(\sigma_x + \sigma_y) = \frac{E_r}{1-\nu_r}(\Delta\epsilon_{xc} + \Delta\epsilon_{yc}) \tag{4.7}$$

Replacing the above mentioned equality into equation 1.2 the resin-rich layer (RRL) model can be described as

$$\frac{\Delta T}{T_0} = -\frac{1}{\rho_r C_{pr}}\left[\frac{E_r\alpha_r}{1-\nu_r}(\Delta\epsilon_x + \Delta\epsilon_y)\right] \tag{4.8}$$

4.2.3 Homogeneous model

The material's thermoelastic response is assumed to be dependent solely of the laminate's extensional stiffness matrix $[A_{i,j}]$ and the global coefficients of thermal expansion, α_x and α_y

$$\frac{\Delta T}{T_0} = -\frac{1}{\rho C_p h}\left[\alpha_{xL}(A_{11}+A_{12})\Delta\epsilon_x + \alpha_{yL}(A_{12}+A_{22})\Delta\epsilon_y\right] \tag{4.9}$$

4.2.4 CTE coupled in the stack

The following formulation was proposed by Sambasivan[55] which assumes the thermal behaviour to remain constant throughout the thickness while retaining the mechanical response of the surface layer.

$$\frac{\Delta T}{T_0} = -\frac{1}{\rho C_p}\left[\alpha_{xL}(Q_{11}+Q_{12})\Delta\epsilon_x + \alpha_{yL}(Q_{21}+Q_{22})\Delta\epsilon_y\right] \tag{4.10}$$

Decoupling the lamina's CTEs from the reduced stiffness tensor's entries and combining them with the global CTEs is mathematically impossible. Hence, this model was not taken into consideration in further sections of this work.

4.3 Measurement Equipment

4.3.1 FLIR Camera

For thermal imaging acquisition, the FLIR x6580sc photon detector model (figure 4.1) was used. Photon detectors employ a semi-conductor which ionizes when receives the required energy to remove a valence electron from the atom. For an absorbed energy greater than the ionization one, an output voltage is generated and the temperature value of the object is obtained.

The FLIR x6580sc thermal camera possesses a digital focal plane array for temperature detection with an Indium Antimonide (InSb) sensor capable of measurements with IR resolution of 640$\times$512 pixels at a maximum of 355Hz frame rate. Temperature differences smaller than 20mK are usually detected with an accuracy of $\pm$1 mK. For this camera two types of lenses were provided, 25mm and 50mm lens.

As it was previously mentioned in section 1.5, sample's motion during TSA measurements might induce errors that are proportional to its displacement. In the absence of motion compensation software, a lower magnification lens, which enables a less narrow analysis window, and an accurate distance allows the minimization of these effects. Therefore, the 25 mm lens was chosen for all the TSA measurements with the lens glass tip at a distance of 73 cm from the sample.

Figure 4.1: FLIR x6580sc infrared camera with 25 mm lens

Signal-to-Noise ratio

The introduction of the SPATE allowed, for the first time, quantitative thermoelastic measurements. However, this system required large observation times and therefore, infrared imagers were the focus of several developments in the past decades. Of these, microbolometers and photon detectors emerged and have had particular importance for TSA measurements. The FLIR x6580sc infrared camera, used in this work, is inserted in the photon detector category, for which the dynamic response is given as a function of the integration time[46].

Compensation of the detector's variation of offset and gain requires employing a Non-Uniformity Correction (NUC). In the case of photon detectors, a Continuous Non-Uniformity Correction is employed, which relies on factory-assigned mapping of gain and offset corrections for a given integration time.

Accurate measurements require the noise influence on the measurements to be null or extremely low. For this, the signal-to-noise ratio value should be as high as possible. For this, the number of loading cycles required for a FLIR x6540sc model with an integration time of 2 ms, the signal-to-noise ratio has been demonstrated to stabilize at approximately 4000-5000 cycles[46]. Figure 4.2 represents the decrease of noise to signal ratio with loading cycles. Therefore the measurement duration for all TSA measurements was set to 300s, since at the working frequency provided enough cycles to obtain the desired conditions.

4.3.2 DisplayImg 6

IR image acquisition control was done by using **DigitalImg 6^{TM}** software, from **Edevis**. This software employs a Fast Fourier Transform (FFT) for analysing a reference signal, taken prior to the measurements, and computing its frequency prior to processing the thermal data, through a lock-in technique. For this, a 50Ω coaxial analog cable was connected from the Instron console to the camera's lock-in port, with a voltage amplitude range between 150mV and 10 V [56].

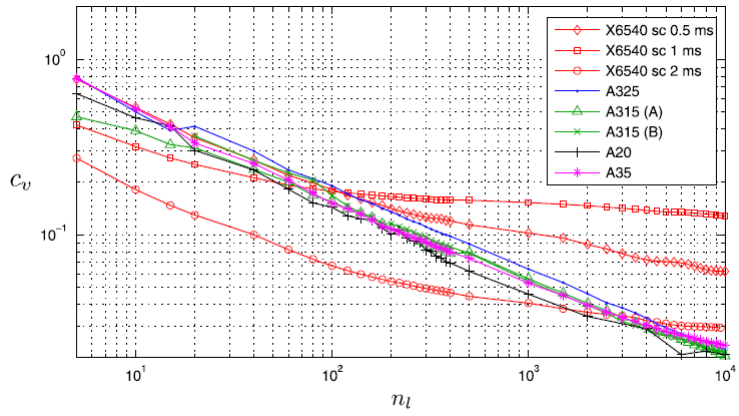

Figure 4.2: Noise-to-signal ratio as a function of the number of loading cycles[46]

Prior to the TSA measurement some inputs had to be defined according to the characteristics of each test,

- **Emissivity:** comparison between the power radiated from a real surface to the one radiated by a black body, at the same temperature and wavelength;
- **Frame Rate:** number of images captured and processed each second;
- **Integration Time:** the average time for capturing one picture (inverse of the frame rate);
- **Measurement Duration:** total time for the TSA measurement, including processing of all the thermal images;
- **Reflected Temperature:** temperature of the environment that is reflected by the sample to the IR camera. Temperature

Three essential outputs, pixel by pixel, came from this software after TSA measurements, with the respective pixel coordinates. Although only two contributed in a quantitative manner, the importance of the third parameter should not be discredited since it demonstrates the attainment of adiabatic conditions.

- **Temperature Amplitude:** In this document referred to as $\Delta T/2$ and corresponds to the average temperature amplitude due to thermoelastic effects;
- **Absolute Temperature:** Corresponding to the average absolute temperature;
- **Phase:** The angle correspondent to the phase difference between the applied load wave and the temperature wave the camera is reading.

Calculation of the phase angle was done using the lock-in technique, where comparison between the camera's signal acquisition and the reference signal, provided by the Instron servo-hydraulic machine allows estimating the phase shift between the two signals.

Chapter 5

Sample Manufacture

For choosing the material to address the problem at hand some points had to been taken into consideration, namely: the availability of the material at the research center; usage of the material in the aerospace industry and amount of TSA research performed on the material;

All the aforementioned requirements were fulfilled by employing CFRPs in this work, since all the manufacturing requirements for these materials were fulfilled at the research center and, as mentioned in chapter 1, this material has been extensively used for the manufacturing of aerospace structures (figure 1.1). Finally, no extensive TSA measurements for CFRPs are available in the literature, which incites the usage of this material for the present work.

5.1 Laminae Manufacturing

Synthesis of CFRPs can be done through different techniques, whose description requires the distinction between dry fibers and pre-impregnated (prepreg) fibers. Prepregs correspond to a thin layer of composite material, where the matrix and fibers are already mixed in a proportion controlled by the manufacturer. The laminate's manufacture, through stacking of these layers, resumes to the curing cycle of the epoxy resin. On the other hand, laminate's manufacturing using dry fibers should be done using Resin Transfer Methods (RTM and VARTM), with increasing number of instruments and additional concerns, followed by the cure of the resin in an oven.

Several types of resins were available for choosing, for which the selection was done according to the applications it provides. The OM10 epoxy resin [57] is presented for the usage on structural composites where high toughness is the main desired property. This resin was chosen since it provided properties similar to the ones yearned in aircraft components.

Each prepreg material has a specific code, independently of the manufacturer, where one can find

information regarding the specifications of the material.

For this work, the prepreg containing the code *KOM10 T700 12KT UD300 37 600 KOMP* was used, where

- *KOM10* indicates the manufacture and the type of epoxy used, where the letter *K* stands for the manufacturer (Kordsa) and *OM10* the type of matrix used;
- *T700* corresponds to the type of Carbon Fibers used,
- *12kt* corresponds to the amount of fibers (12k) in one Tow (t);
- *UD300* corresponds to the fiber's orientation (Unidirectional) and the fiber's lamina density (300 g/m^2)
- *37%* is the matrix specific volume percentage in the lamina;
- *600 KOMP* is the width (600 mm) of the prepreg roll;

Prepreg manufacturing process (illustrated in figure 5.1) involves stretching several fibers and placing them between two layers of matrix, following a set of steps until reaching the final product. One of the main advantages of this method is the automation inherent to it and the final product's quality is independent of the skill of a worker.

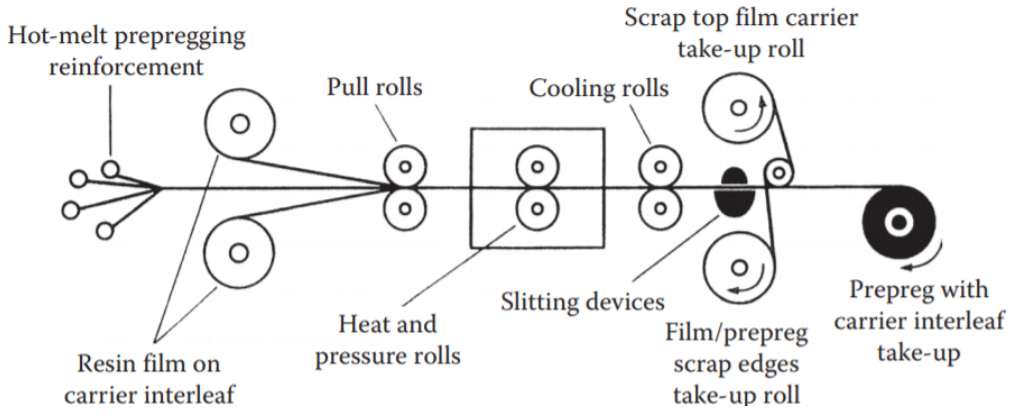

Figure 5.1: Manufacture process of CFRP prepreg [58]

The prepreg roll was later stored in a freezer at a temperature of -18°C in order to avoid material degradation due to deterioration of the adhesive between the resin and the fibers and to prevent the room temperature curing of the resin. The roll has a usage period of 1 year, at the previously mentioned storage conditions.

For the laminate manufacturing, the prepreg roll was placed at intermediate temperature conditions, between ambient temperature and the freezer temperature, 4°C, for over 12 hours in order to avoid large temperature gradients in the material while defrosting. Otherwise, residual stresses in the material would influence the measurements. Moreover, a gradual temperature reduction will ease the material

flexibility for later cutting and prevent water droplets from appearing on the prepreg's surface, which sharply deteriorates its properties.

5.2 Laminate Mnufacturing

After reaching ambient temperature, the prepreg plies were cut with the dimensions of 300×300 mm, correspondent to the necessary plate area for all the tests, using a **Zund D3** machine.

After obtaining the individual plies and stacking them in the desired sequence, cleaning of the steel moulding plates was done, which comprised,

1. Removal of dirt and/or epoxy leftovers, from previous manufacture, by using a Mold Cleaner;
2. Mould sealer was applied to both plates three times with an interval of 20 minutes between each application, in the horizontal and vertical directions;
3. Mould releaser was applied to ease the removal of the laminate after the curing cycle, in the same directions and time interval as before;

The prepreg stacking was then placed, with careful precision, in the center of one of the steel plates, as illustrated in figure 5.2

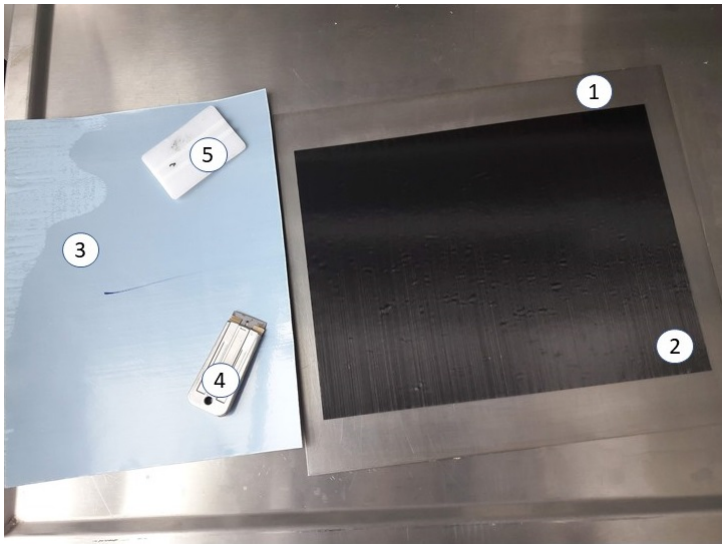

Figure 5.2: Hand lay-up of unidirectional laminae: (1) Steel Plate, (2) laminae stacking, (3) Remaining laminae, (4) Blade to ease the separation of the blue film and the material, (5) Tool for apply pressure to the laminae

Void percentage and delamination, in the laminate, due to weak bounding between plies can be reduced/avoided by applying considerable pressure when placing each lamina in the stacking.

5.2.1 Curing Cycle

Curing cycle corresponds to the set of stages characterized by different temperature and pressures distinct than the verified in standard conditions. These stages are named dwell periods and each one has a specific objective. The first dwell period allows the removal of entrapped gases while the second dwell period allows the enhancement of the laminate's mechanical properties.

The epoxy OM10 technical sheet provided two curing cycles, performed in two different devices, the autoclave curing and the hot press curing.

Most aerospace composites structures manufactured with prepreg laminae are cured using autoclaves [58] since this equipment allows improved mechanical properties, due to the highly controlled temperature and pressure environment it provides, which translates in laminates with enhanced mechanical properties and low void content. Nonetheless, due to the high energy involved in the curing and the complexity of the system, the autoclave curing reveals as the most expensive option for curing of the laminate due to the equipment it requires and the energy it consumes.

Since the amount of plates being manufactured were quite limited and done in a extended time span, the autoclave would constitute an expensive alternative for the resin curing. Meanwhile, the quality obtained using the hot press was acceptable for the current work, even though this machine does not allow the same control over the manufacturing as the laminate. Moreover, it allowes a more flexible manufacturing schedule. Therefore, the hot press was chosen to perform this task.

Figure 5.3: Hot Press Cure; 1- **TM-947SD** Thermometer, 2- Hot Press Panel; 3- Steel Plates

Figure 5.3 displays the **MSE LP_M4SH30** Hot Press for resin curing where, the digital panel illustrates the temperatures of the upper and bottom surfaces of the press and the pressure exerted by them. However, monitoring the curing temperature through this panels would not be accurate since the

laminate's temperature wouldn't be equal to the press surface. Heat transmission by conduction occurs until the laminate's temperature is equal to the machine surfaces. Therefore, for monitoring the epoxy's temperature a thermocouple was attached to the bottom part of the laminate, through an opening in the plate (figure 5.3), and connected to a **TM-947SD** thermometer.

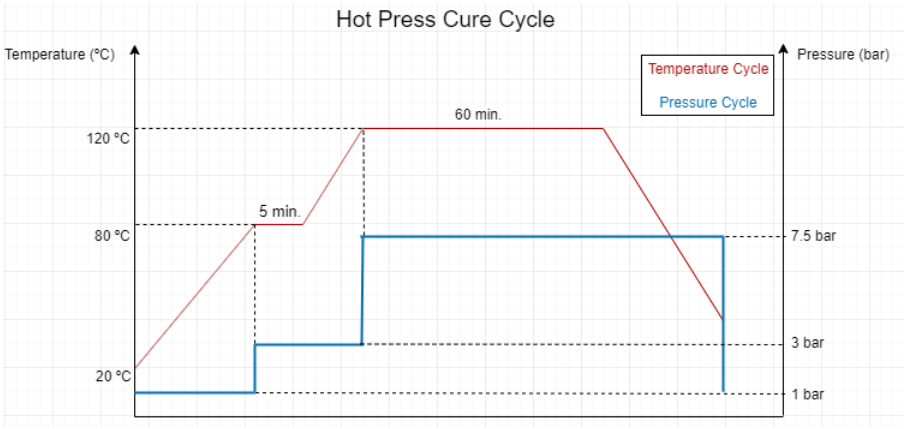

Figure 5.4: Hot press curing cycle for OM10 epoxy

The curing cycle of the OM10 epoxy (figure 5.4) started by placing the laminate and steel plates on the hot press and increasing their temperature to 80°C. After reaching this temperature, a pressure of 2.5 bar was applied through a lever which moves the top and bottom press surfaces closer to each other. The pressure exerted was monitored through a panel, visible in figure 5.3, in unit tons. This temperature and pressure conditions were kept for 5 minutes (first dwell period) after which the temperature was increased to 120°C and pressure to 7.5 bar (second dwell period) for 60 minutes.

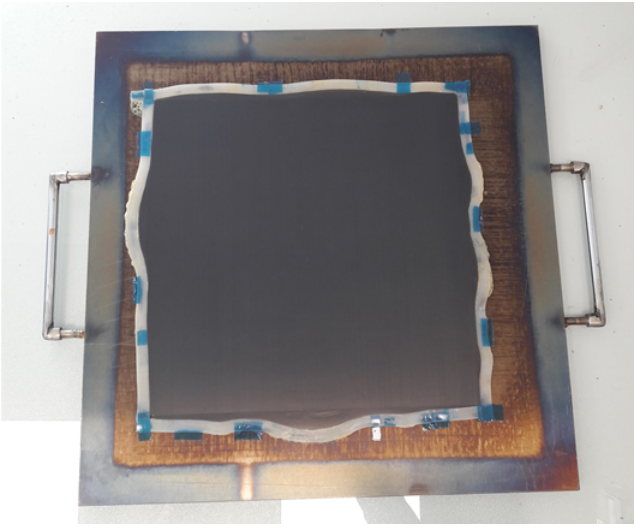

Figure 5.5: CFRP laminate after curing

After this period, the material was cooled smoothly (with cold water inside the hot-press surfaces) to ambient pressure, in order to reduce residual stresses due to high temperature gradients imposed on the laminate causing the laminate to warp. This effect might cause TSA measurements to be compromised

since temperature changes were not taking in relation to an unload state.

In figure 5.5 some resin spillage can be observed on sides of the laminate, as previously mentioned. This might lead to motion of the fibers, inducing internal defects and therefore, decreasing the laminate's quality. In order to mitigate this effect, silicon strips and, later on, metallic frames (with the internal area equal to the laminate's area) was used in order to prevent this resin spill.

5.3 Stacking Sequence

Multi directional laminates involve the stacking of laminae with different directions. Considering that the same material and manufacturing process should be kept to maintain the material properties, the unidirectional prepreg roll should be cut with different directions.

Stacking of the plies was done by considering the most common stacking sequences in the aerospace industry and previously used laminates in TSA researches.

Unidirectional fulfills the previous requirements since it has been of the most employed stacking sequences for TSA measurements and is widely used in the aerospace industry.

Quantitative TSA research has been done in quasi-isotropic GFRP laminates by Marques [20], mainly due to the usage of this stacking sequence in the aerospace industry.

For the evaluation of the surface layer effect, two Cross Ply laminates were manufactured with opposite orientation layers.

Laminate Type	Stacking Sequence	Code
Unidirectional	$(0)_8$	UD0
Cross Ply (0/90)	$(0,90_2,0)_s$	CP(0/90)
Cross Ply (90/0)	$(90,0_2,90)_s$	CP(90/0)
Quasi-Isotropic (0/45)	$(0_2,-45_2, +45_2,90_2)_s$	Q.I(0/45)

Table 5.1: Manufactured stacking sequences

Table 5.1 summarises the type of manufactured laminates, its stacking sequence and the respective code, which will be used from this section forward.

5.4 Voids and Other Material Defects

Material's manufacturing process isn't perfect for which some anomalies and defects are expected in the resulting component. In the manufacturing of composite materials these defects can be categorized in three different groups: matrix, fiber and interface defects [59]. The most common matrix defect are voids, which are inherent to the manufacturing process of composite materials.

Voids are a result of mechanical air entrapment during lay up and moisture absorption during material storage. High void fraction volume in the material will significantly affect the mechanical properties. Therefore, it is desirable to reduce presence of this defect in the material [60], since higher void volumes usually mean lower fatigue resistance, and increased variation or scatter in strength properties. Knowledge of the void volume of a composite material is desirable as an indication of the quality of the laminate's manufacture process.

5.5 Sanding and Tabbing

Tabbing of composite materials is not as straightforward as in the case of metals. A valid failure mode for uniaxial tests involves the breakage of the specimen in the middle of its gage section. This implies that the magnitude of the uniform stress state, in this section, will be higher than in any other location of the specimen, including the gripping areas.

Tensile and compressive testing of composite specimens involves attaching the material to the grips of a machine leading to generation of axial stress by application of shear forces along the specimen's surface, through friction, in both ends of the material. However, shear and transverse strength of unidirectional composite materials are much lower than the longitudinal strength. Therefore, premature failure of the material, might occur even when these stress components are much lower than the axial one.

To address the reduced strength, flat grip surfaces allow the application of uniform shear forces to the specimen and produce low surface damages. However, for flat surfaces the coefficient of friction decreases, making slippage between the specimen and the grips of the machine highly probable. In these conditions, high clamping load is required in order to prevent this effect. This translates in high through thickness load which the laminate's through thickness compressive strength [35], which would result in the specimen's crushing in the gripping area.

A possible solution for achieving all the aforementioned conditions is to apply a material with the same width (and thickness) as the sample, denominated tab. Tabbing allows the thickness tapering of the sample so that the central gage section presents a lower cross section than the specimen ends. Despite this, it can also induce stress concentration locations namely in its ends adjacent to the gage section which can be eased by tapering this location.

For this work, GFRP tabs (manufactured through RTM) were chosen since they provided the best overall results for transmission of loads [61], while providing an economic solution, in comparison with carbon or aluminium tabs.

Improving the adhesion between the tab surface and the sample will allow better load transmission, from the gripping area to the gage section. The sample's ends (with dimensions given by standard

ASTM D3039/D3039M) were sanded with a slightly rough sanding paper (figure 5.6) and an **Araldite 2011** glue was applied to increase the adhesion between the sample surface and the tab (figure 5.7).

The adhesive between the sample and the tabs was later left to cure for 12 hours before usage to minimize eventual failures in the tabbing region.

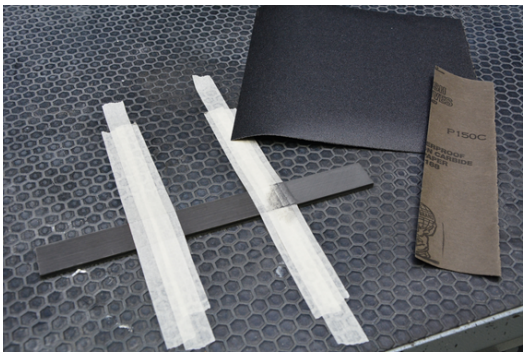

Figure 5.6: Sanding of CFRP sample

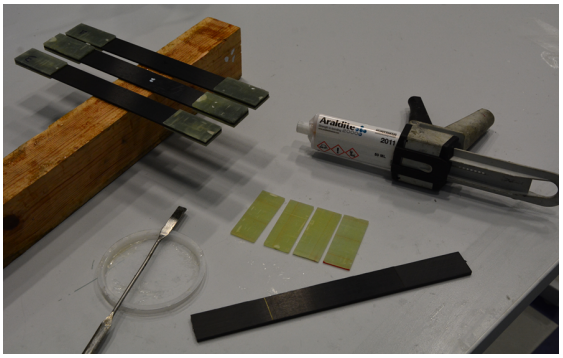

Figure 5.7: Tabbing of CFRP sample

5.6 Speckle Pattern

Displacement monitoring through DIC system requires the sample to present (or be painted with) a gray scale contour which allows the identification of subsets for motion quantification [9].

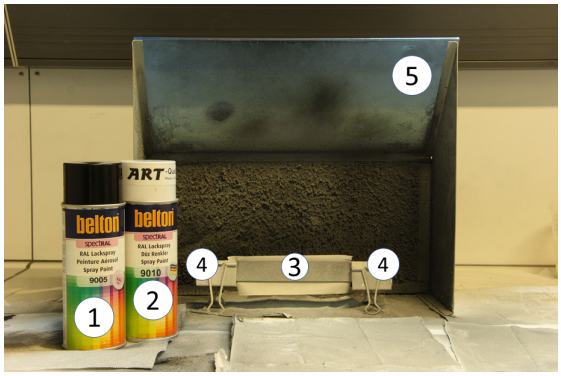

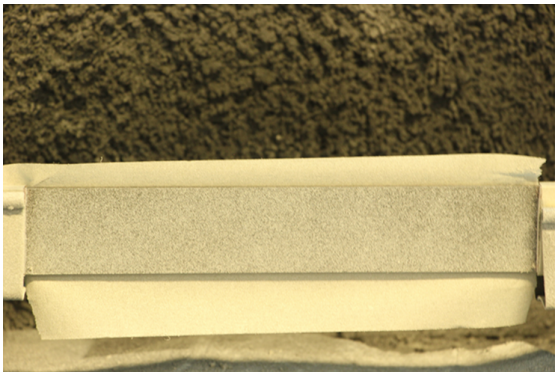

Figure 5.8: Speckle Pattern Paint; 1-Black Mate Paint, 2- White Mate Paint, 3- Sample Surface; 4- Grips, 5- Paint Box

Painting of the CFRP sample required the tabs to be protected with some tape (to avoid any measurements in the grip area) and only one side of the sample was painted and the orientation of the sample marked, for better identification, in case following repetitions were necessary.

Since the CFRP sample already presents a dark tone, the white paint was spread across with more intensity than the black one, thus ensuring the existence of dark spots in the white paint layer.

To ensure that the paint was quasi-homogeneously applied throughout the width, the sample was

elevated (with the aid of some paper grips in the tab region) and constant height was verified using a meter.

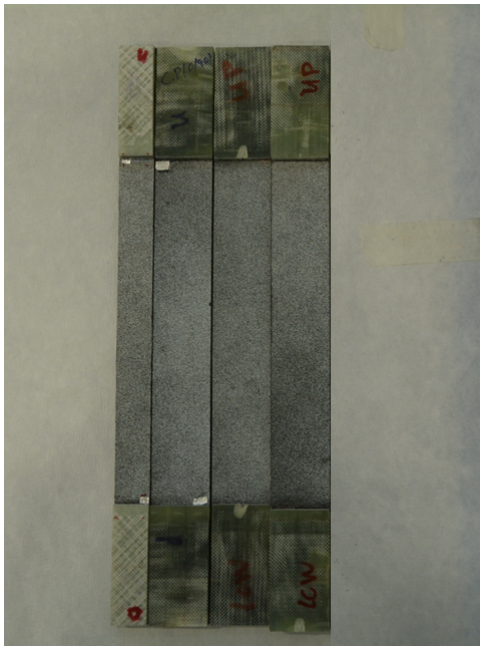

Figure 5.9: Different stacking sequences samples for testing

5.7 Epoxy Manufacturing

Evaluation of the resin rich layer model's influence in the laminate's thermoelastic response requires some of the epoxy's properties to be determined (equation 4.8). Therefore, samples of cured plain epoxy were manufactured through Resin Casting technique.

In this process, the resin was poured into a bucket and left to degas for approximately 5 minutes. The neat resin started an exothermic reaction, at room temperature, which made the resin solidify immediately. Degassing the resin was required to prevent the entrapment of gas bubbles after consolidation of the resin which would decrease its mechanical properties.

In the mould opening, two nozzles (with the surroundings covered with tacky tape for proper isolation) were introduced and the mould sides were closed and sealed. One of the nozzles was connected to the resin bucket and the other connected to a bucket where vacuum was applied through a pump.

The infusion of the resin took a couple of minutes after which the mould was introduced in the oven for proper resin curing.

Dog bone shapes were later cut and tested for tensile properties evaluation, according to ASTM D638-14 [62].

Chapter 6

Material Characterization

Quantitative thermoelastic measurements for orthotropic materials, using equation 1.3 require determining some properties related to the mechanical and thermal behaviour.

Density and specific heat (ρ_c and C_p, respectively) are material properties which depend solely on the manufacturing process and curing cycle of the epoxy. However, certain properties, such as the coefficient of thermal expansion in the loading direction (α_x and α_y) are dependent of the stacking sequence (table 5.1).

6.1 Microstructure Properties

6.1.1 Density

Calculation of the laminate's density was done following a hydrostatic weighting technique (illustrated in figure 6.1), used by Marques [52] and Sambasivam [55]. In this technique, due to the equilibrium of forces, the masses before and after immersing the sample in water ($m_{s,1}$ and $m_{s,a}$, respectively), relates to the composite's volume through the following relation,

$$\Delta m = \rho_w V_c \tag{6.1}$$

where $\Delta m = m_{s,a} - m_{s,l}$, ρ_w is the density of the water and V_c is the sample's volume.

Value for the density of the composite material is given by the ratio of the previously measured sample weight (m_s) to the calculated volume (V_c).

Five samples of a unidirectional laminate were cut with the dimensions of 25×25×2.125 mm^3, in order to obtain a higher amount of data and account with eventual discrepancies. Table 6.1 summarises the obtained results using a **Shimadzu AUX220** scale. Density measurements through this system take

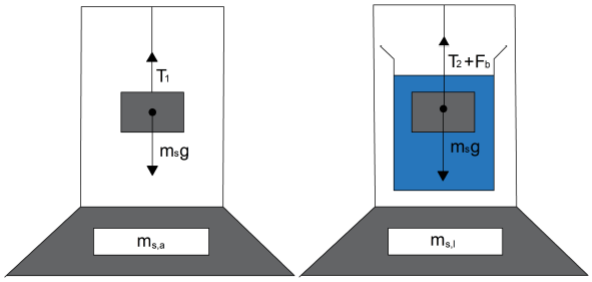

Figure 6.1: Density Measurement [52]

into account the hydrostatic weighting effect and are able to directly output the density value.

Specimen	Density [g/cm^3]
1	1.5111
2	1.5164
3	1.5170
4	1.5150
5	1.5219
Average	1.51628

Table 6.1: Laminate density results

6.1.2 Void Content

FRPs can be manufactured through several techniques, each carries inherent imperfections to the final laminate. Material imperfections such as voids can only be controlled to some extent by perfecting manufacturing parameters such as vacuum pressure, cure temperature, among others.

While FRPs usually present 2 different constituents, matrix and fibers, the presence of voids alters the volume percentage of each, altering the laminate's mechanical properties. Voids are locations of high stress concentration from where material imperfections start to propagate. Therefore, it has been the focus of some studies. Talreja [63] evaluated the detrimental effect of voids on the mechanical performance of composite materials, i.e impact on the elastic properties, delamination growth and intralaminar cracking. Laminates with a void percentage of 0.5% are considered to be well manufactured. However, this characterization is dependent on the application of such material and its requirements.

The assessment of the void volume fraction is done following standard ASTM D3171 - 15 [64] for which the procedure is dependent on the material type. Three specimens of unidirectional fibers 25 $\times$ 25 $\times$ 2.125 mm^3 were cut and tested, under *"Procedure H — Matrix Carbonization in a Nitrogen-Purging Furnace"*. Results obtained from this procedure are condensed in table 6.2 with the respective average value of 1% void volume ratio percentage. This evidences the good quality of the laminate's manufacturing process.

Specimen	Fiber Volume fraction(w_f)	Matrix Volume fraction (w_m)	Void Volume Fraction (w_v)	$\bar{w_v}$
1	0.542274	0.444882	0.012845	
2	0.579899	0.387671	0.03243	0.013064
3	0.556364	0.423591	0.020045	

Table 6.2: Void volume fraction of CFRP laminate

6.2 Mechanical Properties

6.2.1 Young's Modulus and Poisson's Ratio

For unidirectional composite materials, the lamina and laminate's system of axes are the same, throughout the thickness. Therefore, when a unidirectional composite material, with fibers along the longitudinal direction, is tested under traction, the only non-zero stress component is σ_1. The same argument can be made for unidirectional laminates, with fibers along the transverse direction, under tensile load, for which only σ_2 is non-zero.

For assessment of the stiffness modulus in the longitudinal and transverse direction, tensile tests were performed according to standard ASTM D3039/3039M [65]. By recommendation of this standard, five samples of unidirectional samples, with fibers along the longitudinal and transverse direction, were cut with the dimensions of 250$\times$15$\times$1 mm and 175$\times$25$\times$2 mm, respectively. For these tests, an Instron 5983 servo-hydraulic machine, equipped with a 100 kN load cell, was used and the material was tested at a displacement rate 2 mm/min [65]. In order to obtain values for the Poisson's ratio, displacement values in the longitudinal and transverse directions had to be calculated. Hence, three of the specimens were equipped with extensometer and the remaining two with strain gauges.

Strain gauges and extensometers are two devices that allow the measurement of the average local displacements (usually in the middle of the gauge length) of the material. While the first yields higher accuracy than the second, it also has a higher cost. This is the reason why only two samples, per batch, were attached with this instrument. Moreover, the test is conducted in a different way for each device. While for the strain gauge the test can be conducted uninterrupted, for the extensometers, the test had to be interrupted as the tensile strain reached 0.3%, at which the device was removed since an unexpected breakage of the material might lead to damaging of the measurement equipment.

Values for the stiffness modulus, in the fiber direction, E_1, and Poisson's ratio, ν_{12}, were obtained using the longitudinal fiber sample, $[0]_6$, while the transverse stiffness modulus, E_2, was obtained using transverse fiber samples, $[90]_8$

Values for ν_{12} were obtained directly from experimental data, by using biaxial strain gauge, while values for ν_{21} had to be obtained using orthotropic material properties. This was done as such since, due to the low tensile transverse strength of CFRPs, sample breakage could occur without surpassing the minimum reading displacement value for the biaxial strain gauge. Therefore, by attending to the equality between the entries 21 and 12 of the [A] matrix, for unidirectional laminates, ν_{21} is computed

by

$$\bar{A}_{12} = \bar{A}_{21} \Leftrightarrow \nu_{21} E_1 = \nu_{12} E_2 \tag{6.2}$$

and rearranging the previous equation, yields

$$\nu_{21} = \nu_{12} \frac{E_2}{E_1} \tag{6.3}$$

The epoxy resin was considered an isotropic material for which the stiffness modulus and Poisson's ratio assumes a constant value for every material direction, E_r and ν_r respectively. Values for the epoxy's mechanical properties were obtained by following standard ASTM 638-14 [62].

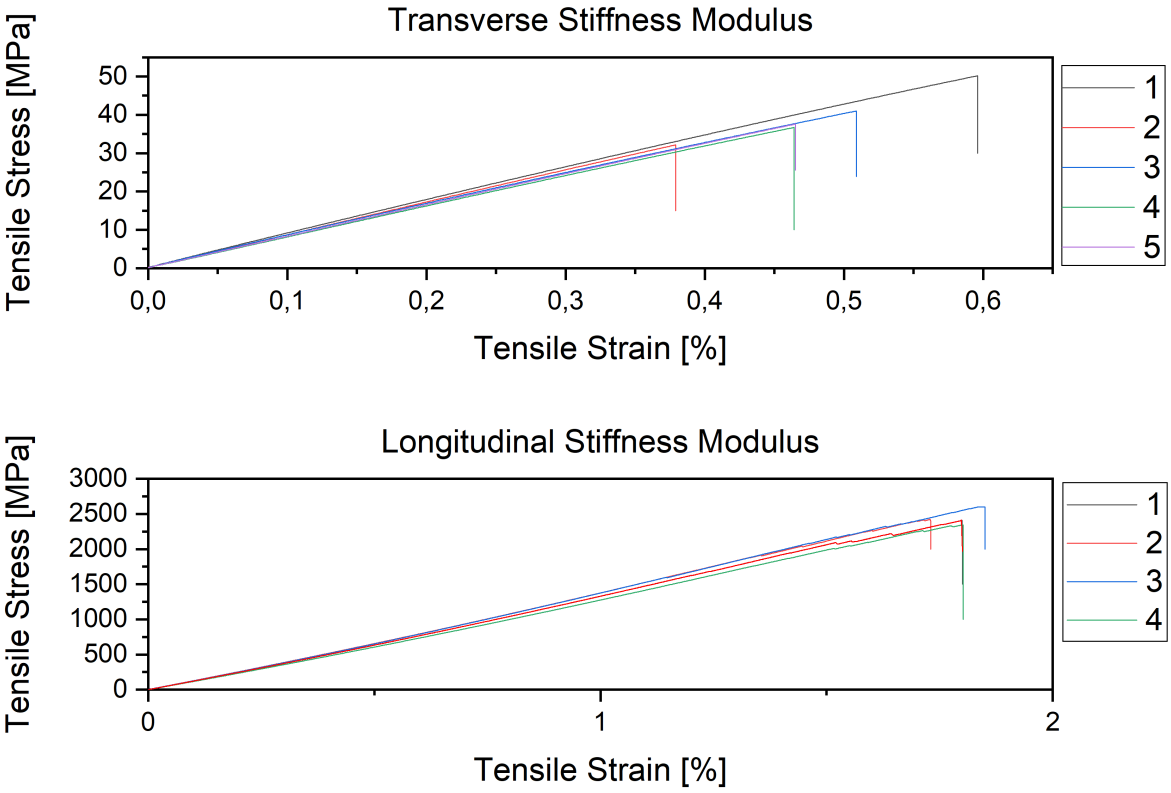

Figure 6.2: CFRP tensile test result

Figure 6.2 illustrates the tensile tests conducted according to standard ASTM D3039/D3039 M for the assessment of the stiffness modulus, in the longitudinal and transverse directions. Through analysis of this figure, one can identify the lack of plastic deformation, anticipated for unidirectional composite laminates.

Table 6.3 summarises the results obtained for the tensile tests.

	CFRP	Epoxy	Carbon Fiber
E_1 [GPa]	128.382	-	-
E_2 [GPa]	8.28432	-	-
ν_{12}	0.3	-	-
ν_{21}	0.01936	-	-
E_r [GPa]	-	3.5826	-
ν_r	-	0.39	-
E_f [GPa]	-	-	230

Table 6.3: CFRP and epoxy resin mechanical properties

6.2.2 Yield Point

Loading a material in the elastic region requires determination of the load value for which stress and strain are no longer characterized by a linear relation, i.e the material enters the plastic domain and deformations are irreversible. Different stacking sequences will allow manufacture of laminates with different stiffness and mechanical behaviour, which will behave differently when subjected to mechanical loading.

Following the same standard [65] as in section 6.2.1, the yielding point for different stacking sequences (table 5.1) was assessed. The samples ends were tabbed with GFRP tabs and mounted in an Instron 8801 servo-hydraulic machine. There was no need to employ additional strain measurement devices, like strain gauges, since strain evaluation was done using a video extensometer, already incorporated in the servo-hydraulic machine.

In table 6.4, summary of the results obtained for the tensile stiffness, maximum load and maximum tensile strain for each stacking sequence is presented. The corresponding test illustration is given by figure 6.3.

Stacking Sequence	E_1 [GPa]	P_{max} [kN]	ϵ_{max} [%]
$[0]_8$	129.14061	75.48170	1.617
$[0/90/90/0]_s$	75.86780	51.69043	1.274
$[90/0/0/90]_s$	53.55956	29.92065	0.916
$[0_2/\text{-}45_2/45_2/90_2]_s$	54.6704	77.394	1.696

Table 6.4: Yield point test results

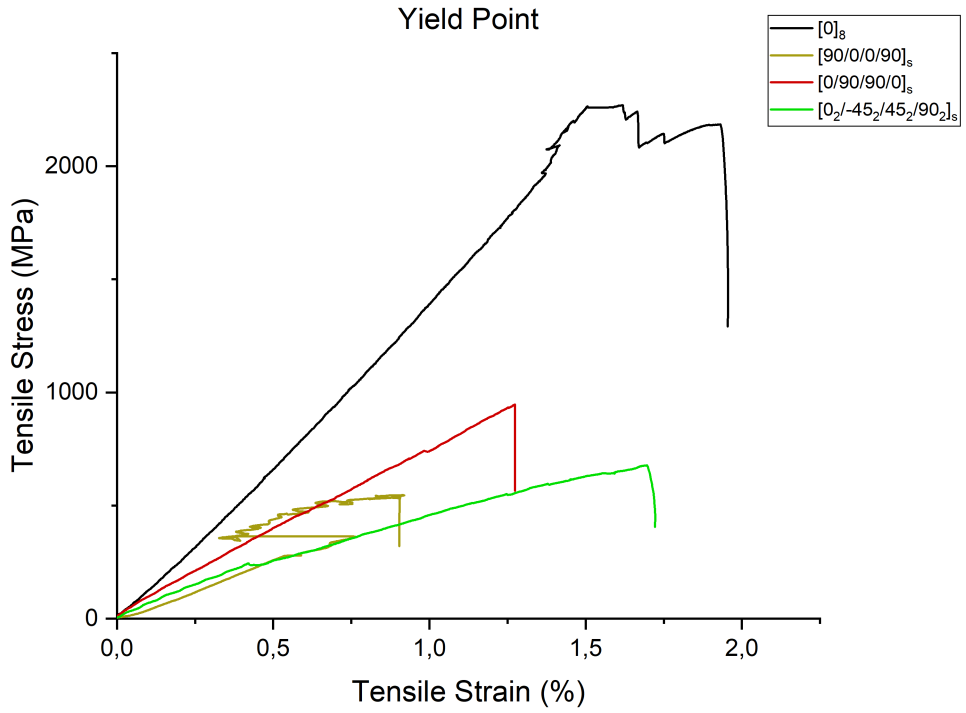

Figure 6.3: Yield point test for different stacking sequence

6.2.3 Shear Modulus

Calculations for the in-plane shear modulus were done following ASTM D5379 [66] using the same machine as in the tensile test. For this, 5 v-notched specimens were cut from a unidirectional laminate and placed on a special fixture which would apply a uniform shear force, while restricting bending motion.

Although, according to the standard [66], the stacking sequence that gave the best overall result for this kind of test is the $[0,90]_n$ laminate, this was also a laminate that had more resin spill and warping from the manufacturing process and therefore not appropriate for a correct assessment of mechanical properties. Unidirectional laminate, $[0]_8$, were used for the test giving an overestimate of 10% [66] for the shear modulus of the laminates which was later accounted.

Table 6.5 summarises the results obtained for during the test, using the Shear Chord Modulus Elasticity.

Specimen	G_{12} [GPa]	Avg [GPa]	Standard Deviation [GPa]	Coefficient of Variation
1	3.22480	3.57963	0.18944	5.29
2	3.732939			
3	3.57690			
4	3.58167			
5	3.74388			

Table 6.5: In-plane shear modulus result for CFRP laminate

6.3 Thermal Properties

6.3.1 Specific Heat Capacity at Constant Pressure

The amount of energy necessary to supply to a material, in order to change its internal temperature, at constant pressure, per unit mass, is denominated Specific Heat Capacity at constant pressure, C_p.

The procedure to calculate this parameter is described in standard ASTM E1269 - 11 [67], which relies on the usage of a Differential Scanning Calorimeter (Mettler Toledo DSC 3+ model). According to this standard, prior to the measurements, the calibration of the apparatus is performed using a synthetic sapphire disk for which the specific heat capacity for several temperatures is documented. No recommendation is done for the heat rate's value, only that the heating of the Saphire's sample and the specimen should occur at the same rate for a valid comparison to be obtained. In order to provide enough time span for the sample's temperature to stabilize, the rate of 0.5 K/min.

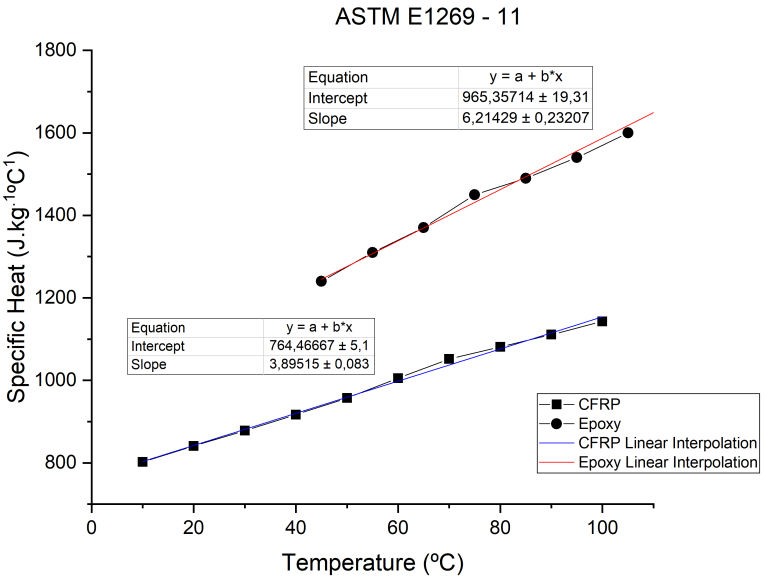

Figure 6.4: Specific heat coefficient curves for CFRP laminate and epoxy resin, for temperature range between 10 °C and 100 °C

The value of the specific heat capacity for the CFRP and epoxy specimen will be calculated as a function of the sapphire disk's specific heat capacity, the vertical distances between the curves of the generated graph and the specimen and sapphire disk's weight.

A note should be done regarding the value for the Saphire's C_p, which, for this test, had an average deviation of -7.1%, in comparison with the standard values.

Figure 6.4 illustrates the results obtained with the performed analysis. Thermoelastic effects in solid materials do not lead to large increases in the material's temperature so, for this test, C_p measurements were obtained for temperatures ranging from 10 to 100°C since it was certain that this temperature

range would not be exceeded.

6.3.2 Coefficient of Thermal Expansion (CTE)

The CTE, in a given direction, corresponds to the material's elongation when an increase of 1°C occurs in the whole body.

A thermomechanical analysis was performed using a **METTLER TOLEDO TMA/SDTA 2+** system, according to standard ASTM E831-14[68]. As recommended in this document, five samples with 5x5 mm in-plane dimensions were cut from an initial plate. The sample is placed in a holder with a temperature sensor at a reduce distance of the surface. Afterwards a force, between 1 and 100 mN, was exerted on a sensing probe to ensure the contact with the sample for displacement measurement This was followed by a heating of the sample at a rate of 5°C/min.

CTE calculation relied on the displacement measurement, as a function of the temperature, initial dimensions of the sample and the system's calibration coefficient.

Stacking Sequence	α_x [μm/m°C]	α_y [μm/m°C]
$[0/90/90/0]_s$	12.48	12.48
$[90/0/0/90]_s$	3.87	3.87
$[0_2/\text{-}45_2/45_2/90_2]_s$	7.65	7.65
$[0]_8$	0.55	27.4
Epoxy	66.0	

Table 6.6: CTE values for the different stacking sequences

CTE measurements through thermomechanical analysis are highly dependent of the materials surface condition since the displacement measurements are obtained through a sensing probe. For most materials this does not imply high CTE variations, however, for CFRPs, the high fluctuations of fiber/-matrix ratio provide different CTE values due to the already discusses mismatch between the resin and fibers CTE value.

Chapter 7

Local-Based Calibration of Thermoelastic Signal

7.1 Problem Statement

Standard TSA measurements involve the employment of strain gauges for obtaining the sample's average strain change during loading. These values are later translated into temperature ratio, $\Delta T/T_0$, by replacing the correspondent values in the thermoelastic models (section 4.2). Afterwards, by comparing the temperature ratio of each model (considered the theoretical values) with the average value obtained with the IR camera, a global characterization is obtained and the model which reveals the lowest error is assumed to describe the thermoelastic behaviour of the material.

Composite materials, due to their inherent heterogeneity, present different mechanical responses within its structure. Therefore, the usage of average values in these materials neglects the full-field characteristics of TSA and proves to under/overestimate the material's thermoelastic response. Switching from a global to a local calibration of the thermoelastic signal seems to correct these limitations. For this, incorporation of DIC provides a full-field calculation of the material's strain which, in concurrency with TSA, will allow a local-wise distribution of the thermoelastic response. However, DIC measurements during the dynamic test proved to generate files of considerable size and with low resolution, since the system cannot apply the same frame rates as the IR camera.

Nevertheless, TSA must be applied under very low load amplitudes so that the stress-strain behaviour lies within the linear elastic domain, where all deformations are reversible. Therefore, a quasi-static tensile test which is performed between the same load intervals as the dynamic test will have equivalent deformation and provide full-field strain change values which are representative of the changes occuring in the dynamic test.

7.2 Preliminary Tests

7.2.1 Emissivity

Radiation can behave differently when acting on a body, either it is transmitted, emitted, absorbed or reflected. According to Kirchhoff's law, the spectral emissivity is equal to the spectral absorvence of a body (valid for any material), at any specified temperature and wavelength[69]. For this work, only the notion of temperature emission will be developed in length.

Bodies whose temperature is higher than 0 K emit radiation in the infrared wavelength. Black bodies are ideal emitters since radiation is equally emitted in every direction with constant magnitude. However, radiation emission from real surfaces does not occur with the same characteristics. Therefore, in order to account with this difference, the emissivity parameter, e, has been proposed and is calculated as the ratio of the radiation emitted by a real surface to the one from a black body.

The emissivity value of the body under observation by the thermal camera is a parameter which should be input for an accurate correlation between the energy absorbed from the photons and the surface temperature by using the Stefan-Boltzmann law. Although this parameter is of vital importance in TSA measurements, several values are proposed in the literature. In order to obtain a consensual and fixed value for this parameter a test was performed, following the methodology described by Marques [52]. For calculating the emissivity value for the CFRP sample, with and without the speckle pattern, a unidirectional laminate with 1 mm of thickness was manufactured. The reduced thickness was chosen so that the temperature homogenization within the laminate would occur at a higher rate.

Later, the following materials were attached to the sample (figure 7.1), in the vertical direction,

1. Aluminium foil;
2. CFRP surface (Epoxy layer);
3. Black 3M tape;
4. Speckle Pattern surface;

The Aluminium foil was incorporated in this experiment due to its lower emissivity[69]. Therefore, temperature readings in this area should be lower when compared to the remaining materials. On the other hand, the Black 3M tape possesses a high emissivity due to its dark colour, consequently this material will be representative of a black body behaviour.

The CFRP sample described above was positioned inside a Vötsch VC^3 7150 climate test chamber. Afterwards, the oven temperature was increased to 30 K higher than room temperature. Higher temperature would generate temperature gradients which would be undesirable for the current test. This temperature was left to stabilize for 30 minutes to ensure temperature homogenization along the thickness. For recording the sample's temperature, the FLIR thermal camera was positioned, with a tilted

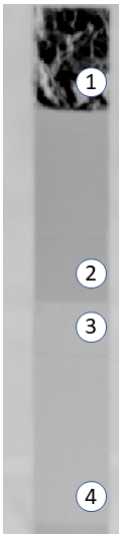

Figure 7.1: Thermal image of the emissivity sample

angle to avoid the Narcissus effect, at a distance of 75cm from the chamber's opening, to avoid readings close to this location given that high temperature gradients occur due to temperature differences inside and outside the oven. This method comprised static temperature measurements, for which the 50mm lens was chosen to be incorporated in the readings, seeing as no motion occurred that would compromise temperature measurements.

Determining the emissivity of the sample comprised consecutive readings, at constant oven temperature and changing the emissivity parameter on the **DisplayImg 6** software. The input emissivity value was assumed to correspond to the 3M black tape and the same averaged temperature reading should be measured in the Epoxy and Speckle Pattern area for its respective emissivity value. For each emissivity value, the average temperature readings on the ROI, correspondent to each material's area on the sample, is summarised in table 7.1.

	$\bar{T}$(ºC)			
e	1	2	3	4
0.93	45.78	55.38	55.25	53.98
0.94	44.83	56.09	55.89	54.28
0.95	51.28	61.09	60.90	60.10
0.96	44.20	55.72	55.57	54.18
0.97	46.43	55.02	55.02	53.44

Table 7.1: Average surface area temperature for different black tape emissivity

Analysis of table 7.1 it's reasonable to assume that even though, at the time of the measurements the value of the emissivity of the black tape was unknown, the emissivity of the speckle pattern is higher than the 3M black tape. Further literature review[56], after the test was performed revealed the

emissivity value of 0.96 to the M3 tape which increases the reliability of the obtained results.

Figure 7.2 summarises the difference of temperature amplitude measured by the FLIR camera between the Epoxy and the Speckle Pattern. The values of 0.95 and 0.97 were used for the emissivity of the Epoxy and Speckle Pattern, respectively.

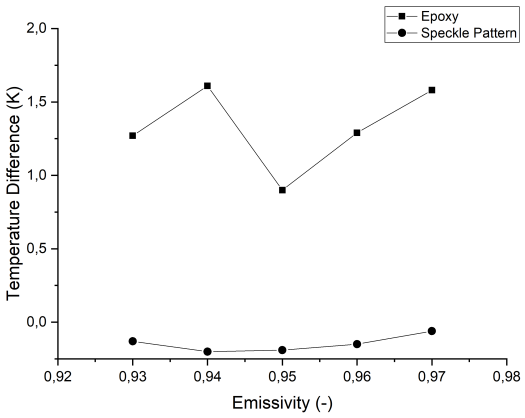

Figure 7.2: Average temperature difference from Epoxy and Speckle Pattern surface to the 3M black tape

Metals are characterized by a low emissivity value (e = 0.3, for most Aluminium alloys [56]), and therefore, high emissivity surface coatings, usually consisting of black mate paints, should be applied for allowing quantitative TSA measurements. On the other hand, as concluded by this chapter, composite materials, with a surface layer constituted of Epoxy possess a high emissivity value and therefore do not require any surface coating cover. This practicality and low surface preparation is one of the main advantages of the usage of TSA for composite materials [8].

7.2.2 Effect of Loading Frequency in Adiabatic Conditions

Attainment of adiabatic conditions during TSA measurements requires the application of dynamic loading at sufficient frequency so that the temperature change being measured by the camera due to the thermoelastic effect is retained in the outer surface ply.

Experiments with GFRP composites[53, 20] have showed that frequencies between 10-12 Hz are sufficient to obtain quasi-adiabatic conditions during TSA measurements. However, the case is different for CFRP composite materials due to the high conductivity of this material compared to GFRP composite materials (almost three times higher[70]). Consequently, for determining the suitable frequency for valid TSA measurements, a UD(0) sample with 2.23 mm thickness was cut and tabbed with GFRP tabs. Frequency values of 5, 8, 10, 12, 15, 18, 20 Hz were tested in load control with the applied load threshold for this stacking sequence, according to table 7.2.

Application of increasingly high frequencies, particularly after 12 Hz, led to additional concerns re-

garding the stability of the tripod. Temperature changes due to the thermoelastic effect have very small orders of magnitude (between 10^{-2} and 10^{-3} K) and therefore, the occurrence of vibrations during measurements have a augmented impact. Addressing this issue, a foam was placed between the foot of the tripod and the floor and TSA measurements, with and without the foam, were conducted and the Phase output analysed. It should be noted that 0° phase should be attained for adiabatic conditions to be present in the measurements.

Comparison between the phase data collected for both TSA measurements, as illustrated in figure 7.3, concludes that the foams attenuate the vibrations that were preventing the camera to read quasi-adiabatic conditions.

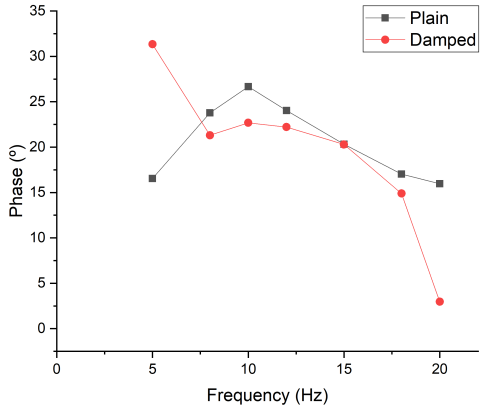

Figure 7.3: Phase difference between damped and undamped system

Results presented in figure 7.4 are in line with the ones found in early TSA works for CFRP samples[47, 49, 50]. According to these authors, the CFRP's frequency response, is more complex than for isotropic materials like Aluminium alloys[49] and GFRPs[53], for which the average temperature ratio, $\Delta T/T_0$ stabilizes after 5 Hz and 10 Hz, respectively.

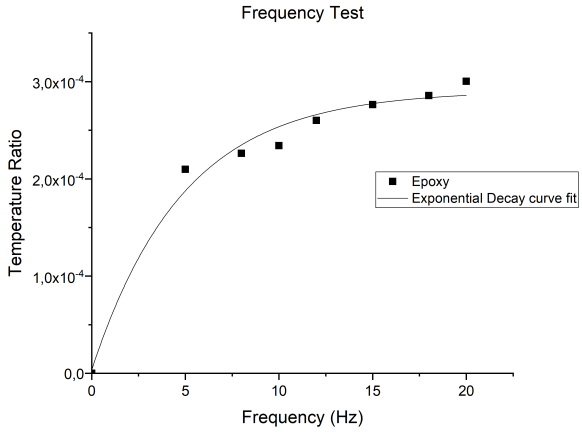

Figure 7.4: Temperature ratio values as a function of the loading frequency of CFRP sample

Although no apparent stabilization of the average temperature ratio occurs in figure 7.4, further frequency increase would lead to enhancement of the vibrations in the camera's tripod and compromise the readings. Therefore, TSA measurements were performed at a loading rate of 20 Hz, representative of the maximum attained adiabatic conditions.

Nonetheless, the frequency response from Carbon laminates is dependent of the stacking sequence. Therefore, while 20 Hz is an appropriate frequency for UD laminates, for laminate's with multi directional laminae[48] or cross ply laminates[50] that is not the case. This effect was verified in the current work by analysing phase shift value, for each sample. Nonetheless, the frequency for these stacking sequences were kept at 20 Hz since, frequencies higher than this value generated vibrations in the camera which the foam was unable to resolve.

7.2.3 Effect of Speckle Pattern in Temperature Amplification

The combination of both TSA and DIC in practical real-time applications requires the IR camera to measure the temperature emission from a structure whose surface is painted with a speckle pattern. However, the DIC is measuring the strain occurring in the laminate's epoxy surface layer. Therefore, to improve the comparison between the two techniques, the average signal amplification, due to the effect of the paint layer, should be quantified. Influence of the application of black paint coatings, to induce high uniform emissivity surfaces in metallic samples, was reported by Welch et al.[71]. In this work, the experimental results for frequencies between 20 and 25 Hz provided a clear temperature amplification of 20 %, from painted to unpainted samples. After a series of tests where combination of coating thickness and test frequency was done, the authors concluded that a strain witness behaviour was only obtained for the paint layer for a combination of high thickness and frequency, whereas for lower frequencies and thickness the paint layer acts as a temperature amplifier.

Results obtained by Wang et al.[29] for the evaluation of IR signal differences for samples with and without speckle pattern, allowed the authors to conclude that this layer does not alter the temperature emission value, in relation to the epoxy layer, reassuring the accuracy of the obtained results.

In order to simulate as accurately as possible the joint usage of TSA and DIC, a unidirectional sample, with fibers along the longitudinal direction, was dynamically tested under load control on an Instron 8801 servo-hydraulic machine, between 2 and 8 kN, at a frequency of 20 Hz. The thermal camera was positioned at the previously mentioned distance of the sample and images were acquired at a frame rate of 350 Hz. Afterwards, maintaining the same conditions (load, orientation, camera position and recording parameters), the sample was painted with a speckle pattern and tested, after changing the emissivity parameter, in the software to the corresponding value.

Optical microscope image of the speckle pattern can be observed in figure 7.5, where paint bubbles of different dimensions are visible. An average temperature amplification of 1.03 was verified which was

incorporated in the data processing in section 7.5.

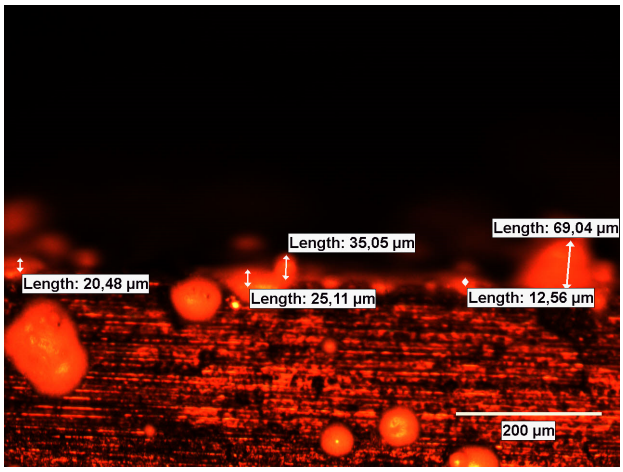

Figure 7.5: Optical Microscopy Image of the Speckle Pattern

The DIC measurements were taken in relation to the laminate's surface, i.e the Epoxy surface layer. In order to obtain a more accurate correspondence, between the results from both techniques, the temperature amplification was incorporated in the processing of the results so that the real value of the Epoxy's temperature signal was accounted.

7.3 Experimental Procedure

7.3.1 Digital Image Correlation

Positioning of the DIC system was straightforward since no concerns regarding vibrations were taken due to the quasi-static load application. Therefore, the system was positioned on a metallic stand, next to an Instron 8853 servo-hydraulic machine with a load cell of $\pm$ 250 kN. The sample was loaded under a tensile test with a load rate of 3 kN/min and DIC measurements were performed by positioning the system at a measuring distance of 1250 mm, with the sensor's axis perpendicular to the sample's surface. Image acquisition was obtained for a frame rate of 0.5Hz, since larger frame rate values required a lower lens amplitude which decrease the light on the sample, resulting in incorrect subset matching. Measurements were performed between the same loading limits as the aforementioned dynamic test (according to table 7.2), in order to provide accurate correlation between mechanical deformation of the sample in both tests.

Stacking Sequence	P_{min} [kN]	P_{max} [kN]
$[0]_8$	2	11.25
$[0/90_2/0]_s$	2	7.65
$[90/0_2/90]_s$	1	4.49
$[0_2/-45_2/45_2/90_2]_s$	2	11.61

Table 7.2: Load threshold

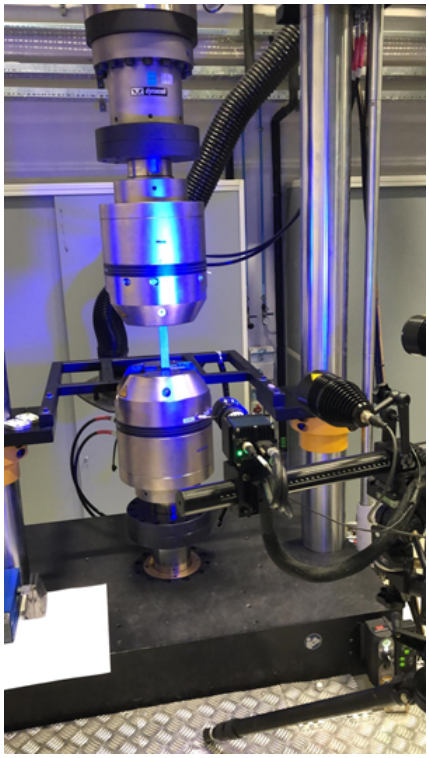

Figure 7.6: DIC experimental setup

7.3.2 Thermoelastic Stress Analysis

The FLIR infrared camera model, described in section4.3.1, with a 25 mm lens and placed at a distance of 73 cm of the sample, was used to monitor temperature emission signal during all the TSA measurements. These conditions are not ideal since the measurement's quality is highly dependent on the number of photons arriving to the photon detector, therefore it is desirable to put the camera as close to the sample as possible. However, a compromise had to be reached due to several aspects,

- Two servo-hydraulic machines, powered by an Instron Hydraulic Power Unit, with dynamic test capabilities were available (Instron 8803 and Instron 8853). The Instron 8853 allowed the position of the camera to be very close to the sample, however the vibrations induced by this machine, for the expected loading frequencies, made the camera measurements susceptible to considerable errors;

- The Instron 8803 had a AVE2 Video Extensometer incorporated requiring the grips to be rotated and also due to the presence of a plastic protective door, attached to the front of the machine, required the IR camera to be positioned at the back of the machine;

- The final location (figure 7.7) of the IR camera's tripod had to take into account the presence of several hydraulic cables which during testing would vibrate and induce errors if in contact with the tripod' legs;

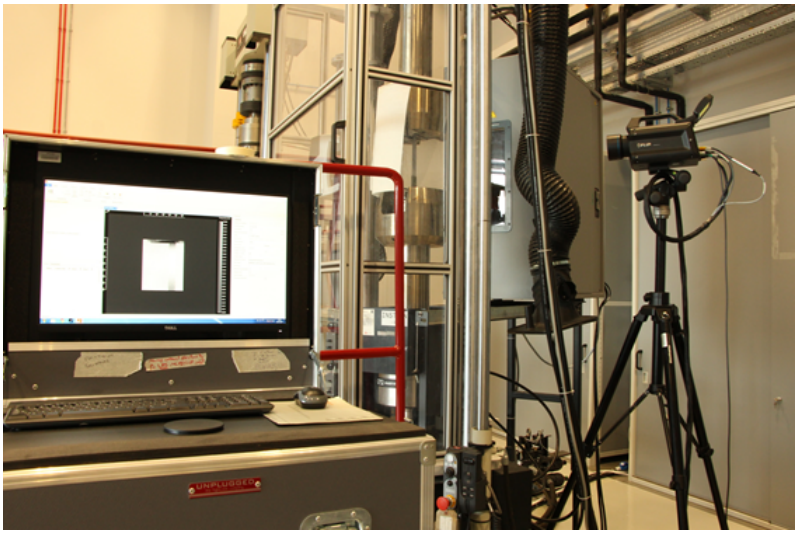

Figure 7.7: Thermoelastic Stress Analysis Setup

Furthermore, the camera was consistently positioned with a tilted angle to avoid the Narcissus effect. This corresponds to measurements of the camera's lens reflected on the sample. Illustration of this effectin figure B.1, in annex B.

Camera's acquisition parameters were set by analysis of the camera's temperature-frame rate, represented in figure 7.8 for the 25 mm lens. Therefore, the integration time of all TSA measurements was set to 0.0019 s since it is correspondent to 25°C. Consequently, the chosen value for the frame rate corresponds to the maximum allowed for the resolution at which the measurements were done was 350 Hz.

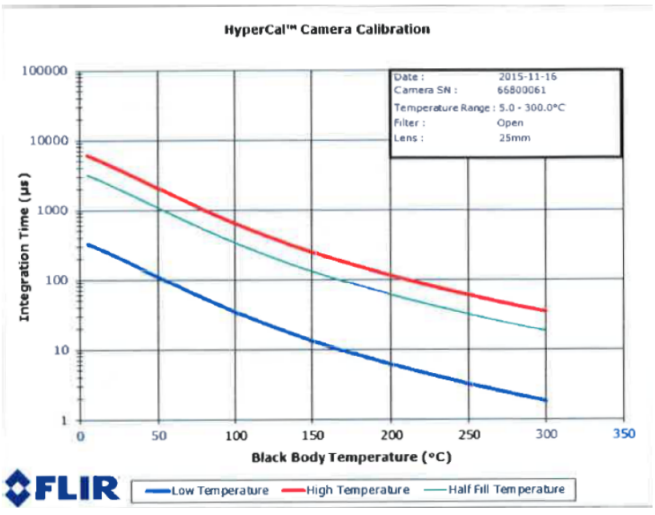

Figure 7.8: FLIR X6580sc model range of temperature measurement according to the integration time

Recovering the results obtained in the yield point determination, in section 6.2.2, the values for the maximum value of the tests were defined as 15% of the Yield Point. This was such to ensure that, during

measurements, the material would remain in the elastic domain. Moreover, a tensile-tensile dynamic test should be performed for TSA measurements which advocates the value of 0 kN for the minimum load value. However, due to load application uncertainty of the servo-hydraulic machines, this value might lead to compression of the sample, for which the value of 2 kN was set for minimum loads value. This way, no compression of the sample would occur. Summary of the load limits for each stacking sequence is presented in table 7.2.

Using load control tests, instead of displacement control, required the PID controller of the servo-hydraulic machines to be adjusted for each sample. For this process, the load applied to the sample was increased to 5kN and a cyclic load of 1 kN amplitude was applied at 12 Hz. This process allowed the machine to adjust its PID controller to the stiffness of the sample and accurately apply load.

7.4 Data Extraction and Processing

The temperature ratio ($\Delta T/T_0$) resultant from the combination of a thermal signal captured by the infrared detector together with a reference sinusoidal change in deformation provided by the servo-hydraulic machine's load cell was computed via digital processing tools available in **DisplayImg 6** software. The results from TSA tests were classified as experimental when further considering error calculations. Analogously, the **ARAMIS**^{TM}software allowed a full-field computation of the strain components ($\Delta\epsilon_x$ and $\Delta\epsilon_y$). In order to avoid the presence of edge-induced interlaminar stresses in forthcoming data processing stages [50], the ROIs for data extraction were defined such that gap distances to the sample's edges and griping area were considered. The user interfaces of **DisplayImg 6** and **ARAMIS**^{TM}softwares, for tests using the UD0 sample, are presented in figures 7.9 and 7.10, respectively.

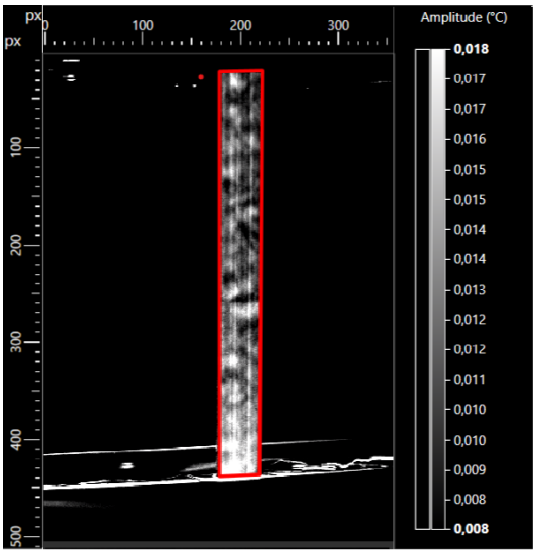

Figure 7.9: **DisplayImg 6** interface of UD0 TSA test

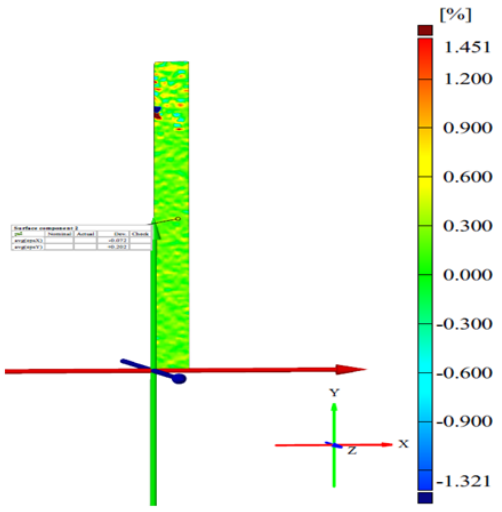

Figure 7.10: **ARAMIS** interface of UD0 DIC test

Output data is stored in a pixel-wise manner. However, depending upon cameras' resolutions, the same geometrical location of a material point in the specimen can be represented by two distinct sets of pixels. Therefore, data comparison is only made possible if one interpolates both final datasets into a common mesh with a reduced number of structured grid points, here defined as *background mesh*.

If one considers a set of initial data points $h(\mathbf{x})$ with coordinates $\mathbf{x}$ in a bi-dimensional space defined as the *input space*, their mapping into a set of new reference points ξ located in the background mesh can be accomplished using radial basis functions (RBF), schematically shown in figure 7.11. The process relies in a first non-linear mapping from $\mathbf{x}$ into ξ through a function ϕ that takes the distance between the training and reference points as input, $\|x_1 - \xi_M\|$. A final collocation in the background space using a linear combination of the training points is followed. In summary, the function value at point $\mathbf{x}$ represented in the background domain, $f(\mathbf{x})$, can be expressed as [72]:

$$f(\mathbf{x}) = \sum_{i=1}^{M} w_i \phi(r_i) = \sum_{i=1}^{M} w_i \phi(\|\mathbf{x} - \xi_i\|) \tag{7.1}$$

where w_i are unknown scalar weights and ϕ is denoted as a Kernel function.

A first step involves defining the set of constants $\mathbf{w} = \{w_1, w_2, ...w_M\}$ for M reference points from N initial training points. By rewriting equation 7.1 in a matrix format,

$$\begin{bmatrix} \phi(\|x_1 - \xi_1\|) & ... & \phi(\|x_1 - \xi_M\|) \\ ... & ... & ... \\ \phi(\|x_N - \xi_1\|) & ... & \phi(\|x_N - \xi_M\|) \end{bmatrix} \begin{pmatrix} w_1 \\ ... \\ w_M \end{pmatrix} = \begin{pmatrix} h(x_1) \\ ... \\ h(x_M) \end{pmatrix} \tag{7.2}$$

one can simply determine $\mathbf{w}$ by solving $\mathbf{A}^{-1}\mathbf{h}$, where $\mathbf{A} = \phi_{ij}(\mathbf{e}_i \otimes \mathbf{e}_j)$ for $i = 1, ..., N$ and $j = 1, ..., M$. Once the coefficients are determined, equation 7.1 can be used to determine the function values at position $\mathbf{x} = \xi$ in the new background domain.

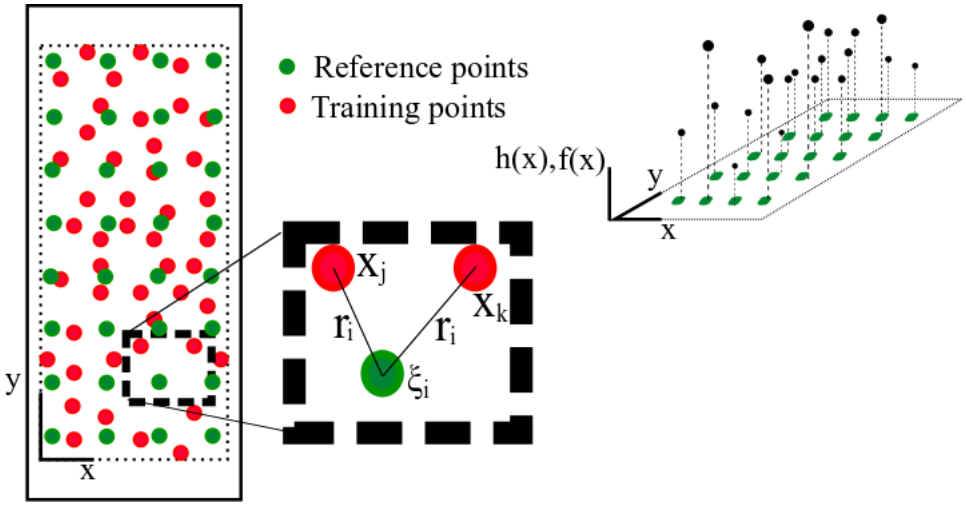

Figure 7.11: Radial Basis Function interpolation schematic

A Gaussian Kernel function was used to interpolate the training points into the background mesh domain.

$$\phi(\|\mathbf{x} - \xi_i\|) = \exp(-\|\mathbf{x} - \xi_i\|^2) \tag{7.3}$$

where $\mathbf{x}$ can either correspond to the input mesh from the DIC or TSA. Other interpolation functions, such as rational functions, were tested for which the results did not change significantly.

A mesh refinement study was performed for all the laminate's stacking sequences. A distance between mesh points of 1mm was selected since it provides stabilized data values with a reasonable computational times. Summary of the results are presented in tables B.2, B.3, B.4 and B.5, in section B.2.

After interpolating the DIC's point-wise strain values into the background mesh, scalar temperature ratios were computed using the various thermoelastic model's equations. The mechanical and thermal properties determined in section 6 were used in these equations and are summarised in table 7.3.

Property	CFRP lamina	OM 10 Epoxy
E_1 [GPa]	128.382	-
E_2 [GPa]	8.284	-
ν_{12}	0.3	-
ν_{21}	0.019	
ρ [kg/m^3]	1516.3	-
C_p [J/kg.K]	763.632	-
α_1 [μ .K^{-1}]	0.55	-
α_2 [μ .K^{-1}]	27.4	-
E_r[GPa]	-	3.583
ν_r	-	0.39
C_{pr} [J/kg.K]	-	841
ρ_r [kg/m^3]	-	1210
α_r [μ .K^{-1}]	-	58

Table 7.3: Mechanical and Thermal Properties of Epoxy resin and CFRP lamina

Figure 7.12 illustrates the aforementioned data extraction and interpolation methodology.

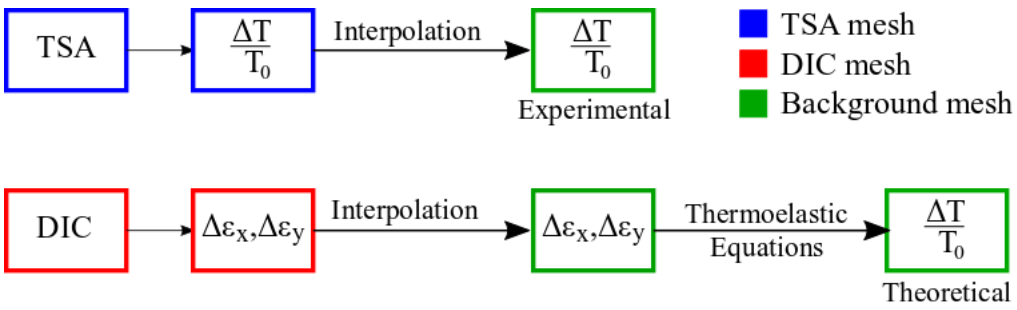

Figure 7.12: Data extraction and interpolation methodology

7.5 Results and Discussion

After obtaining the full-field temperature ratio values, from each model, the temperature ratio obtained through TSA measurements were compared against the theoretical values according to equation 7.4.

$$e(\%) = \frac{|(\Delta T/T_0)_{DIC} - (\Delta T/T_0)_{TSA}|}{(\Delta T/T_0)_{DIC}} \times 100 \tag{7.4}$$

The model with the least error is considered to best characterize the local thermoelastic behaviour.

Results of this method allowed mapping the thermoelastic model characterizing the thermoelastic behaviour of each point of the sample and the respective minimum error obtained through equation 7.4. This local-based assignment is represented in figures 7.13 and 7.14.

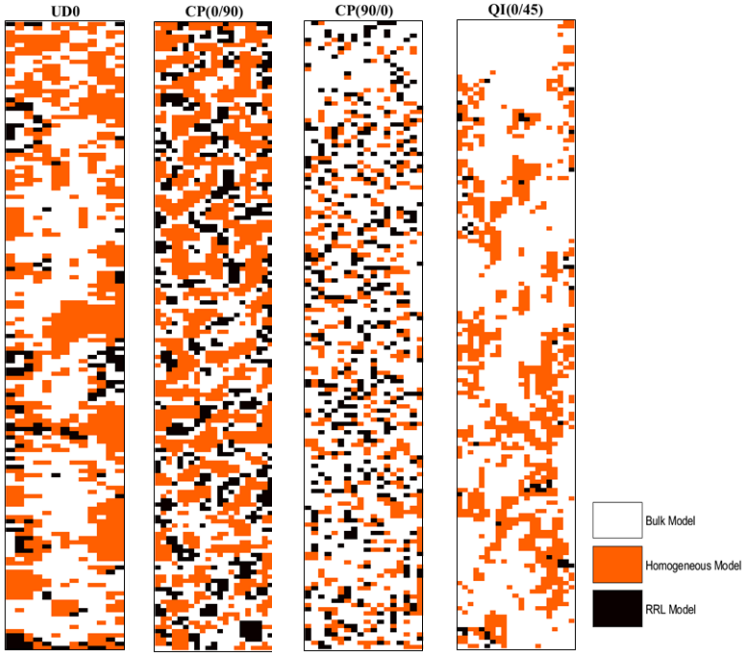

Figure 7.13: Point-wise thermoelastic model assignment which yields the least error

Analysis of figure 7.13 confirms the limitations of the global calibration of the thermoelastic signal, since several locations of the sample have different models assigned. The results of the different will differ from the ones obtained by using the strain gauge's data as input. Furthermore, one of the already referred consequences of the conventional methodology for quantitative TSA measurements is the under/overestimation of the material's mechanical deformation. In order to prove this statement, table 7.4 was generated containing the average minimum error for the correlation between both techniques and the theoretical temperature amplitude values, which are directly correlated with the values of the strain.

For the UD0 sample, the distribution of the thermoelastic models reveals a predominance of the bulk model, covering around 53.90% of the sample's area. Accuracy of the results are reinforced by the averaged phase angle of 5.1976º during TSA measurements, meaning adiabatic conditions appear to

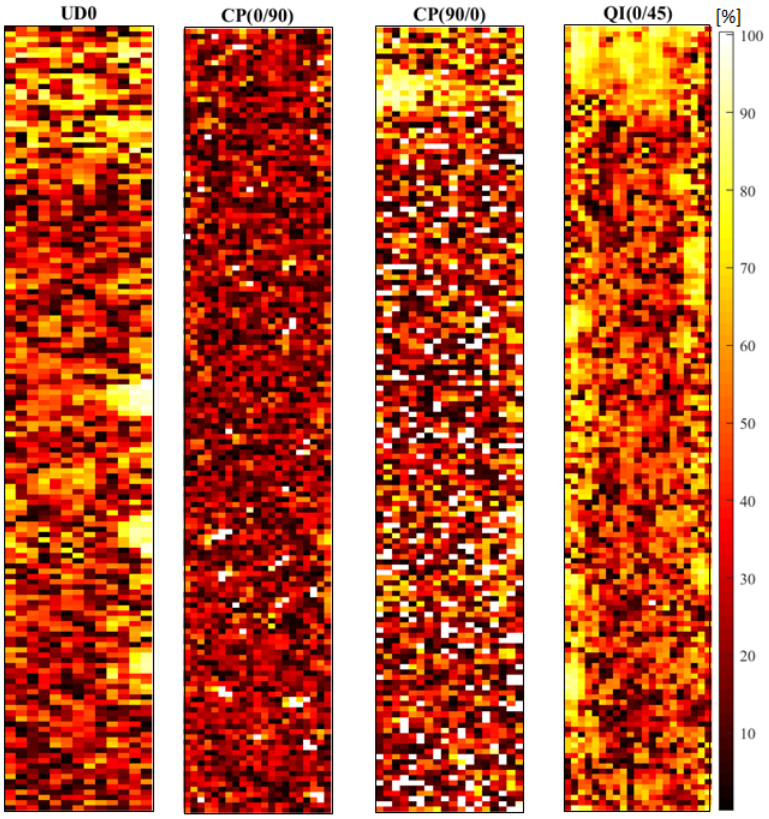

Figure 7.14: Mapping with the minimum local error

have been attained. Nonetheless, 39.24% of the sample's area has a thermoelastic response closer to the homogeneous model. Similar TSA works with low loading frequencies[73] have concluded that the homogeneous model better represents the thermoelastic behaviour due to the influence of inner plies in the surface's thermal response. However, in the authors perspective, since the homogeneous model's mathematical formulation relies in the assumption of isentropic deformation processes, this argument seems not to be valid. Finally, only 6.87% of the sample's area has a thermoelastic response closer to the resin-rich layer model, which is in agreement with the conclusions arrived by Pitarresi and Galietti[23].

Although the temperature signal from the resin is reduced, an increase of 3.13% was observed between the average experimental temperature ratio obtained through the bulk model. On the other hand, if the homogeneous model would have been used to characterize the global thermoelastic behaviour of the material, an average increase of 8.74% would have occurred. A justification for no apparent temperature ratio difference between models might lay in the low order of magnitude of the applied load. An increase in the maximum load of the test could enhance this difference. Another factor that could justify the reduced differences between the two models is the quality of the laminate and the lack of defects in the material, which leads to a higher homogenization of the material.

Attending on the CP laminates, there are considerable locations for which the homogeneous model

seems to provide lower correlation errors. Considering the theoretical background behind this model, the thermoelastic response reflects a high influence of the laminate's properties. This fact has been pointed out in cross ply laminates due to the high mismatch in thermo-mechanical properties between 0° and 90° plies. This translates in the generation of opposing magnitude stress fields, thus increasing the through thickness stress gradient and preventing retention of the heat generated due to the thermoelastic effect in the surface ply. This assumption is reinforced by increase of the average phase angle. For the CP(0/90) and CP(90/0) samples, phase angles of 15° and 23° were respectively attained.

For the QI(0/45) sample, the increase in the number of plies, in relation to other configurations (from 8 to 16 layers), appears to have led to an homogenization of the material's thermoelastic response, since only the bulk and homogeneous models present a considerable area percentage, 70.89 % and 27.55%, respectively. This could be resultant from stacking two plies with the same orientation near the surface observed by the IR detector, thus reducing any mismatch between properties of different orientation plies. An average 7.39% increase on the temperature ratio is obtained between the areas characterized by the homogeneous and the bulk model. The RRL model, accounting for only 1.56% of the whole area, gives a thermoelastic response 2.66% lower than the bulk model.

Even though this work appears to provide a better approach for evaluating the material's stress state, inspection of table 7.4 reveals a high percentage for the average minimum error for every stacking sequence. Several possible sources of error can be pointed out:

- The measuring distance between the IR camera and the specimen together with the lens magnification employed in the camera makes any small vibrations in system to be amplified in the detector's signal;
- The servo-hydraulic machine's load cell is 2 orders of magnitude higher than the applied load. This fact compromises the capability of the controller to reach the load limits in a consistent manner throughout the test, particularly at high loading frequencies;
- High loading frequencies induce vibrations in the camera which will amplify errors in the measurements;
- Correlation between the two techniques was done between different load stages;
- The small changes in temperature due to the thermoelastic effect, around 10^1 mK, make the accuracy of the results highly sensitive to small disturbances during the TSA measurements.

		Temperature Ratio ($\mu K/K$)		
Laminate Code	Average Error (%)	RRL	Homogeneous	Bulk
UD0	31.8011	94.933	86.64	92.053
CP(0/90)	28.1484	202.81	197.29	205.69
CP(90/0)	60.2925	209.66	210.29	210.37
QI(0/45)	41.7037	29.431	32.468	30.235

Table 7.4: Laminate's average error and temperature ratio from each thermoelastic model

Assuming the influence of experimental errors in the TSA and DIC's output does not compromise the accuracy of the calibration process, another hypothesis should be drawn to explain the source of the inaccuracy of the previous results.

7.5.1 Effect of the Coefficient of Thermal Expansion

The following proposal has been previously referred by Pitarresi and Galietti[23]. Many engineering materials have a positive coefficient of thermal expansion, α. Therefore, an extension, in a certain direction, occurs once temperature increases. In the case of carbon fibers, this value is negative at room temperature, i.e α_1 = -0.38μm/m$^{\circ}$C [74]. On the other hand, the epoxy resin has a positive CTE value for room temperature. This mismatch between the fiber and matrix's CTE generates a material whose CTE is highly sensitive to fiber/matrix volume ratios. Yales et al.[75] proved this effect by evaluating the change of the laminate's α_1 due to an increase of 10% in the fiber volume, from 50% to 60%. This change induced a switch in the laminate's CTE value from positive to negative, at room temperature. Further developments revealed the oscillatory behaviour for the CTE value, with increasing temperatures. The effect of the CTE's variability in the thermoelastic signal was also pointed out by Zhang et al.[54] when comparing the thermoelastic response, in CFRPs, over and between fiber bundles since it indicated fiber and resin rich locations, respectively. For these locations, the SPATE's signal reported rapid changes between positive and negative SPATE signal values, respectively.

Therefore, switching from a global coefficient of thermal expansion for the outer lamina, to a local value, which takes into account fiber/matrix volume ratio fluctuations will give a more accurate result for the material's thermoelastic behaviour.

7.5.2 Implementation

For increasing the sample data of the newly develop approach, more values for CTE in the longitudinal direction were obtained through TMA tests, according to ASTM E831 standard. This will aid the identification of the CTE values that should be included in the range.

The local-based thermoelastic assignment and correspondent error, obtained by ranging α_1 values from the minimum and maximum, obtained through TMA tests and summarised in table B.6, are illustrated in figures 7.15 and 7.16.

Comparison between the local distribution of the thermoelastic models, figures 7.13 and 7.15, clearly show the replacement of the homogeneous model with the bulk model. This way, locations which appear to have a thermoelastic response with high influence from the laminate, instead were not taking into account fiber/ratio volume ratio variations. This effect is particularly significant in the unidirectional sample, where the percentage of locations under the homogeneous model decreased from 39.18% to 0.938%. The results for the cross ply with the surface ply oriented at 90° are consistent with the literature

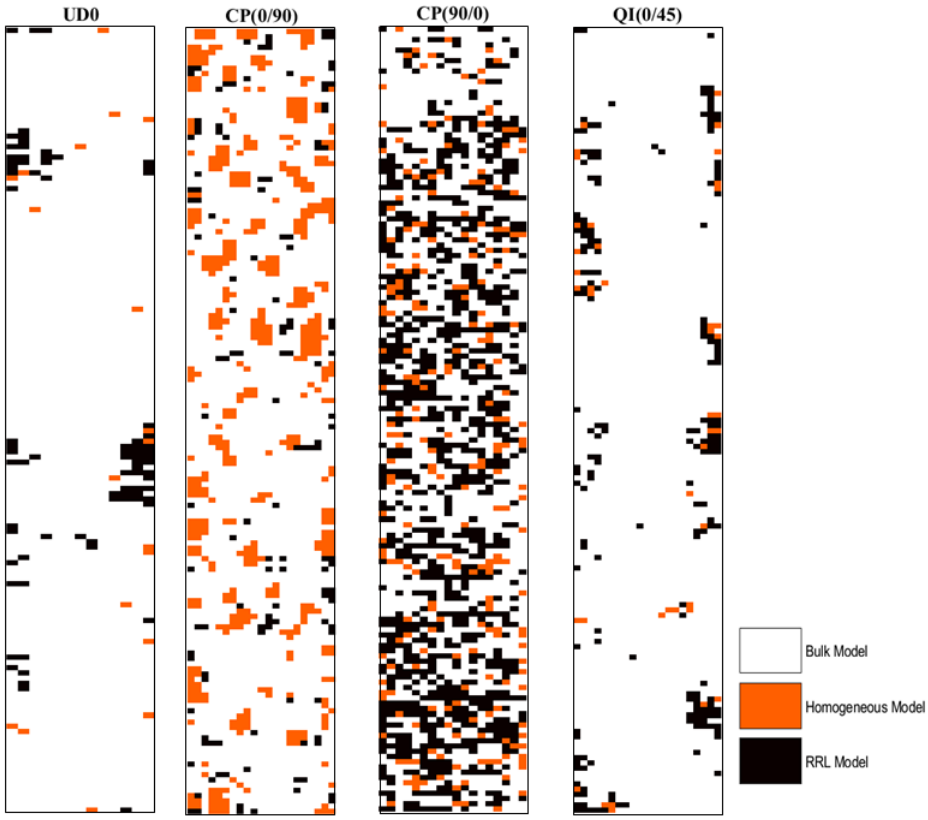

Figure 7.15: Local thermoelastic model calibration with local CTE distribution

review[52], since for this laminate there is an increase on the thermoelastic response from the surface layer. Percentage of the resin rich layer model increased from 4.35% to 35.94%, with the change in the surface ply orientation.

Evaluating the average error reduction between each sample reveals that the laminate, whose error reduction occurred in a lower percentage was the Cross Ply sample with surface ply at $90°$. While in the sample with a surface layer at $0°$ the error decrease was 72.33%, in the CP(90/0) sample the error decreased 58.03%. This fact, in addition to the presence of locations with high error in the middle of the sample, leads to the conclusion that non-adiabatic effects might have been present in the sample, during loading. This could have been originated in cracks, voids or heat generation due to friction of the plies. Nonetheless, the possibility that some overload might have occurred in the sample cannot be dismissed. The same consideration should apply to the CP(0/90) sample due to the existence of a high number of points, within the laminate, which present high error value.

Reduction of, 82.05% and 83.75% of the average minimum error were obtained, respectively, for the UD0 and QI(0/45) samples. The high error decrease in the unidirectional and quasi-isotropic sample yields a particular significance due to the high application of these laminates in aerospace structures.

In addition, the histogram containing the errors before and after local CTE distribution, is presented for each stacking sequence in section B.4.

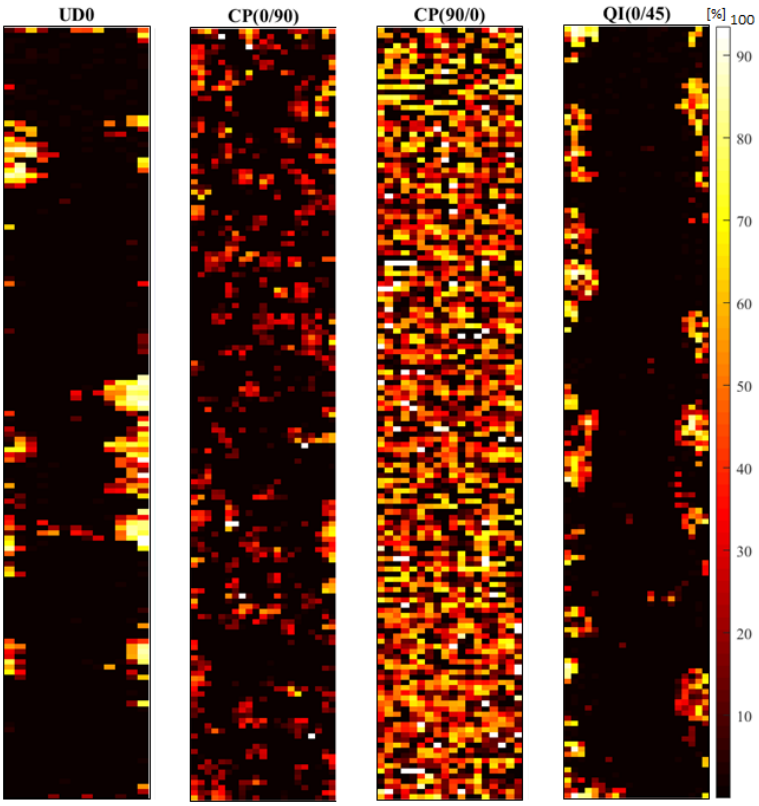

Figure 7.16: Minimum Error with local CTE distribution

		Temperature Ratio ($\mu K/K$)		
Laminate Code	Average Error (%)	RRL	Homogeneous	Bulk
UD0	5.7098	81.902	85.065	90.532
CP(0/90)	7.7893	203.92	196.84	202.58
CP(90/0)	34.99	210.06	210.06	210.76
QI(0/45)	6.7745	24.204	27.653	31.298

Table 7.5: Laminate's average error and temperature ratio from each thermoelastic model with local CTE distribution

The aforementioned evaluation of the results obtained through a local CTE distribution might not fully provide an accurate assessment of the errors, given that the real value for the CTE in each point is unknown. Therefore, the true validation of this last proposal can only be confirmed by evaluating the true point-wise CTE value, in the sample.

Complementing this approach, the values of other variables, namely E_1, could also present some variation, since only the average value was used from the values obtained through the various tests, as illustrated in table B.1. The variability of α_x and α_y can also be confirmed by the value difference obtained in the TMA analysis for the CP(0/90) and CP(90/0), since these two values should be equal, given the laminate's configuration. However, increasing the variability and combinations of parameters in the simulation will harshly increase the computational cost of such method.

Chapter 8

Conclusion

In this work, a new methodology was developed for quantitative measurements of the thermoelastic effect which takes into account the full-field characteristics of the already existent technique. This was accomplished by employing DIC for strain measurements, which takes into account the heterogeneity of composite materials.

The local calibration of the thermoelastic signal was obtained by generating a full-field map with the thermoelastic model which better fits the temperature generation captured with the IR camera. Analogously to previous TSA works in CFRPs, the role of the resin-rich layer as a strain witness of the composite material due to its low-conductive properties, was negligible when compared with the response of the surface ply. The CFRP's CTE variability and its impact in the prediction for temperature generation due to cyclic load was assumed to justify this fact. Nonetheless, locations correspondent to the resin-rich layer model verified higher temperature emission values than the remaining models.

Considerable locations of the sample still had a correspondent error which was higher than anticipated. Therefore, a new methodology was considered which takes into account the variability of the CTE of CFRPs. Several values for the laminate's CTE were obtained from different locations of the material. By ranging this value between the minimum and maximum of the determined CTE, the minimum error was obtained with the correspondent thermoelastic model.

Requirement for calculation of the CTE distribution within the laminate and elevated errors still retain this methodology as a research subject due to the elevated risks its direct application implies in the aerospace industry.

8.1 Future Work

Replication for GFRP

As mentioned throughout this work, GFRP have been widely used for TSA measurements since it provides accurate results due to agreement between the thermal properties of fiber and matrix. The influence of the resin rich layer model has been mentioned has the main source of the thermoelastic effect for this work, nonetheless this would still be a useful tool for more accurate stress field measurement.

Reproducibility for more stacking sequences

Improvement of the reliability of the method requires repeating this process for different stacking sequences.

Assessment of local CTE value

Development of techniques capable of point-wise NDI of the material's CTE will improve the reliability of the proposed methodology.

Validation in aerospace structures

This work aims to provide real-time applications to the aerospace structures industry, replacing current regulatory techniques due to the previously discussed disadvantages. Therefore, validation of this method would require its employment in the detection of the thermoelastic effect in complex shape aerospace structures.

Bibliography

[1] C. Kassapoglou. *Design and Analysis of Composite Structures With Application to Aerospace Structures*. Wiley, 2013.

[2] J. Pora. Composite materials in the airbus a380-from history to future. In *13th International Conference on Composite Materials*, 2001.

[3] K. Ramesh. Structural health monitoring – its association and use. In *New Trends in Structural Health Monitoring*, pages 1–79. Springer, Boston, MA, 2013.

[4] M. M. Derriso, C. D. McCurry, and C. M. Schubert Kabban. 2 - a novel approach for implementing structural health monitoring systems for aerospace structures. In *Structural Health Monitoring (SHM) in Aerospace Structures*. Woodhead Publishing, 2016.

[5] C. R. Farrar and K. Worden. An introduction to structural health monitoring. *Philosophical Transactions of the Royal Society A: Mathematical, Physical and Engineering Sciences*, 365(1851):303–315, 2007.

[6] R.J. Pryputniewicz. Holography. In *Springer Handbook of Experimental Solid Mechanics*, pages 675–700. Springer, Boston, MA, 2008.

[7] K. Ramesh. Photoelasticity. In *Springer Handbook of Experimental Solid Mechanics*, pages 701–742. Springer, Boston, MA, 2008.

[8] R. Greene, E. Patterson, and R. Rowlands. Thermoelastic stress analysis. In *Springer Handbook of Experimental Solid Mechanics*. Springer, 2008.

[9] M. A. Sutton. Digital image correlation for shape and deformation measurements. In *Springer Handbook of Experimental Solid Mechanics*, pages 565–600. Springer, Boston, MA, 2008.

[10] M. A. Sutton, S. R. McNeill, J. D. Helm, and Y. J. Chao. Advances in two-dimensional and three-dimensional computer vision. In *Photomechanics*, pages 323–372. Springer, 2000.

[11] B. Pan, K. Quian, H. Xie, and A. Asundi. Two-dimensional digital image correlation for in-plane displacement and strain measurement: a review. *Measurement Science and Technology*, 20(6), 2009.

[12] L.P. Canal, C. González, J.M. Molina-Aldareguía, J. Segurado, and J. LLorca. Application of digital image correlation at the microscale in fiber-reinforced composites. *Composites Part A: Applied Science and Manufacturing*, 43(10):1630 – 1638, 2012.

[13] A. Muc, M. Barski, M. Chwał, P. Romanowicz, and A. Stawiarski. Fatigue damage growth monitoring for composite structures with holes. *Composite Structures*, 189:117 – 126, 2018.

[14] M.A. Caminero, M. Lopez-Pedrosa, C. Pinna, and C. Soutis. Damage monitoring and analysis of composite laminates with an open hole and adhesively bonded repairs using digital image correlation. *Composites Part B: Engineering*, 53:76 – 91, 2013.

[15] GOM. Liebherr-aerospace: Optical metrology from gom accelerates certification tests for new landing gears. Technical report, GOM, 2015.

[16] GOM. Optical 3d metrology supports certification of airbus a350. Technical report, GOM, 2014.

[17] P. Stanley. Beginnings and early development of thermoelastic stress analysis. *Strain*, 44(4):285–297, 2008.

[18] J. R. Lesniak and B.R. Boyce. A high-speed differential thermographic camera. *SEM Spring Conference Proceedings*, (1):6–8, 1994.

[19] W. Thomson. Ii.- on the thermoelastic, thermomagnetic, and pyroelectric properties of matter. *The London, Edinburgh, and Dublin Philosophical Magazine and Journal of Science*, 5(28):4–27, 1878.

[20] R. Marques, M. Unel, M. Yildiz, and A. Suleman. Remaining useful life prediction of laminated composite materials using thermoelastic stress analysis. *Composite Structures*, 210:381 – 390, 2019.

[21] L. Krstulovic-Opara, B. Klarin, P. Neves, and Z. Domazet. Thermal imaging and thermoelastic stress analysis of impact damage of composite materials. *Engineering Failure Analysis*, 18(2):713 – 719, 2011.

[22] T. R. Emery and J. M. Dulieu-Barton. Thermoelastic stress analysis of damage mechanisms in composite materials. *Composites Part A: Applied Science and Manufacturing*, 41(12):1729 – 1742, 2010.

[23] G. Pitarresi and U. Galietti. A quantitative analysis of the thermoelastic effect in cfrp composite materials. *Strain*, 46(5):446–459, 2010.

[24] N. Rajic and S. Galea. Thermoelastic stress analysis and structural health monitoring: An emerging nexus. *Structural Health Monitoring*, 14(1):57–72, 2015.

[25] R. K. Fruehmann, J. M. Dulieu-Barton, S. Quinn, J. Peton-Walter, and P. A. N. Mousty. The application of thermoelastic stress analysis to full-scale aerospace structures. *Journal of Physics: Conference Series*, 382:12–58, 2012.

[26] R. Tomlinson and G. Calvert. Industrial applications of thermoelastic stress analysis. 1-2:165–170, 01 2004.

[27] G. Crammond, S. W. Boyd, and J. M. Dulieu-Barton. A point-wise approach to the analysis of complex composite structures using digital image correlation and thermoelastic stress analysis. *Strain*, 51(4):311–323, 2015.

[28] M. L. Silva and G. Ravichandran. Combined thermoelastic stress analysis and digital image correlation with a single infrared camera. *Journal of Strain Analysis for Engineering Design*, 46(8):783–793, 2011.

[29] R. K. Fruehmann W. Wang and J. M. Dulieu-Barton. Application of digital image correlation to address complex motions in thermoelastic stress analysis.

[30] Department of Defense of USA. Volume 3. polymer matrix composite materials usage, design and analysis. In *Composite Materials Handbook*. 2002.

[31] S.J. Park and K.M. Bae. Testing of carbon fibers and their composites. In *Carbon Fibers*, pages 135–178. 2015.

[32] T. J. Reinhart. Overview of composite materials. In *Handbook of Composites*, pages 21–33. Springer US, 1998.

[33] J.L. Massingill and R.S. Bauer. Epoxy resins. In C.D. Craver and C.E. Carraher, editors, *Applied Polymer Science: 21st Century*, pages 393 – 424. Pergamon, 2000.

[34] G.H. Staab. 6 - laminate analysis. In *Laminar Composites*, pages 189 – 284. Butterworth-Heinemann, second edition edition, 2015.

[35] V. V. Vasiliev and E. V. Morozov. Chapter 5 - mechanics of laminates. In *Advanced Mechanics of Composite Materials*, pages 255 – 320. 2007.

[36] I. M Daniel and O. Ishai. *Engineering mechanics of composite materials*, volume 3. Oxford university press New York, 1994.

[37] W. H. Peters and W. F. Ranson. Digital imaging techniques in experimental stress analysis. *Optical Engineering*, 21(3):427 – 431 – 5, 1982.

[38] Q. Tian and M.N. Huhns. Algorithms for subpixel registration. *Computer Vision, Graphics, and Image Processing*, 35(2):220 – 233, 1986.

[39] M. A. Sutton, C. Mingqi, W. H. Peters, Y. J. Chao, and S. R. McNeill. Application of an optimized digital correlation method to planar deformation analysis. *Image and Vision Computing*, 4(3):143 – 150, 1986.

[40] M. A. Sutton, S R. McNeill, J. Jang, and M. Babai. Effects of subpixel image restoration on digital correlation error estimates. *Optical Engineering*, 27(10):870 – 877 – 8, 1988.

[41] B. Pan, K. Qian, H. Xie, and A. Asundi. Two-dimensional digital image correlation for in-plane displacement and strain measurement: A review. *Measurement Science and Technology*, 20(6), 2009.

[42] GOM. Digital image correlation and strain computation basics. Technical report, GOM, 2016.

[43] B. Pan, A. Asundi, H. Xie, and J." Gao. Digital image correlation using iterative least squares and pointwise least squares for displacement field and strain field measurements. *Optics and Lasers in Engineering*, 47(7):865 – 874, 2009.

[44] M. R. James, W. L. Morris, B. N. Cox, and M. S. Dadkhah. Description and application of displacement measurements based on digital image processing. *ASME-AMD, Micromechanics: Experimental Techniques*, 102(89):333, 1989.

[45] *ARAMIS User Manual - Software, version 6.3*.

[46] N. Rajic and N. Street. A performance comparison between cooled and uncooled infrared detectors for thermoelastic stress analysis. *Quantitative InfraRed Thermography Journal*, 11(2):207–221, 2014.

[47] R. T. Potter and L. J. Greaves. The Application Of Thermoelastic Stress Analysis Techniques To Fibre Composites. In *Optomechanical Systems Engineering*, volume 0817, pages 134 – 146. SPIE, 1987.

[48] S. A. Dunn, D. Lombardo, and J. G. Sparrow. The Mean Stress Effect in Metallic Alloys and Composites. In *Stress and Vibration: Recent Developments in Industrial Measurement and Analysis*, volume 1084, pages 129 – 142. SPIE, 1989.

[49] A. K. Wong. A non-adiabatic thermoelastic theory for composite laminates. *Journal of Physics and Chemistry of Solids*, 52(3):483 – 494, 1991.

[50] C. E. Bakis and K. L. Reifsnider. The adiabatic thermoelastic effect in laminated fiber composites. *Journal of Composite Materials*, 25(7):809–830, 1991.

[51] S. A. Dunn. Analysis of thermal conduction effects on thermoelastic temperature measurements for composite materials. *Journal of Applied Mechanics*, 59(3):552, 2008.

[52] R. Marques. Remaining useful life prediction of laminated composite materials using thermoelastic stress analysis. Master's thesis, Instituto Superior Técnico, 2017.

[53] G. Pitarresi, M. S. Found, and E. A. Patterson. An investigation of the influence of macroscopic heterogeneity on the thermoelastic response of fibre reinforced plastics. *Composites Science and Technology*, 65(2):269 – 280, 2005.

[54] D. Zhang, N. F. Enke, and B. I. Sandor. Thermographic stress analysis of composite materials. *Experimental Mechanics*, 30(1):68–73, 1990.

[55] S. Sambasivam. *Thermoelastic stress analysis of laminated composite materials*. PhD thesis, University of Southampton, 2009.

[56] *User's manual FLIR x6580sc series*.

[57] Kordsa. Om10 technical data sheet. Technical report, Kordsa, 2018.

[58] Ronald F. Gibson. *Principles of Composite Material Mechanics*. Boca Raton: CRC Press, 2016.

[59] T. Ramesh. *Manufacturing defects in composites and their effects on performance*, pages 99–113. 12 2015.

[60] L. Liu and D.and Wu Z. Zhang, B.and Wang. Effects of cure cycles on void content and mechanical properties of composite laminates. *Composite Structures*, 73(3):303 – 309, 2006.

[61] D.O. Adams and D. F. Adams. Tabbing guide for composite test specimens. Technical report, U.S. Department of Transportation, Federal Aviation Administration, Office of Aviation Research, 2002.

[62] *ASTM D638-14, Standard Test Method for Tensile Properties of Plastics*.

[63] R. Talreja. 5 - manufacturing defects in composites and their effects on performance. In *Polymer Composites in the Aerospace Industry*, pages 99 – 113. Woodhead Publishing, 2015.

[64] *ASTM D3171-15, Standard Test Methods for Constituent Content of Composite Materials*, 2015.

[65] *ASTM D3039 / D3039M-17, Standard Test Method for Tensile Properties of Polymer Matrix Composite Materials*.

[66] *ASTM D5379 / D5379M-12, Standard Test Method for Shear Properties of Composite Materials by the V-Notched Beam Method*, 2012.

[67] *ASTM E1269 - 11, Standard Test Method for Determining Specific Heat Capacity by Differential Scanning Calorimetre*, 2018.

[68] *ASTM E831 - 19Standard Test Method for Linear Thermal Expansion of Solid Materials by Thermomechanical Analysis*.

[69] F. P. Incropera, D. P. Dewitt, T. L. Bergman, and Lavine A. S. *Fundamentals of Heat and Mass Transfer*. Wiley, 6 edition, 2006.

[70] U. Berardi and N. Dembsey. Thermal and fire characteristics of frp composites for architectural applications. *Polymers*, 7(11):2276–2289, 2015.

[71] C.S. Welch and M.J. Zickel. Thermal coating characterization using thermoelasticity. In *Review of Progress in Quantitative Nondestructive Evaluation: Volumes 12A and 12B*, pages 1923–1930. Springer US, 1993.

[72] V. Skala. A practical use of radial basis functions interpolation and approximation. 37:137–145, 01 2016.

[73] D. Crump and J. Dulieu-Barton. Performance assessment of aerospace sandwich secondary structure panels using thermoelastic stress analysis. *Plastics, Rubber and Composites*, 39:137–147, 06 2010.

[74] T700s data sheet. Technical report, TorayCA, 2018.

[75] B. Yates, M. J. Overy, J. P. Sargent, B. A. McCalla, D. M. Kingston-Lee, L. N. Phillips, and K. F. Rogers. The thermal expansion of carbon fibre-reinforced plastics. *Journal of Materials Science*, 13(2):433–440, 1978.

[76] G. Pitarresi and E. A. Patterson. A review of the general theory of thermoelastic stress analysis. 38(5):405–417, 2003.

Appendix A

Appendix chapter

A.1 Thermoelastic Stress Analysis

The full mathematical deduction of the thermoelastic effect performed in this section.

The thermoelastic phenomena corresponds to the change of temperature occurring in a material when subjected to changes in its elastic strain. Therefore, characterization of the thermoelastic phenomena involves relating the material temperature change (ΔT) to the material's stress/strain tensor ($\sigma_{ij}/\epsilon_{ij}$).

Characterization of the system, from a thermodynamic point of view, involves describing its state by means of state variables. Therefore, to investigate the thermo-mechanical behaviour of an elastic solid material, the system's state can be described by assigning the stress tensor and the temperature as state variables (assuming small displacements hypothesis).

Thus, the state function, mechanical or thermodynamical, describing the state of the system can be written as dependent of the state variables, i.e the internal energy of the system is written as

$$u = u(\sigma_{ij}, T) \tag{A.1a}$$

and in the differential form

$$du = \Big(\frac{\partial u}{\partial \sigma_{ij}}\Big)_T d\sigma_{ij} + \Big(\frac{\partial u}{\partial T}\Big)_{\sigma_{ij}} dT \tag{A.1b}$$

For a closed system undergoing a reversible process, the first law of thermodynamics states,

$$du = \delta w + \delta q \tag{A.2}$$

where all the terms are specific (per unit volume) and u is the internal energy of a system, w and q are

the work and the heat exchanged between the system and the surroundings, respectively. By reviewing the notation used in the previous equation it is assumed that the heat is positive when transferred from the surroundings to the system and the same for the work when exerted on the system. Moreover, the usage of partial (δ) and total (d) differentials, in the previous equation, relates to the path dependence/independence of the thermodynamic process.

The second law of thermodynamics can now be stated, which relates the increase of entropy (ds) in the system, to the generated heat (δq) at temperature (T). For reversible processes one obtains

$$(ds)_{reversible} = \frac{(\delta q)_{reversible}}{T} \tag{A.3}$$

In TSA, the continuous material undergoes a deformation in a quasi-static process, in order to avoid stress gradients which could damage the structure and induce residual stress (altering the TSA data analysis), once it is relaxed. This ensured that equilibrium is achieved in each step of the experiment and an almost adiabatic process can be assumed.

The external load applied on the structure constitutes the only work in the system. Therefore, one can define the work exchanged between the system represented as an infinitesimal element of unit volume and the external surroundings, at a constant temperature, as

$$\delta w = \sigma_{ij} d\epsilon_{ij} \tag{A.4}$$

where σ_{ij} is the stress tensor and ϵ_{ij} is the strain tensor at a given constant temperature. Introducing equations A.3 and A.4 into equation A.2, the following equation is obtained

$$du = Tds + \sigma_{ij} d\epsilon_{ij} \tag{A.5}$$

A second state function Gibbs free energy can now be introduced, as a thermodynamic potential, per unit volume, meaning g = g(σ_{ij}, T)

$$g = u - Ts - \sigma_{ij}\epsilon_{ij} \tag{A.6}$$

and by applying the differential properties, the differential form for the previous equation is obtained

$$dg = du - Tds - sdT - \sigma_{ij} d\epsilon_{ij} - \epsilon_{ij} d\sigma_{ij} \tag{A.7}$$

Introducing equation A.5 into the previous one, yields

$$dg = -(sdT + \epsilon_{ij} d\sigma_{ij}) \tag{A.8}$$

The aforementioned equation describes the relation between the Gibbs free energy and the state variables, for which the differential form assumes

$$dg = \Big(\frac{\partial g}{\partial \sigma_{ij}}\Big)_T d\sigma_{ij} + \Big(\frac{\partial g}{\partial T}\Big)_{\sigma_{ij}} dT \tag{A.9}$$

Comparing equations A.8 and A.9 the following equalities are valid

$$\epsilon_{ij} = -\frac{\partial g}{\partial \sigma_{ij}} \quad , \quad s = -\frac{\partial g}{\partial T} \tag{A.10}$$

Stating an equivalent relation for the entropy's dependence of the state variables, the following equation is obtained

$$ds = \Big(\frac{\partial s}{\partial \sigma_{ij}}\Big)_T d\sigma_{ij} + \Big(\frac{\partial s}{\partial T}\Big)_{\sigma_{ij}} dT \tag{A.11}$$

which can be modified taking into account the relations obtained in A.10.

$$ds = \frac{\partial}{\partial \sigma_{ij}}\Big(-\frac{\partial g}{\partial T}\Big)d\sigma_{ij} + \frac{\partial}{\partial T}\Big(-\frac{\partial g}{\partial T}\Big)dT \tag{A.12}$$

and by introducing the second result of equation A.10 in A.12, the following result is obtained,

$$-ds = \frac{\partial^2 g}{\partial T^2} dT - \frac{\partial \epsilon_{ij}}{\partial T} d\sigma_{ij} \tag{A.13}$$

If instead the formulation adopted by the authors in [76] was used ($u = u(\epsilon_{ij}, T)$) by defining the strain tensor (ϵ_{ij}) and temperature (T) as state variables, the Helmholtz potential would have been used for describing the system's state, instead of the Gibbs free energy. Nonetheless, the same results would have been achieved. However, an additional relation would be required, in order to relate the parameter γ with the Lamé constants and the coefficient of thermal expansion, α.

The specific heat at constant pressure, per unit volume, is defined as

$$\rho C_\sigma = \Big(\frac{\delta q}{dT}\Big)_{\sigma_{ij}} \tag{A.14}$$

Combining the equalities previously stated in equations A.3 and A.10 into A.14 yields,

$$\rho C_\sigma = \Big(\frac{T ds}{dT}\Big)_{\sigma_{ij}} = -T\Big(\frac{\partial^2 g}{dT^2}\Big)_{\sigma_{ij}} \Leftrightarrow \Big(\frac{\partial^2 g}{dT^2}\Big)_{\sigma_{ij}} = -\rho\frac{C_\sigma}{T} \tag{A.15}$$

Introducing this latest equality in A.13, the following relation is obtained

$$-ds = -\rho C_\sigma \frac{dT}{T} - \frac{\partial \epsilon_{ij}}{\partial T} d\sigma_{ij} \tag{A.16}$$

Combining the adiabatic and reversible process results in isentropic conditions, for which, according to the second law of thermodynamics (equation A.3), ds = 0 and assuming the definition of thermal expansion coefficient in isotropic media, the following relation is obtained

$$\alpha\delta_{ij} = \frac{\partial\epsilon_{ij}}{\partial T} \tag{A.17}$$

Reviewing the algebraic properties of the internal product in index notation, the product between δ_{ij} by $d\sigma_{ij}$ corresponds to the first stress invariant $d\sigma_{kk}$. By joining all these results one obtains

$$\rho C_\sigma \frac{dT}{T} = -\alpha d\sigma_{kk} \tag{A.18a}$$

and by integrating it between two equilibrium states (0 and f)

$$\rho C_\sigma \int_{T_0}^{T_f} \frac{dT}{T} = -\alpha \int_{\sigma kk_0}^{\sigma kk_f} d\sigma_{kk} \tag{A.18b}$$

Resulting in

$$\rho C_\sigma ln\Big(\frac{\Delta T}{T_0}\Big) = -\alpha\Delta\sigma_{kk} \tag{A.19}$$

Current IR cameras are able to detect temperature fluctuations on the order of 1 mK. Therefore, the assumption $\Delta T << T_0$ is valid, and by expanding the logarithmic function into a series of infinite power terms, yielding

$$\rho C_\sigma\Big(\frac{\Delta T}{T_0} - \frac{1}{2}\Big(\frac{\Delta T}{T_0}\Big)^2 + \frac{1}{3}\Big(\frac{\Delta T}{T_0}\Big)^3 - ...\Big) = -\alpha\Delta\sigma_{kk} \tag{A.20}$$

By neglecting the higher order terms and rearranging the previous equation, the mathematical formulation for characterizing the thermoelastic effect, valid for isotropic materials is obtained

$$\Delta T = -T_0\frac{\alpha}{\rho C_\sigma}\Delta\sigma_{kk} \qquad k = 1,2,3 \tag{A.21}$$

In the case of orthotropic materials, such as composite laminates, the coefficient of thermal expansion is no longer constant on every direction. Therefore, the first stress invariant will be further developed into the principal directions of the laminate. Therefore, the thermoelastic response is given by the linear combination of the coefficient of thermal expansion and the stress changes, in a given principle direction.

$$\Delta T = -T_0\frac{1}{\rho C_\sigma}(\alpha_1\Delta\sigma_1 + \alpha_2\Delta\sigma_2 + \alpha_3\Delta\sigma_3) \tag{A.22}$$

The term $\frac{\alpha_i}{\rho C_\sigma}$ is many times referred to called the thermoelastic constant, represented by K_i.

Under plane stress assumption, valid for composite laminates where in-plane dimensions are much

higher than the thickness. For this assumption, equation A.22 simplifies to,

$$\Delta T = -T_0 \frac{1}{\rho C_\sigma}(\alpha_1 \Delta\sigma_1 + \alpha_2 \Delta\sigma_2) \tag{A.23}$$

valid for orthotropic materials under plane stress and adiabatic, reversible conditions.

Appendix B

Appendix chapter

B.1 Tensile Test

In this section the full results obtained for the mechanical testing are described.

Unidirectional Carbon Fiber Reinforced Polymer					
Specimen	1	2	3	4	5
E_1 [GPa]	125.211	129.412	128.375	119.815	130.528
E_2 [GPa]	8.6242	8.4847	8.1254	8.0160	8.1713
ν_{12}	0.28	0.30	0.29	0.33	0.30
ν_{21}	0.019	0.020	0.018	0.022	0.019

Table B.1: Tensile test result

B.2 Mesh Refinement Study

Element Size [mm]	Average Error [%]	Computational times (s)
4	27.5412	1.676363
2	26.8674	3.805647
1	31.8011	31.8011
0.5	31.5144	356.37

Table B.2: Mesh refinement study for the UD0 sample

Element Size [mm]	Average Error [%]	Computational Time (s)
4	27.5412	3.892957
2	26.8674	9.049526
1	31.8011	81.550772
0.5	31.5144	2080.854

Table B.3: Mesh refinement study for the CP(0/90) sample

Element Size [mm]	Average Error [%]	Computational Time (s)
4	27.5412	97.5168
2	26.8674	85.6878
1	31.8011	60.2925
0.5	63.8057	3439.308

Table B.4: Mesh refinement study for the CP(90/0) sample

Element Size [mm]	Average Error [%]	Computational Time (s)
4	30.6408	6.370201
2	35.8678	15.945880
1	42.1468	150.957924
0.5	41.7037	3277.002

Table B.5: Mesh refinement study for the QI(0/45) sample

B.3 Narcisus Effect

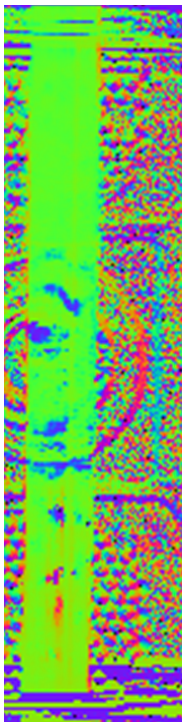

Figure B.1: Narcisus effect

B.4 CFRP minimum error histogram

α_1 (μm/(m.K))			
-0.990	-0.930	-0.710	-0.680
-0.570	-0.540	-0.190	-0.150
-0.0173	0.0273	0.0608	0.0822
0.320	0.390	0.400	0.420
0.490	0.550	0.640	0.640

Table B.6: CTE values for several regions of the CFRP laminate

Laminate Code	CTE (%)	RRL (%)	Bulk(%)
UD0	39.18	5.44	55.38
CP(0/90)	67.95	5.95	26.10
CP(90/0)	63.69	18.06	18.25
QI(0/45)	0.083	26.19	73.72

Table B.7: Pixel percentage of each thermoelastic model, prior to local CTE distribution

Laminate Code	CTE (%)	RRL (%)	Bulk(%)
UD0	19.31	7.35	73.34
CP(0/90)	41.11	4.99	53.90
CP(90/0)	18.25	18.06	63.69
QI(0/45)	0.037	23.99	75.97

Table B.8: Pixel percentage of each thermoelastic model, after local CTE distribution

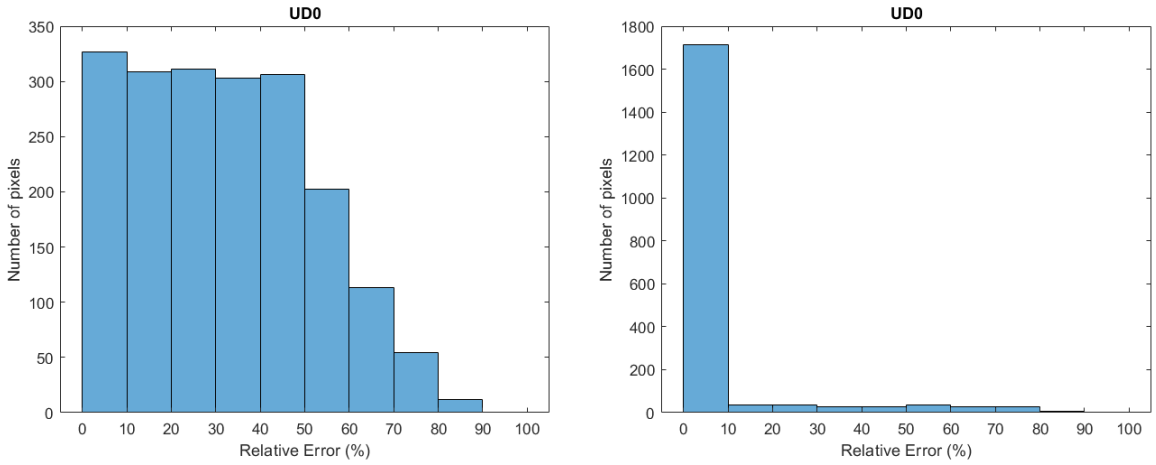

Figure B.2: UD sample minimum error histogram comparison before and after local alpha distribution

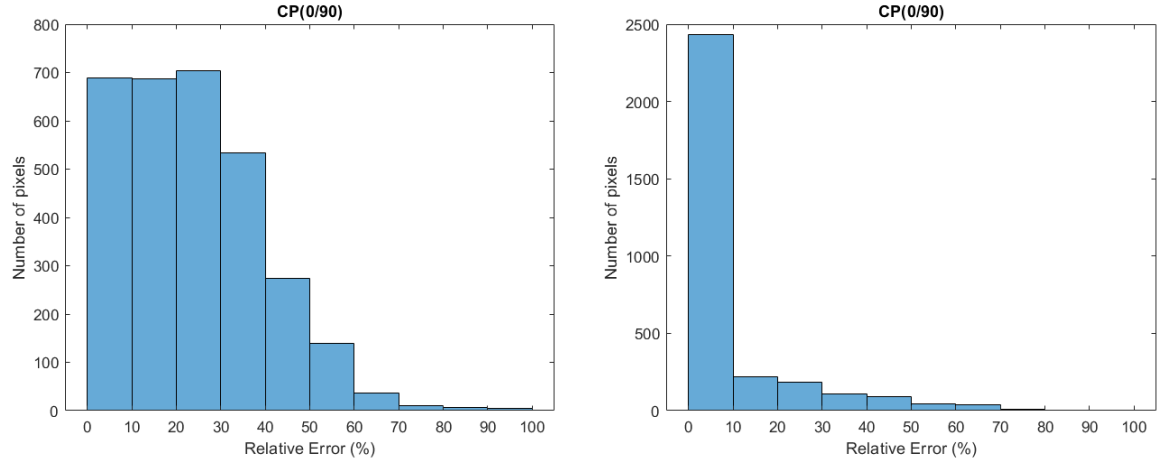

Figure B.3: Cross Ply sample minimum error histogram comparison before and after local alpha distribution

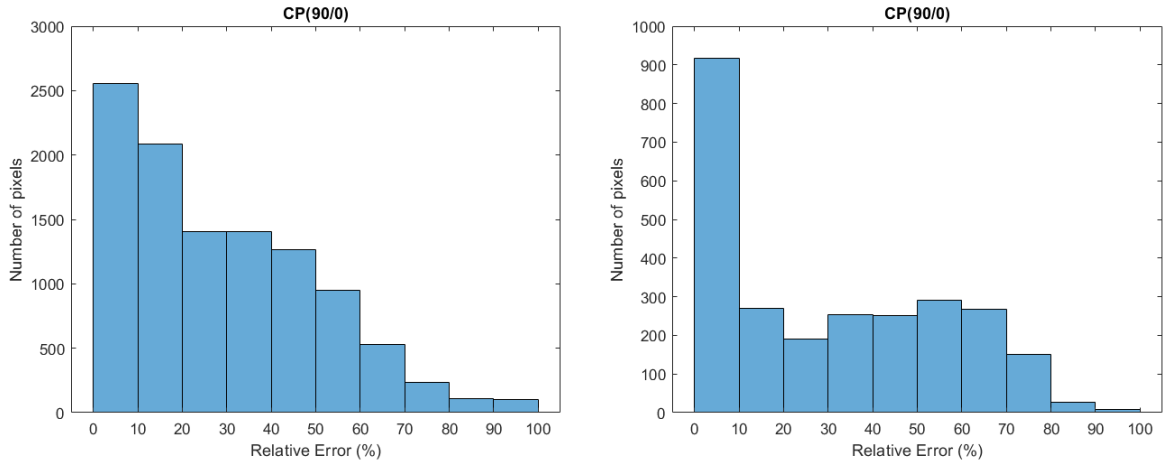

Figure B.4: Cross Ply sample minimum error histogram comparison before and after local alpha distribution

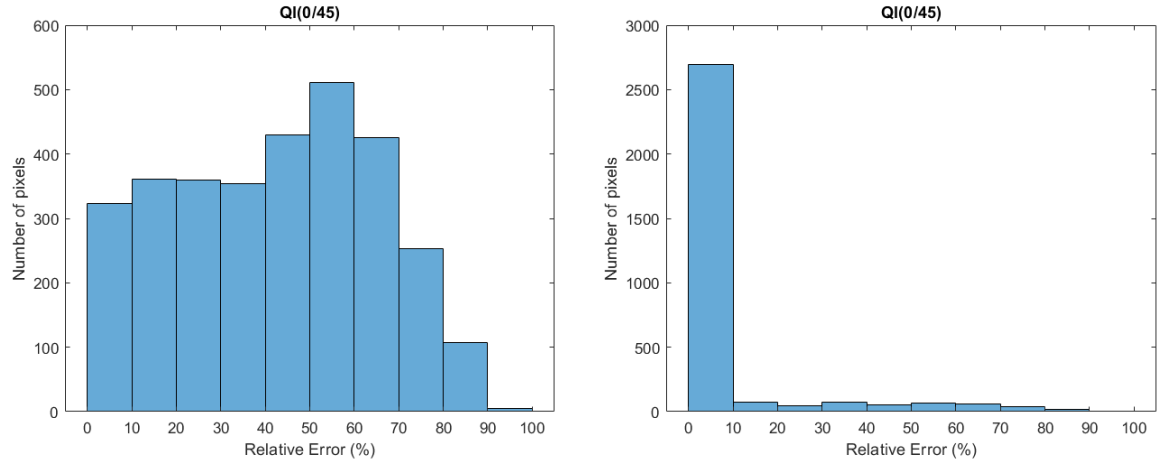

Figure B.5: Quasi-Isotropic sample minimum error histogram comparison before and after local alpha distribution

4.5 100 mm Lens (ARAMIS 12M)

Sensor	Lens	Measuring volume [mmxmm]	Comment	Min. length camera support [mm]	Distance ring [mm]	Measuring distance [mm]	Slider distance [mm]	Camera angle [°]	Calibration Object	Aperture dependent depth of field [mm]									
										1,4	2	2,8	4	5,6	8	11	16	22	32
ARAMIS 12M rev03	Titanar 100mm	25 x 19	---	500	87,5	400	148	25	CQ 23x18	---	---	---	---	n.a.	n.a.	n.a.	n.a.	n.a.	2,3
		35 x 26	---	500	62,5	415	154	25	CQ/CP20 30x24	---	---	---	---	n.a.	n.a.	n.a.	n.a.	0,4	4,3
		50 x 38	---	500	37,5	455	172	25	CQ/CP20 55x44	---	---	---	---	n.a.	n.a.	n.a.	n.a.	3,2	9,6
		65 x 49	---	500	25	505	196	25	CQ/CP20 55x44	---	---	---	---	n.a.	n.a.	n.a.	1,6	7,5	17
		80 x 60	---	500	25	560	218	25	CQ/CP20 55x44	---	---	---	---	n.a.	n.a.	n.a.	5,3	14	28
		100 x 75	---	500	12,5	635	252	25	CP20 90x72	---	---	---	---	n.a.	n.a.	1,4	12	24	45
		125 x 95	---	500	12,5	735	296	25	CP20 90x72	---	---	---	---	n.a.	n.a.	7,7	23	42	74
		150 x 110	---	500	12,5	840	342	25	CP20 90x72	---	---	---	---	n.a.	3,2	17	39	66	110
		175 x 130	---	500	12,5	940	388	25	CP20 175x140	---	---	---	---	n.a.	9,5	27	57	93	150
		200 x 150	---	800	---	1045	434	25	CP20 175x140	---	---	---	---	n.a.	18	41	80	130	>200
		250 x 190	---	800	---	1250	524	25	CP20 250x200	---	---	---	---	11	40	75	130	210	>250
		300 x 230	---	800	---	1455	616	25	CP20 250x200	---	---	---	---	28	68	120	200	>300	>300
		350 x 260	---	800	---	1665	688	24	CP20 350x280	---	---	---	---	52	110	170	290	>350	>350
		400 x 300	---	800	---	1890	688	22	CP20 350x280	---	---	---	---	89	160	250	>400	>400	>400
		500 x 380	2)	1200 fixed	---	2260	---	29	CP20 350x280	---	---	---	---	120	230	370	>500	>500	>500
		750 x 560	2)	1600 fixed	---	3310	---	27	CC20 700x560	---	---	---	---	380	630	>750	>750	>750	>750
		1000 x 750	2)	1600 fixed	---	4390	---	21	CC20 1000x800	---	---	---	---	820	>1000	>1000	>1000	>1000	>1000

Legend				
	1)	without laser pointer	---	Lens cannot be adjusted to the aperture value.
	2)	For further information please refer to the user information Hardware for ARAMIS (Fixed Base).	n.a.	It is not possible to focus the complete measuring volume.
			*	Resolution limited by aperture.
	MS	Slider distance at Mech. Stop		